UNIVERSITY OF LIVERPOOL

Optical manipulation of metallic particles

Thesis submitted in accordance with the requirements of the University of Liverpool for the degree of Doctor in Philosophy by *Zhe Shen*

March 2017

Acknowledgements

Firstly, I would like to express my sincere appreciation to my current supervisor, Prof. Yaochun Shen. I am grateful to him for taking over my supervision and taking care of me during my later PhD studies. His kind support and valuable discussions are gratefully acknowledged. My gratitude also goes to Dr. Lei Su for his guidance and prudent advice.

Secondly, I thank people who have worked together with me. They are Prof. Xiaocong Yuan, Prof. Changjun Min, Prof. Chen Liu, Dr. Benham Bastani, Liang Deng, Peinan Qi, Dr. Chongyang Liu, Dr. Jidong Jin, Dr. Maduka Attamah, Jinke Zhang, Dr. Danhua Mei, Shiyun Liu, and Yuxuan Zeng. I also thank the workshop and store of the Electrical Engineering and Electronics department for their generous assistance.

Lastly, I would like to thank my family members, for their consistent encouragement and support.

Publication List

1 **Z. Shen**, L. Su, X. C. Yuan, and Y. C. Shen, “Trapping and rotating of a metallic particle trimer with optical vortex," Appl Phys Lett **109**, 241901 (2016).

2 **Z. Shen**, L. Su, and Y. C. Shen, "Vertically-oriented nanoparticle dimer based on focused plasmonic trapping," Opt Express **24**, 16052-16065 (2016).

3 **Z. Shen**, and L. Su, "Plasmonic trapping and tuning of a gold nanoparticle dimer," Opt Express **24**, 4801-4811 (2016).

4 C. J. Min[#], **Z. Shen**[#], J. F. Shen, Y. Q. Zhang, H. Fang, G. H. Yuan, L. P. Du, S. W. Zhu, T. Lei, and X. C. Yuan, "Focused plasmonic trapping of metallic particles," Nat Commun **4**, 2891(2013). ([#]: contributed equally)

Other related publication:

1 Q. N. Chen, T. G. Liu, K. Liu, J. F. Jiang, **Z. Shen**, Z. Y. Ding, H. F. Hu, X. D. Huang, L. Pan, and C. Y. Ma, "An Improved Positioning Algorithm With High Precision for Dual Mach-Zehnder Interferometry Disturbance Sensing System," J Lightwave Technol **33**, 1954-1960 (2015).

2 L. Deng, Y. Wang, **Z. Shen**, C. Liu, D. J. J. Hu, P. P. Shum, and L. Su, "Design of Plasmonic Nanopore Platforms for Single-Molecule Detection," Asia Communications and Photonics Conference, Optical Society of America, 2014, Shanghai.

Table of Contents

Thesis title: Optical manipulation of metallic particles

Author: Zhe Shen

Abstract

Plasmonic tweezers and optical tweezers are two techniques for trapping and manipulating particles. Plasmonic tweezers utilizes localized surface plasmon field, whilst optical tweezers utilizes focused laser beam. In this thesis, these two techniques were applied for the manipulation of metallic particles in three basic forms: single particle, particle dimer and particle trimer.

Firstly, the trapping of metallic particles was investigated through focused plasmonic tweezers when surface plasmons are excited by focused Radially Polarized Beam (RPB). The force exerted on the metallic particle is responsible for the trapping, which is found to be due to the sum of both gradient and scattering forces acting in the same direction established by the coupling between the metallic particle and focused plasmonic field. This contrasts the repulsion of metallic particles in optical tweezers. Focused plasmonic trapping of metallic particle enables actively moving metallic particle in a controlled way, which could be used for intracellular Surface Enhanced Raman Scattering (SERS) imaging.

Secondly, the trapping of horizontally-oriented metallic particle dimers was theoretically studied through focused plasmonic tweezers when surface plasmons are excited by focused linearly-polarized beam. It was found that a Surface Plasmon Virtual Probe (SP-VP) pair was generated on a metal film. A formula is derived to represent the electric field of SP-VP pair, revealing that the spacing of the two virtual probes is wavelength-dependent. Each SP-VP is able to trap a metallic particle, thus the gap between the trapped particles of the dimer can be controlled by changing the excitation wavelength. This theory was further tested by successfully trapping nanosphere and nanorod metallic dimers with 10 nm gaps. The trapped dimer showed a typical electric field enhancement of more than 10^3 times, which is enough for single molecule SERS detection.

Thirdly, a vertically-oriented dimer structure was proposed based on trapping of metallic nanoparticle by focused plasmonic tweezers. The vertically-oriented dimer can effectively make use of the dominant longitudinal component of the SP-VP thus providing much stronger electric field in the gap. Furthermore, for practical application the top nanoparticle of the dimer can be replaced with the tip of an atomic force microscope which enables the precise control of the gap distance of the dimer. Therefore the proposed vertically-oriented dimer structure provides both the scanning capability and the extremely-high electric field enhancement necessary for the high sensitivity Raman imaging.

Lastly, the stable trapping and steady rotation of a metallic particle trimer were experimentally achieved by optical tweezers with optical vortex. The trimer particles are found to be confined inside the maximum intensity ring of a focused circularly polarized optical vortex. Theoretical analysis suggests that a large proportion of the radial scattering force pushes the particles together, whilst the remaining portion provides the centripetal force necessary for the rotation. The achieved steady rotation of the metallic particle trimer may lead to the development of microfluidics devices such as micro-rotor.

List of Figures

Symbols and Abbreviations

List of Symbols

α	polarizability
c	speed of light
ε	permittivity
f	focal length
i	imaginary unit
k	wavevector
k_B	Boltzmann constant
l	topological charge
λ	wavelength
ω	frequency
w	beam waist
π	3.1415926…
$\hbar$	reduced Planck constant

List of Abbreviations (Alphabet order)

3D	Three Dimensional
AFM	Atom Force Microscopy
ATR	Attenuated Total Reflection
CCD	Charge Coupled Device
CGH(s)	Computer Generated Hologram(s)
CVBs	Cylindrically Vector Beams
DDA	Discrete Dipole Approximation
DNA	Deoxyribose Nucleic Acid
EBL	Electron Beam Lithography
FDTD	Finite-Difference Time-Domain
FEM	Finite Element Method
FWHM	Full Width at Half Maximum
(L)SP(R)	(Localized) Surface Plasmon (Resonance)
MST	Maxwell Stress Tensor

NA	Numerical Aperture
NSOM	Near-field Scanning Optical Microscopy
OAM	Orbital Angular Momentum
OTRS	Optical Tweezers Raman Spectroscopy
RPB	Radially Polarized Beam
SAM	Spin Angular Momentum
SERS	Surface Enhanced Raman Scattering
SLM	Spatial Light Modulator
SPW	Surface Plasmon Wave
SPP(s)	Surface Plasmon Polariton(s)
SPR	Surface Plasmon Resonance
SP-VP	Surface Plasmon Virtual Probe
TERS	Tip Enhanced Raman Scattering

Chapter 1 Introduction

1.1 Motivation

Metallic particles especially noble metal particles have many favourable features such as covalent attachment, catalysis and high free-electron density [1-8], which make metallic particles quite useful in many disciplines such as medical science, pharmacology and chemical analysis. In medical science, metallic particles can be used in targeted chemotherapy for cancer treatment [3, 9-14]. When tumour cells containing gold nanoparticles are exposed to laser, the tumour cells will be attacked and destroyed because of the photo-thermal effect. In pharmacology, metallic particles can be used for convenient drug delivery [15-17]. Proteins, drugs, nucleic acids and fluorescence molecules can be easily attached to gold nanoparticles. When biological cells absorb gold nanoparticles, the attached substances enter the biological cells. With only treatment of targeted cells, diseases can be cured with minimum side effect. In chemical analysis, metallic particles can be used in Surface Enhanced Raman Scattering (SERS) [18, 19]. Due to Localized Surface Plasmon Resonance (LSPR) effect, the electric field around metallic particle is enhanced. Since the Raman enhancement is proportional to the fourth power of the electric field enhancement, the Raman signal will be amplified significantly with the enhanced electric field.

Nowadays, SERS has expanded to characterise complex structures such as biological cells. Intracellular SERS measurement of the biological cells is important for early diagnosis of diseases, as cytometaplasia always occurs before disease symptoms start to show. Because biological cells have the capability to up-take metallic nanoparticles, employing metallic nanoparticles in the intracellular SERS

measurement is a preferred method, which has attracted much attention from researchers. Kneipp *et al* have tried the SERS imaging of a single living cell with gold nanoparticles [19]. As the gold nanoparticles were randomly distributed inside the cell, the measurement did not cover fully for the cell. Kawata's group investigated the usage of a gold nanoparticle in SERS measurement of a living cell [20], but their measurement had to follow the trajectory of the gold nanoparticle inside the cell.

If the movement/positions of metallic particles can be controlled, the metallic particles assisted SERS measurement can be performed at arbitrary places inside cells. Under the same condition, the metallic particles assisted targeted chemotherapy inside biological cells would be more precise, and the metallic particles assisted drug delivery would be more efficient. Therefore, the manipulation of metallic particles is highly desirable.

The current optical manipulation techniques include optical tweezers and plasmonic tweezers. Optical tweezers is a technique that uses a focused laser beam to trap objects. It has been widely used for trapping particles in the micro world, especially biological cells. Plasmonic tweezers is a technique that uses a non-uniform plasmonic field to trap objects [33-36]. Since the surface plasmon wavelength is shorter than the excitation wavelength, plasmonic focusing can break the optical diffraction limit, thus plasmonic tweezers could achieve the trapping of smaller size particles [21, 22].

Single, dimer and trimer are the three most basic forms of metallic particles. In order to manipulate metallic particles in each form, proper optical manipulation technique should be applied.

As for a single metallic particle, it is difficult to achieve the stable trapping of it by optical tweezers. Because metal naturally scatters the vast majority of incident light, it is difficult to generate proper trapping force by simply focusing laser beam onto the metallic particle. It has been reported in [21-23] that plasmonic tweezers is used to trap metallic particle. However, most previous reports about plasmonic tweezers were using nanostructures such as nano-disc [21], nano-antennae [22], and nano-pillar [23]. On the one hand, the fabrication of these structures is complex and costly. On the other hand, since these structures are fixed, they attract particles rather than move particles. Without using nanostructures, focused plasmonic tweezers was proposed based on all-optically focusing excitation of Surface Plasmon Polaritons (SPPs) on a smooth thin metal film [24].

As for a metallic particle dimer, it can further enhance Raman signal compared to a single metallic particle. When the two dimer particles are very close, due to the Localized Surface Plasmon (LSP) coupling, the dimer gap can have stronger electric field enhancement than that of the monomers [25]. Generally, the orientation of the dimer is of significant importance because the more the orientation aligns with the polarization direction the stronger the enhancement [26, 27]. The coupling efficiency reaches its maximum when the polarization direction of the incident laser beam is aligned parallel to the orientation of the dimer. Since metallic particles are free standing in liquid, most current dimers are horizontal and there is no report about other orientation of the metallic particle dimer. By using focused plasmonic tweezers, the manipulation of two kinds of metallic particle dimers with orthogonal orientations, namely horizontally- and vertically- oriented metallic particle dimers, was studied.

Meanwhile, the electric field enhancement factor is inversely-proportional to the gap distance, which is another important issue of the dimer. The gap distance control reported previously is mainly implemented by introducing material fillers to the dimer gap [28-31]. On the one hand, the gap distance is fixed although the gap distance can reach few nanometers with specific materials such as Deoxyribose Nucleic Acid (DNA) molecule [32] and single layer graphene [28]. On the other hand, the introduced materials will bring noise to the measurement as the filler materials are likely to be detected in the measurement. Therefore, maintaining an empty gap is required in the manipulation of a metallic particle dimer.

As for a metallic particle trimer, due to the stability of triangle, the rotation of the metallic particle trimer can be regarded as a micro-rotor, which has great potential in micro-fluidics devices. In order to study the rotation of a metallic particle trimer, optical tweezers with optical vortex has been applied to trap and rotate metallic particles. However, the rotation of metallic particles in previous studies is not steady. In addition, the trapped metallic particles in previous studies were individual particles rather than an integrated system, which is necessary for micro-rotor application. Therefore, the mechanisms for the trapping and rotation of metallic particles in optical vortex need to be further investigated.

1.2 Objectives

Based on the discussions above, the main objective of this thesis is to study the manipulation of metallic particles by plasmonic tweezers and optical tweezers, and to explore the applications of metallic particles manipulation systems. The objective can be divided into three sub-items as follows:

- To investigate the focused plasmonic trapping of metallic particles.

- To investigate the focused plasmonic trapping of a horizontally-oriented metallic particle dimer, to explore the gap distance tuning method, and to explore the SERS application of the horizontally-oriented metallic particle dimer.
- To design a vertically-oriented metallic particle dimer based on focused plasmonic tweezers, to analysis the feasibility and stability of the vertically-oriented metallic particle dimer, and to explore the SERS application of the vertically-oriented metallic particle dimer.
- To achieve the stable trapping and steady rotation of a metallic particle trimer by optical tweezers with optical vortex, and to investigate the trapping and rotation mechanisms of metallic particles in optical vortex.

1.3 Major contributions

During the PhD studies, the fundamental work as follows has been done:

- Based on angular spectrum representation and Richards-Wolf vectorial diffraction theory, a method for calculating the plasmonic field on metal surface excited by focused vector beams was developed. This method has been used to calculate the plasmonic field excited by focused Radially Polarized Beam (RPB) and linearly polarized beam.
- Based on Maxwell Stress Tensor (MST) method, a method for calculating the total force of metallic particle was derived. The calculated total force includes both gradient force and scattering force, which can be used to better explain the trapping mechanisms.
- Based on angular spectrum representation and Richards-Wolf vectorial diffraction theory, a method for calculating the focal field of vector beams was

developed. This method has been used for calculating the focal field of circularly polarized optical vortex.

The major achievements presented in this thesis are as follows:

- **Single metallic particle**

  Focused plasmonic tweezers was proposed for manipulating metallic particles. It is the first time that structureless plasmonic trapping of metallic particles has been achieved. This technique has solved the problem that metallic particles are hard to trap. This work has been published in [24].

- **Horizontally-oriented metallic particle dimer**

  The manipulation of a horizontally-oriented metallic particle dimer was achieved with focused plasmonic tweezers. The gap distance of the dimer can be adjusted by changing the parameters of the trapping system such as the wavelength of incident light. The dimer with its gap distance under control in nanoscale has potential applications in lab-on-chip devices, biosensing, single molecule SERS detection, and so on. This work has been published in [33].

- **Vertically-oriented metallic particle dimer**

  A vertically-oriented dimer structure was designed based on plasmonic trapping of a metallic nanoparticle. The gap distance of the vertical dimer can be controlled. The vertical dimer system has potential application in the scanning Raman spectroscopy for imaging with high sensitivity. This work has been published in [34].

- **Metallic particle trimer**

  The first stable trapping and steady rotation of a metallic particle trimer in optical vortex was experimentally demonstrated. The trapping and rotation of metallic particle trimer in optical vortex provides an alternative method for micro-rotor,

which has great potential in micro-fluidics devices. This work has been published in [35].

1.4 Organization of this Thesis

This thesis is made up of the following 7 chapters:

Chapter 1 is the introduction of the thesis, which includes motivation, objectives, major contributions and organization of the thesis.

Chapter 2 is the background of the thesis, which includes topics such as surface plasmon, optical vortex, radially polarized beam, SERS, optical tweezers, plasmonic tweezers.

Chapter 3 is the work about focused plasmonic trapping of metallic particles. In this chapter, the Surface Plasmon Virtual Probe (SP-VP) will be firstly introduced. Secondly, force analysis methods for metallic particles in optical field will be introduced. Thirdly, the trapping mechanisms for metallic particles will be introduced. Lastly, detailed comparison between plasmonic tweezers and optical tweezers from aspects of Poynting vector, total force, force components and charge distribution will be made.

Chapter 4 is the work about plasmonic trapping and tuning of a horizontally-oriented metallic particle dimer. In this chapter, the SP-VP pair will be firstly introduced. Secondly, the trapping mechanisms for metallic particle dimers will be introduced. Thirdly, gap distance tuning mechanism for metallic particle dimers will be introduced. Lastly, the SERS application of the horizontal dimer will be introduced.

Chapter 5 is the work about vertically-oriented nanoparticle dimer based on focused plasmonic tweezers. In this chapter, the theories for studying the vertical dimer

system will be firstly introduced. Secondly, the trapping mechanism for the dimer particle will be introduced. Thirdly, SERS application of the vertical dimer will be introduced. Lastly, plasmon hybridization and charge distribution evidences for the strong electric field enhancement in the vertical dimer gap will be introduced.

Chapter 6 is the work about manipulation of a metallic particle trimer based on optical tweezers. In this chapter, experimental trapping and rotation of a gold particle dimer and a silica particle tetramer will be firstly introduced. Secondly, the circularly polarized optical vortex will be introduced. Thirdly, the trapping and rotation mechanisms of gold particles in focused optical vortex will be introduced.

Chapter 7 is the conclusion and discussion of future work. Conclusion section mainly summarizes the main points of previous chapters. Future work section offers an outlook for possible further research work.

Chapter 2 Literature review

2.1 Overview

Before introducing the main work, it is necessary to make a systematic review of the knowledge related to the work. More fundamentally, the surface plasmon excitation criteria will be reviewed firstly, followed by the review of SPPs and LSPs, including their excitation mechanisms and electric field enhancement effects. Then optical vortex and RPB will be reviewed. These are the structured light used in the tweezers systems of this thesis. Next, Raman enhancement mechanism of SERS and different kinds of the SERS substrates will be introduced. Among the SERS substrates part, emphasis will be put on the review of SERS by metallic particles and metallic particle dimer. The intracellular SERS detection by metallic particles, the gap distance and orientation issues of dimer and previous methods of forming dimers with nanoscale gap distance will be reviewed in detail. Lastly, optical tweezers and plasmonic tweezers will be reviewed. Optical trapping and rotation of metallic particles and plasmonic tweezers based on nanostructures will be reviewed in detail.

2.2 Surface plasmon

2.2.1 Overview of surface plasmon

The study of surface plasmon began with the interaction between electrons and metal. Ruthemann [36, 37] and Lang [38] observed energy loss during a procedure in which fast electrons passed through thin metal film in their experiments. Ritchie predicted that self-sustained collective oscillations existed on the metal surfaces due to electron-metal interaction [39]. Powell and Swan proved the

existence of surface collective oscillation by a series of experiments [40, 41]. Pines and Bohm predicted that the collective oscillation might be associated with Coulomb interaction [42]. Ritchie continued to study the electron-metal interaction and found that the surface collective oscillation was affected by the boundary condition of metal film [39]. The surface collective oscillation was called surface plasmon for the first time by Stem and Ferrell [43]. In 1968, Otto [44], Kretschmann and Raether [45] proposed their configurations for the excitation of surface plasmon with using Attenuated Total Reflection (ATR) structure.Basically, surface plasmons have two modes: SPPs and LSPs, which are shown in Fig. 2.1. SPPs are also known as propagating surface plasmons. They can propagate tens of micrometers distance along the dielectric-metal interface. Simultaneously, they also penetrate several hundreds of nanometers in the z direction [Fig. 2.1(a)]. LSPs appear when light interacts with nanostructures, e.g. nanosphere [Fig. 2.1(b)]. The size of the nanosphere is much smaller than the incident light wavelength (i.e. diameter<λ/10). In the following subsections, SPPs and LSPs will be introduced in detail.

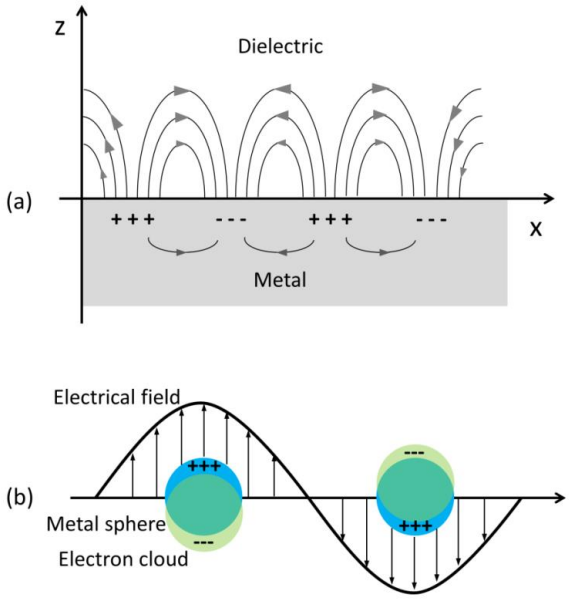

Fig. 2.1 Schematic diagrams for (a) SPPs on dielectric-metal interface and (b) LSPs around metal spheres.

2.2.2 Surface plasmon polaritons

SPPs can be in the form of electromagnetic wave that appears when an incident laser beam enters into a metal film carrying free electrons. Under certain circumstances, collective resonance oscillation of the free electrons can be formed on the metal film. The oscillation will initiate a Surface Plasmon Wave (SPW) at the excitation point on the metal film. The excited SPW will propagate along the metal film. The field of the wave decays exponentially from both transversal and longitudinal directions [46].

As shown in Fig. 2.2, the wavevector of incident light k_{light} can be expressed as

$$k_{light} = \frac{\omega_0}{c}\sqrt{\varepsilon_1}\sin\theta_{SP} \tag{2.1}$$

where ε_1 is the dielectric constant of the dielectric medium and θ_{SP} is the Surface Plasmon Resonance (SPR) angle. The surface plasmon has a momentum determined by the parameters of the metal film and the two-sided mediums. The surface plasmon momentum p_{SP} relates to k_{SP}, and it can be expressed as

$$p_{sp} = \hbar k_{SP} \tag{2.2}$$

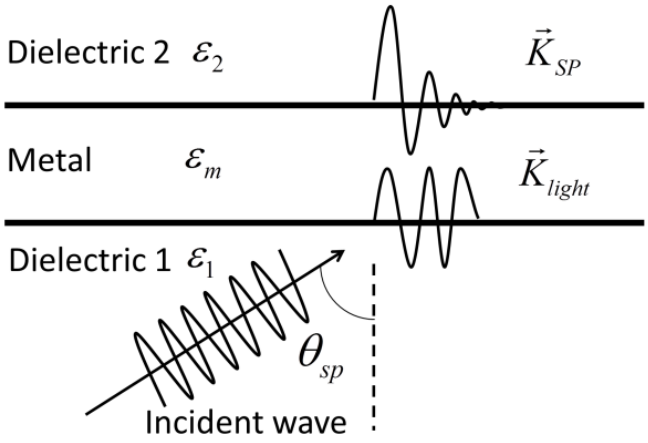

Fig. 2.2 The SPW excitation at the metal film.

If SPW is generated on an ideal interface and it propagates along the interface, a longitudinal component of the electric field should exist, but a s-polarized SPW whose electric field is parallel to the interface does not exist, although the magnetic field of the wave may propagate along the interface. Therefore, only a p-polarized beam can excite surface plasmon on a metal film.

As shown in Fig. 2.3, two semi-infinite media with dielectric constants ε_1 and ε_2 are separated by a planar interface at z=0. Their dielectric constants are frequency dependent. The electric field E and magnetic field H propagating along x direction can be expressed with the following equations [46]:

$$E_i = (E_{ix}, 0, E_{iz}) e^{-\kappa_i |z|} e^{i(q_i x - \omega t)} \tag{2.3}$$

$$H_i = (0, E_{iy}, 0) e^{-\kappa_i |z|} e^{i(q_i x - \omega t)} \tag{2.4}$$

where q_i is the magnitude of the wavevector, which is parallel to the interface. Solving Maxwell's equations by substituting Eqs. (2.3) and (2.4), we can obtain

$$i\kappa_1 H_{1y} = +\frac{\omega}{c}\varepsilon_1 E_{1x} \tag{2.5}$$

$$i\kappa_2 H_{2y} = -\frac{\omega}{c}\varepsilon_2 E_{2x} \tag{2.6}$$

$$\kappa_i = \sqrt{k_i^{\,2} - \varepsilon_i \frac{\omega^2}{c^2}} \tag{2.7}$$

According to the boundary conditions, the electric and magnetic fields components should be continuous. Deriving from Eqs. (2.5) and (2.6), we can obtain

$$\frac{\kappa_1}{\varepsilon_1} H_{1y} + \frac{\kappa_2}{\varepsilon_2} H_{2y} = 0 \tag{2.8}$$

$$H_{1y} - H_{2y} = 0 \tag{2.9}$$

$$\frac{\varepsilon_1}{\kappa_1} + \frac{\varepsilon_2}{\kappa_2} = 0 \tag{2.10}$$

The wavevectors should satisfy the continuity of the boundary conditions. The surface plasmon wavevector can be expressed as follows:

$$k(\omega) = \frac{\omega_0}{c}\sqrt{\frac{\varepsilon_1\varepsilon_2}{\varepsilon_1+\varepsilon_2}} \tag{2.11}$$

where ω_0 is the angular frequency of the incident light wave and c is the light speed. Using the parameters in Fig. 2.2, we can obtain the surface plasmon dispersion relation for the metal film structure, and the frequency dependent surface plasmon wavevector can be expressed as

$$k_{SP} = \frac{\omega_0}{c}\sqrt{\frac{\varepsilon_2\varepsilon_m}{\varepsilon_2+\varepsilon_m}} \tag{2.12}$$

where ε_2 is the dielectric constant of the dielectric 2 (Fig. 2.2) and ε_m is the dielectric constant of the metal. Another criterion for SPPs generation is that the complex dielectric constants of the metal and dielectric 2 (Fig. 2.2) media need to have opposite signs, i.e. $\mathrm{Re}(\varepsilon_m) < -\mathrm{Re}(\varepsilon_2)$. The resonance of SPPs occurs when the incident light wavevector matches with the surface plasmon wavevector. This can be expressed by the following equation:

$$k_{light} = \frac{\omega_0}{c}\sqrt{\varepsilon_1}\sin\theta_{SP} = k_{sp} \tag{2.13}$$

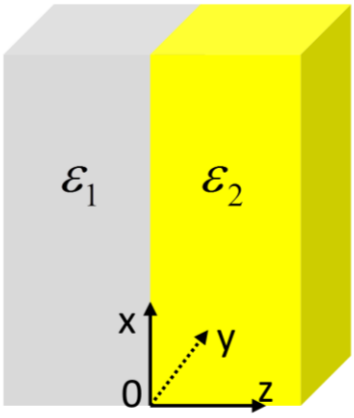

Fig. 2.3 Two semi-infinite media with different dielectric constants.

Fig. 2.4 shows the dispersion relations for light associated with the metal film structure. At frequency ω_l, the momentum of light in vacuum is $\hbar \times \Delta k_{x1}$ less than that of surface plasmon, and the momentum of light in dielectric medium is $\hbar \times \Delta k_{x2}$ higher than that of surface plasmon. Neither of them is able to excite the resonance of surface plasmon because of the momentum mismatching. In order to satisfy the surface plasmon excitation condition, compensating the momentum is necessary. We can either increase the wavevector of light in vacuum or decrease the wavevector of light in dielectric medium. Based on the momentum compensation, the following methods have been used for the surface plasmon excitation.

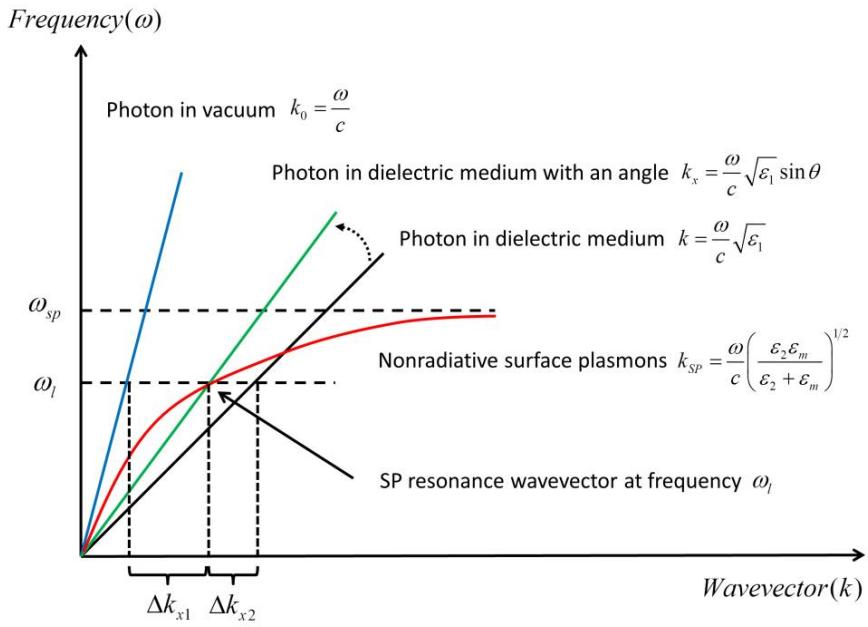

Fig. 2.4 Dispersion relations: photon in vacuum (blue line). Photon in dielectric medium with an angle (green line). Photon in dielectric medium (black line). Nonradiative surface plasmons (red curve). [47]

2.2.2.1 Attenuated total reflection

In 1968, Otto proposed the configuration in Fig. 2.5(a) for the surface plasmon excitation [44, 46]. In this system, a thin metal film and a prism are separated by a dielectric medium, i.e. air. When the light wave is incident at a

surface plasmon angle that is larger than the critical angle, ATR occurs. If the wavevector of the evanescent wave matches with that of SPPs, the photons will tunnel through the air gap and the energy will transfer to the surface plasmon. Surface plasmon excitation based on this configuration is hard to repeat because of the difficulty of maintaining the air gap. In the same year, Kretschmann proposed the configuration in Fig. 2.5(b) for the surface plasmon excitation [45]. In this configuration, a thin metal film is attached to the prism, and when light wave is incident from the optically dense medium (prism), ATR occurs. If the wavevector matching condition is satisfied, photons will penetrate the metal film and couple with the surface plasmon. This configuration is widely used because it is easy to build.

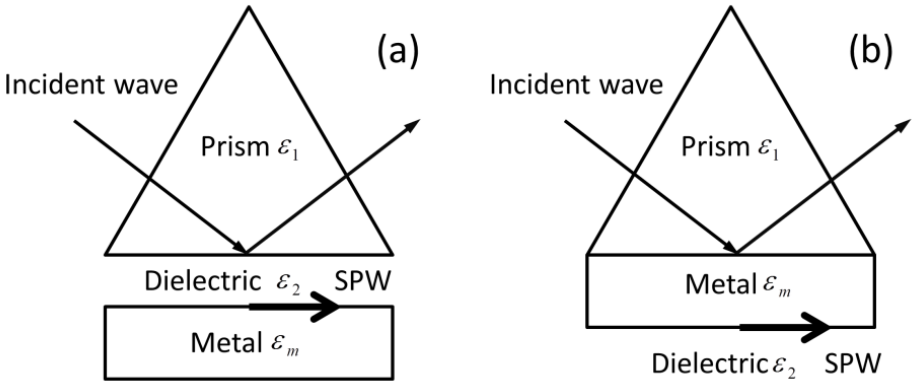

Fig. 2.5 (a) Otto configuration. (b) Kretschmann configuration.

2.2.2.2 Grating

Metal grating structure can also be used for the surface plasmon excitation [46]. The grating is made up of periodic sub-wavelength slits. As shown in Fig. 2.6, the incident wave can be scattered to many orders. In a specific order, the wave is able to provide additional momentum for exciting SPPs. Therefore, the grating can be used to couple free space light to the surface plasmon. The surface plasmon excitation condition based on grating can be simply obtained by the following wavevector matching equation:

$$k_{sp} = k_{in} \pm \frac{2m\pi}{\Lambda} \tag{2.14}$$

where k_{in} is the incident wavevector, m is the integer, and Λ is the grating pitch.

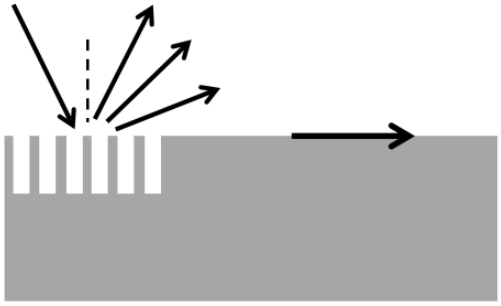

Fig. 2.6 Metal grating configuration.

2.2.2.3 Near-field excitation

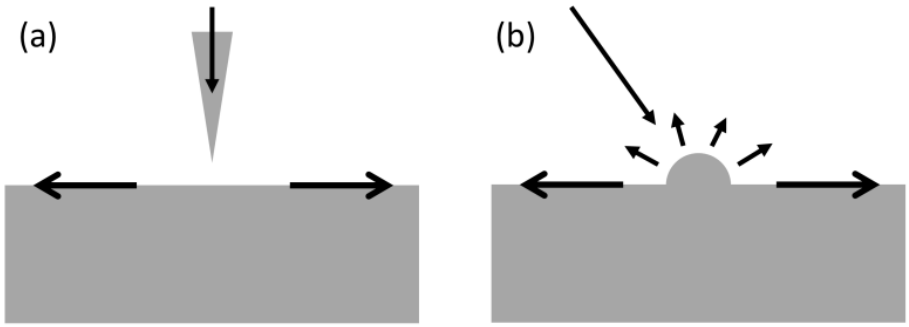

Fig. 2.7 Surface plasmon excitation on metal surfaces with (a) a nanoprobe and (b) a particle.

Near-field excitation of surface plasmon can be performed by two typical configurations as shown in Fig. 2.7. In Fig. 2.7(a), the aperture size of the nanoprobe is smaller than the wavelength of the incident light. When the light transmits from the nanoprobe, the wavevector will be increased [46, 48]. This will satisfy the wavevetor matching condition for the surface plasmon excitation on the metal surface. In Fig. 2.7(b), the protuberant particle on the metal film scatters the incident light, by which the required wavevector satisfying the surface plasmon excitation condition can be obtained. SPPs will then be formed at the vicinity of the particle.

However, each of these two configurations gives rise to excitations that have low efficiency.

2.2.2.4 Focused laser beam

Fig. 2.8 shows the laser focusing system for surface plasmon excitation. In this system, light is focused by an oil immersion objective lens, which usually has a high Numerical Aperture (NA). The immersion oil is used to match the refractive index difference between the lens and the substrate. With the strong focusing by the lens, the large SPR angle can be satisfied. If the polarization condition is satisfied, a circle of SPPs will be excited on the metal film, and they will propagate to the axis. Subsequently, an interference of SPPs will be formed and a surface plasmon standing wave will be generated. Focused structured light illumination will enable dynamic manipulation of the plasmonic field distribution on the metal film. Since this system uses objective lens, it can be easily integrated into a microscope, thus it is very suitable for research relevant to microscopy.

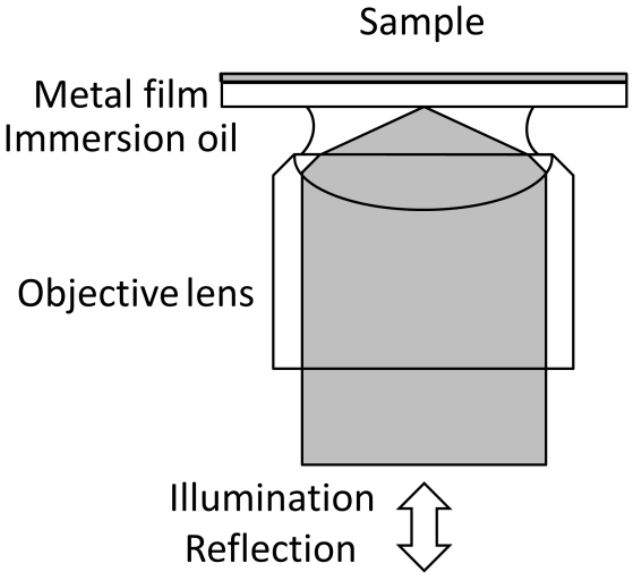

Fig. 2.8 Surface plasmon excitation with an objective lens.

The surface plasmon excitation on the metal film leads to an exponentially decaying plasmonic field. The intensity of the plasmonic field is maximum on the metal surface and it can be enhanced many times with respect to the incident field. The maximum enhancement factor is determined by the ratio of the maximum field intensity on the dielectric-metal interface ($\left|H(3/2)\right|^2$ at the excitation point, where n/n-1 indicates the side of n) to the incident field intensity in the dielectric medium ($\left|H(1/2)\right|^2$ for the p-polarized beam, where n/n+1 indicates the side of n) [46],

$$\left[\frac{\left|H(3/2)\right|^2}{\left|H(1/2)\right|^2}\right]_{\max} = \frac{1}{\varepsilon_3}\cdot\frac{2\left|\varepsilon_2'\right|^2}{\varepsilon_2''}\cdot\frac{a}{1+\left|\varepsilon_2'\right|} \tag{2.15}$$

where $a^2 = \left|\varepsilon_2'\right|(\varepsilon_1 - 1) - \varepsilon_1$. Note that the electric field is not continuous across the interfaces. We can get the enhancement factor of the electric field intensity by the following equation:

$$\frac{\left|E(3/2)\right|^2}{\left|E(1/2)\right|^2} = \frac{\varepsilon_1}{\varepsilon_3}\cdot\left[\frac{\left|H(3/2)\right|^2}{\left|H(1/2)\right|^2}\right] \tag{2.16}$$

Through calculations, the SPPs on the metal surface can have an electric field enhancement factor of around 100 when proper parameters are chosen.

2.2.3 Localized surface plasmon

LSP is the result of the confinement of surface plasmon. LSP can also be described by the localization of free electrons induced by the external excitation. It leads to a strong electric field enhancement. The frequency of LSP can be determined through solving the Laplace's equation while invoking proper boundary conditions. If the size of the nanostructure is much smaller than the wavelength

corresponding to the frequency of LSP, then quasi-electrostatic approximation is applicable in solving the equation [49].

A metallic nanosphere in a uniform electromagnetic radiation environment is the simplest situation of LSP excitation [Fig. 2.1(b)]. Taking the radius of the nanosphere, the dielectric constants of the nanosphere, and the ambient medium to be R, ε_m and ε_0, respectively, and solving Laplace's equation, the electrostatic potentials inside and outside the nanosphere can be obtained [49]:

$$\phi_{in}(r,\theta,\varphi)=\sum_{l=0}^{\infty}\sum_{m=-l}^{l}a_{lm}r^{l}Y_{lm}(\theta,\varphi),0\le r\le R \tag{2.17}$$

$$\phi_{out}(r,\theta,\varphi)=\sum_{l=0}^{\infty}\sum_{m=-l}^{\infty}b_{lm}\frac{1}{r^{l+1}}Y_{lm}(\theta,\varphi),r\ge R \tag{2.18}$$

where $Y_{lm}(\theta,\varphi)$ is the spherical harmonic, and l is the angular momentum label of atomic orbitals. If we only consider the situation that $l=1$ and the incident electric field (E_0) is in x direction, the potentials can be simplified to

$$\phi_{in}=Ar\sin\theta\cos\varphi \tag{2.19}$$

$$\phi_{out}=(-E_0r+B/r^2)\sin\theta\cos\varphi \tag{2.20}$$

where A and B are constants to be determined. Invoking the boundary conditions, i.e. the continuity of ϕ and $\varepsilon\cdot\partial\phi/\partial r$ at the surface of the nanosphere, Eqs. (2.19) and (2.20) can be solved. The obtained potential outside the nanosphere can be used to determine the electric field outside the nanosphere, which can be expressed as

$$\vec{E}_{out}=E_0\hat{x}-\alpha E_0\left[\frac{\hat{x}}{r^3}-\frac{3x}{r^5}(x\hat{x}+y\hat{y}+z\hat{z})\right] \tag{2.21}$$

where α is the polarizability of the nanosphere, and $\hat{x}$, $\hat{y}$ and $\hat{z}$ are the unit vectors in Cartesian coordinates. The polarizability can be obtained from the solution of the Laplace's equation:

$$\alpha = \frac{\varepsilon_m - \varepsilon_0}{\varepsilon_m + 2\varepsilon_0} = \frac{\varepsilon' + i\varepsilon'' - \varepsilon_0}{\varepsilon' + i\varepsilon'' + 2\varepsilon_0} \tag{2.22}$$

where ε' and ε'' represent the real and imaginary parts of the permittivity of the nanosphere, respectively. According to Eq. (2.22), the magnitude of electric field outside the nanosphere will be maximum when $\varepsilon' + 2\varepsilon_0 = 0$. This is the resonance equation of the dispersion relation for a nanosphere. In this case, α can be expressed as

$$\alpha = \frac{-2\varepsilon_0 + i\varepsilon'' - \varepsilon_0}{i\varepsilon''} = \frac{3i\varepsilon_0 + \varepsilon''}{\varepsilon''} = 1 + 3\frac{\varepsilon_0}{\varepsilon''}i \tag{2.23}$$

According to Eq. (2.23), the polarizability is positively correlated to the dielectric constant of the ambient environment and negatively correlated to the imaginary part of the permittivity of the nanosphere. Thus we can either increase the refractive index of the environment or decrease ε'' to obtain a stronger electric field.

When the size of the nanosphere increases, the contribution from higher multipole, especially the quadruple term ($l = 2$), becomes more and more significant [50]. The calculation of LSP in higher order mode can be obtained by simulation or by Mie scattering theory.

If the nanostructure has other shapes such as triangle or cube, then the Laplace's equation becomes complex and the solution is no more explicit. Numerical methods such as Discrete Dipole Approximation (DDA) and (Finite-Difference Time-Domain) FDTD are then applicable. In these methods, the nanostructure is divided to finite elements, and solving the Maxwell's equations can determine the electric field around the nanoparticle.

2.3 Optical vortex

2.3.1 Overview of optical vortex

Optical vortex is generally regarded as an optical beam with helical wavefront in its optical field [51]. The twisting of the helical wavefront leads to a diminishing intensity in the optical axis, which can be explained by phase singularity occurring at the center of the optical beam [52]. Because of the dark core of the intensity profile, optical vortex is known as 'doughnut' beam. The general expression for the complex amplitude of optical vortex is given by

$$E(\rho,\theta) = A(\rho)\exp(il\theta) \tag{2.24}$$

where $A(\rho)$ is the amplitude of optical wave, and $\exp(il\theta)$ describes the helical phase; l is the topological charge of the optical vortex.

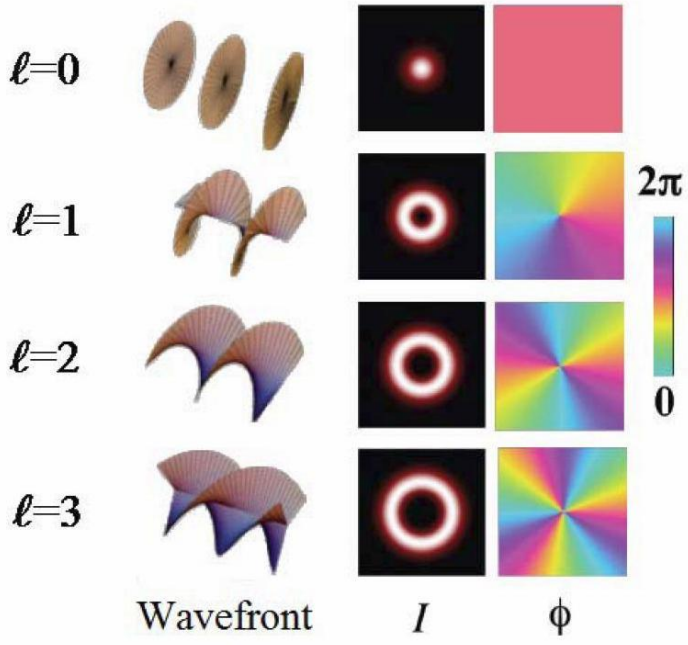

Fig. 2.9 The left, middle and right columns show the helical wavefronts, transverse intensity profiles and transverse phase distributions of the optical vortices with topological charges from 0 to 3. [53]

Fig. 2.9 shows the helicity and optical field of optical vortices with different l. The helicoid starts with $l=1$ or $l=-1$. The sign of l is associated with the

rotation direction of the helicoid. Looking along the optical propagation direction, the positive sign of l represents anticlockwise rotation, and vice versa. The size of the maximum intensity ring of the optical vortex increases with l.

2.3.1 Generation of optical vortex

There are several practical ways to generate an optical vortex as follows: (1) phase modulation of an incident laser beam with a spiral phase plate; (2) holographic methods such as designing Computer Generated Holograms (CGHs) on a Spatial Light Modulator (SLM); (3) tuning laser cavity to output the Laguerre-Gaussian mode beam; (4) mode conversion of Hermite-Gaussian mode beam with cylindrical lens. Among these ways, spiral phase plate and CGHs are most widely used.

2.3.1.1 Spiral phase plate

A spiral phase plate can introduce an azimuthal retardation to an incident optical field. It is engineered specifically to the desired topological charge and the incident wavelength. As shown in Fig. 2.10, it is a transparent plate of refractive index n whose thickness is proportional to azimuthal angle θ,

$$t = t_s \frac{\theta}{2\pi} + t_0 \tag{2.25}$$

where t_s is the step thickness, t_0 is the base thickness. When such an optical element is placed at the waist of a Gaussian beam, it is imprinted with an additional phase of $\exp(il\theta)$ and a topological charge $l = t_s \triangle n / \lambda$, where $\triangle n$ is the refractive index difference between the spiral phase plate and the surrounding air, and λ is the wavelength.

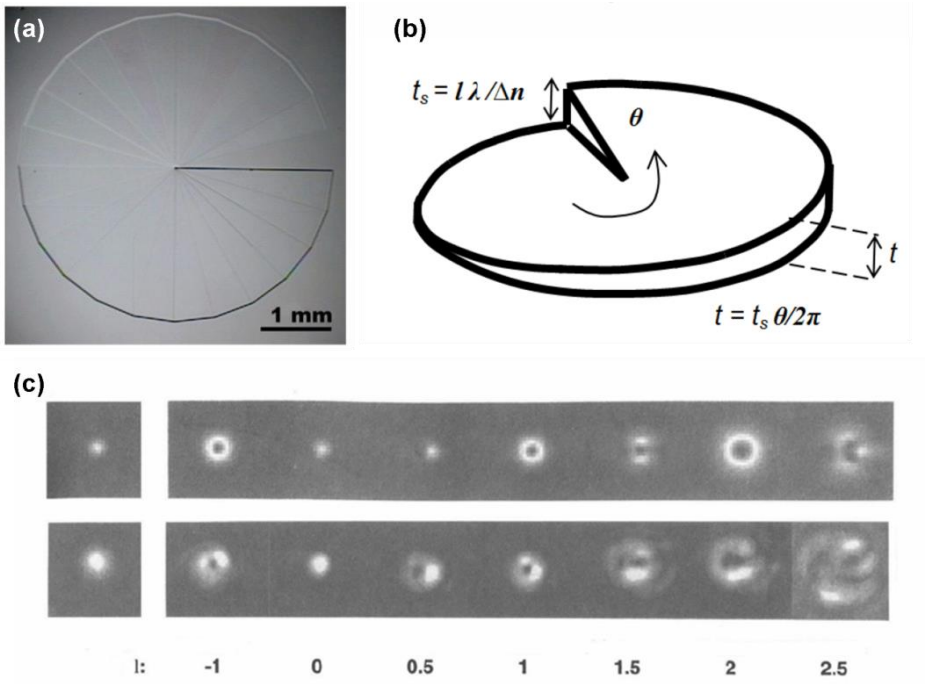

Fig. 2.10 (a) Top view of a spiral phase plate. (b) The morphology of a spiral phase plate. (c) Far-field intensity distributions of optical vortices with different topological charges produced by spiral phase plates (top row: simulation results; bottom row: experimental results). [54]

Spiral phase plate has high transmission efficiency and it can bear high laser power. The fabrication of a spiral phase plate with continuously increasing step thickness is difficult due to the requirement of the smooth control of the step thickness, thus continuously increasing step thickness is quantized to discrete step thicknesses. However, this will cause information loss of the produced optical vortex.

2.3.1.2 Computer generated holograms

The CGHs technique was introduced by Lohman *et al* [55, 56] and it is widely used to generate the LG beam [57, 58]. CGH is the calculated pattern of interference between a plane wave and a LG beam. The expression for the interference pattern can be given by

$$I = A^2 + a^2 + 2Aa\cos(l\theta - 2\pi\alpha\gamma) \tag{2.26}$$

where A is the reference beam and a is the amplitude function of the optical vortex. Consider a simple situation in which the amplitude is uniform and its value is equal to the magnitude of the reference beam, then Eq. (2.26) can be expressed as

$$I = \frac{1}{2}\left[1+\cos(l\theta - 2\pi\alpha\gamma)\right] \tag{2.27}$$

Through this equation, we can calculate the pattern of optical vortex, which looks like a regular sinusoidal amplitude grating with a 'fork' like dislocation at the center, as shown in Fig. 2.11. By using a SLM, the CGH can be used to produce an optical vortex.

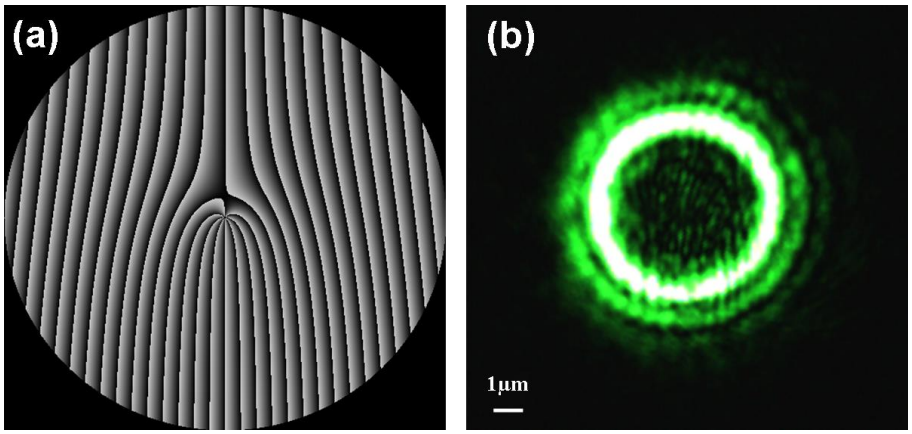

Fig. 2.11 (a) CGH used to produce an optical vortex of $l = 4$.; (b) The optical vortex corresponding to the CGH in (a). [59]

SLM allows dynamic design of the input pattern, thus using CGH based on SLM is a flexible method for optical vortex generation. However, it suffers from low diffraction efficiency. Like all other gratings, the CGH diffracts light to multiple orders and a large portion of the incident light cannot be utilized.

2.3.2 Application of optical vortex

With the unique characteristics of the helical wavefront, dark core and Orbital Angular Momentum (OAM), optical vortex has been used in various fields.

Optical vortex has been used in optical tweezers. With the transfer of OAM from the optical vortex to particles, optical vortex can exert a torque to the particles, which can be rotated in the orbits around the optical axis of the optical vortex beam [60, 61]. For trapping non-transparent and low refractive index particles, optical vortex will be more suitable than conventional beams such as Gaussian beam [61-64].

Optical vortex has been used in optical communication. Optical vortex theoretically has an infinite number of states, as there is no limit to the topological charge. The OAM-states labelled by the corresponding topological charges provide high dimensional quantum entanglements. Therefore, optical vortex can significantly improve communication bandwidth.

2.4 Radially polarized beam

2.4.1 Overview of radially polarized beam

Polarization is a basic nature of optical waves that describes the direction of the vibration. Polarization is generally divided into linear, circular and elliptical polarizations. Different from these three common polarizations, cylindrically polarized beams, also called as Cylindrical Vector Beams (CVBs), have an inhomogeneous polarization state. Their electric field vibration directions are distributed across the cross sections of the beams, and the direction of the electric field vector at each point on the cross section plane can be regarded as having rotated an angle from the radial direction. CVBs were first known as LP modes [65], which are shown in Fig. 2.12.

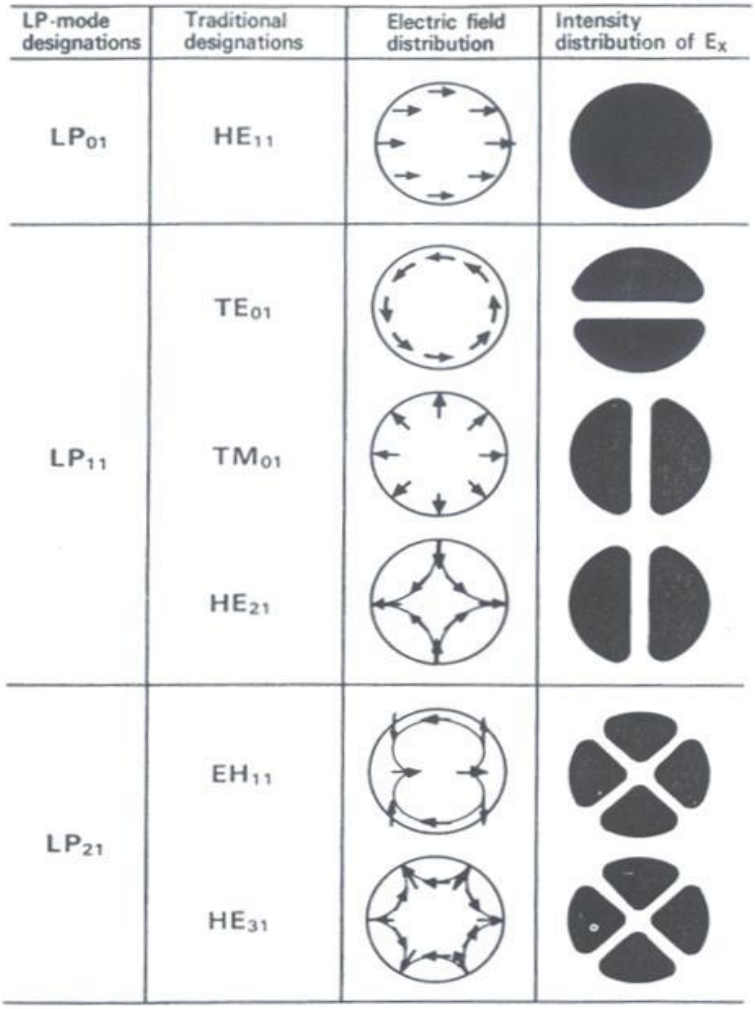

Fig. 2.12 Electric field distributions and intensity distributions of LP modes. [65]

General CVBs are in LG modes as the laser gain amplifiers are usually with radial profiles. In the CVB family, RPB receives more attention due to its unique features, as follows. Firstly, RPB has low loss when propagating in waveguides [66]. Secondly, it has higher laser cutting efficiency in metal manufacturing than linearly or circularly polarized beams [67]. Thirdly, it has a very small focused spot, which has potential applications in data storage and photoetching [68, 69].

The pure radial and azimuthal polarization modes are the solution of Maxwell's equations. Their electric field vectors across the cross sections are axially symmetrical. Generalised CVBs can be expressed as

$$E(r,\theta) = E_0(r)[\hat{r}\cos\phi + \hat{\theta}\sin\phi] \tag{2.28}$$

where $\hat{r}$ and $\hat{\theta}$ are unit vectors in the radial and azimuthal directions, respectively. The angle ϕ describes the deviation to the radial direction of the field vector at a specific point on the cross section, as shown in Fig. 2.13.

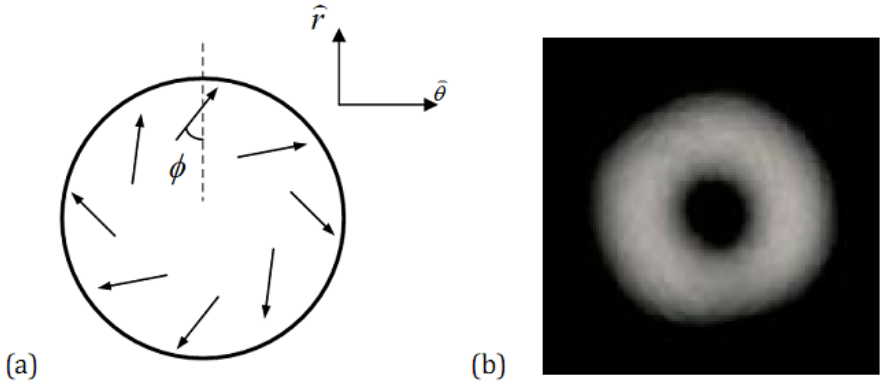

Fig. 2.13 (a) Electric field vectors of a CVB. (b) The intensity pattern of a CVB on the cross section. [70]

RPB and azimuthally polarized beam are special CVBs with ϕ equal to 90° and 0°, respectively. Their intensity profiles look like 'doughnuts' with dark cores due to the polarization singularity at the center. At the points away from the center, the electric field vectors vibrate in an axially symmetrical way as the wave moves forward. The radial and azimuthal polarizations have been illustrated in Fig. 2.14.

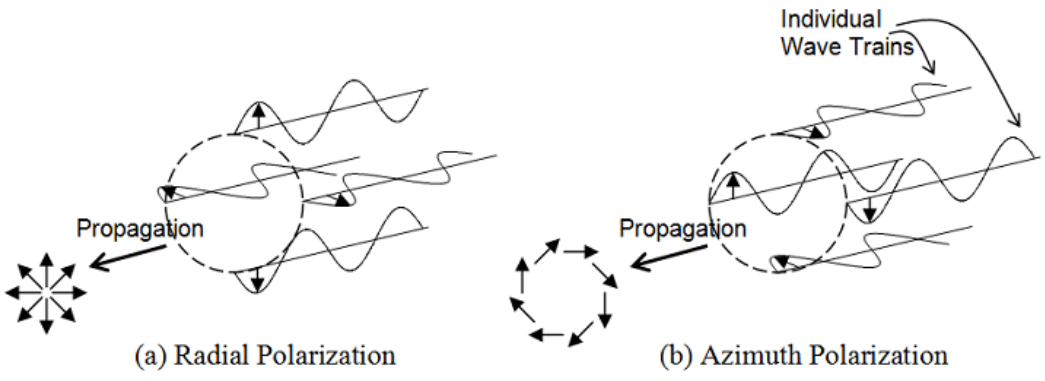

Fig. 2.14 Wave trains of (a) radial polarization and (b) azimuthal polarization. [70]

As we know, considering a single wave train, all the electric field vectors of linear polarization vibrate only in one direction. For circular polarization, the

directions of each electric field vector of the beam vary around the axis of each wave train. Different from linear and circular polarization, radial and azimuthal polarization possess their unique polarization patterns. For radial polarization, the electric field vectors either originate from or converge towards the beam center. The pattern of the electric field distribution looks like the spokes of a wheel. For azimuthal polarization, the electric field vectors are orientated along the azimuthal directions of the beam. The Jones vectors of these beams are shown in Table 2.1 [71].

Table 2.1 Jones vectors of polarized light.

Polarization state	Jones vector	Polarization state	Jones vector
Linear	$\begin{bmatrix}1\\0\end{bmatrix}$ or $\begin{bmatrix}0\\1\end{bmatrix}$	Diagonal linear	$\frac{1}{\sqrt{2}}\begin{bmatrix}1\\0\end{bmatrix}$
Left circular	$\frac{1}{\sqrt{2}}\begin{bmatrix}1\\1\end{bmatrix}$	Right circular	$\begin{bmatrix}-\sin\theta\\\cos\theta\end{bmatrix}$
Radial	$\frac{1}{\sqrt{2}}\begin{bmatrix}1\\-i\end{bmatrix}$	Azimuthal	$\begin{bmatrix}\cos\theta\\\sin\theta\end{bmatrix}$

2.4.2 Generation of radially polarized beam

RPB can be generated inside or outside the laser cavity. The methods for generating RPB can be generally classified to two strategies. One is coherent superposition of two orthogonal mode beams. The other is polarization conversion scheme. In this thesis, the latter strategy was used, which is through optical vortex beam shaping and polarization filtering. As shown in Fig. 2.15(a), azimuth type analyzer, spiral phase plate and two half wave plates are the optical elements the laser beam passes through successively. Because of the materials of these optical plates, they can bear very high incident laser power. Azimuth type analyzer is used to extract the polarization components at azimuthal directions, and its Jones matrix is

$\begin{pmatrix} -\frac{1}{2}\sin(2\theta) & \sin^2(\theta) \\ \cos^2(\theta) & \frac{1}{2}\sin(2\theta) \end{pmatrix}$. Spiral phase plate commonly used to generate optical vortex is used to compress the time-dependent polarizations here, and its Jones vector is $e^{i\theta}$. The two half wave plates are used to convert the azimuthal polarization to radial polarization, and their Jones vector is $\begin{pmatrix} 1 \\ -i \end{pmatrix}$. The Jones vector of the incident right circular polarized beam is $\begin{pmatrix} 0 & 1 \\ -1 & 0 \end{pmatrix}$. Therefore, the polarization conversion process can be express as

$$\begin{pmatrix} 0 & 1 \\ -1 & 0 \end{pmatrix} \begin{pmatrix} -\frac{1}{2}\sin(2\theta) & \sin^2(\theta) \\ \cos^2(\theta) & \frac{1}{2}\sin(2\theta) \end{pmatrix} e^{i\theta} \begin{pmatrix} 1 \\ -i \end{pmatrix} = \begin{pmatrix} \cos\theta \\ \sin\theta \end{pmatrix} \tag{2.29}$$

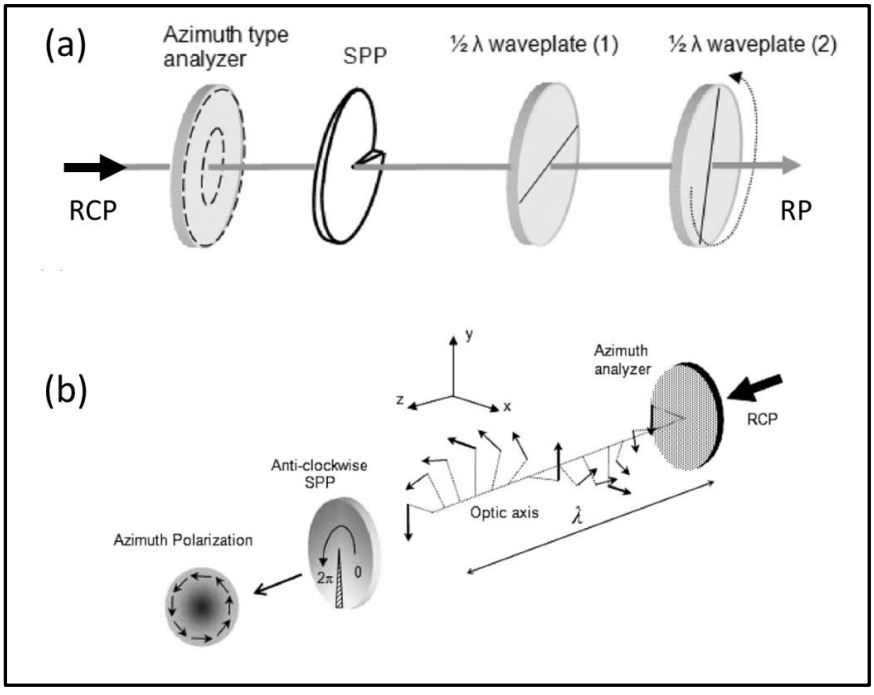

Fig. 2.15 The principle for the generation of RPB.

Fig. 2.15 (b) shows that azimuthal polarization is formed by a wave train passing through an azimuthal analyzer and a spiral phase plate. The azimuthal

analyzer can extract the azimuthal polarization from the incident beam. The azimuthal polarization can be converted to radial polarization. The Jones vector of radial polarization is $\begin{pmatrix} \cos\theta \\ \sin\theta \end{pmatrix}$.

2.4.3 Characteristics of focused radially polarized beam

Focused radially and azimuthally polarized beams have special characteristics due to rotational symmetry of their polarizations. In order to understand the difference in focusing, the focal fields are decomposed to two planes for each polarization, as shown in Fig. 2.16. For linear polarization, the electric field is parallel to the y axis before the lens. Observing the rays between the lens and focal plane, in the x section, the electric field is in the incident plane, indicating it is p polarized (TM mode). While in the y section, the electric field is perpendicular to the incident plane, indicating it is s polarized (TE mode). For radial polarization, ray is totally p polarization (TM mode) after the lens. For azimuthal polarization, ray is totally s polarization (TE mode) after the lens.

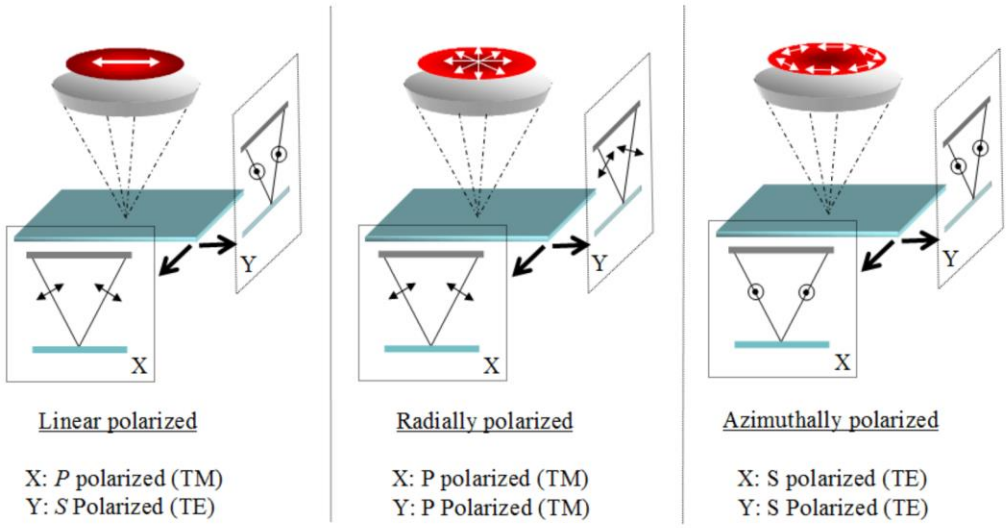

Fig. 2.16 Polarization modes illustrating of focused linearly, radially and azimuthally polarized beams.

The focal field of linearly polarized beam and RPB also differs, especially when a high NA objective lens is used. In order to know the difference, simple ray tracking and vector superposition methods are applied, as shown in Fig. 2.17.

In Fig. 2.17(a), for linear polarization, E_1 and E_2 are parallel to y axis. The direction of E_2 remains unchanged at the focal plane. There is a superposition of both E_2 at positive and negative x axes. After the lens, E_1 is no longer parallel to y axis due to the phase delay by the lens. After the lens, the x direction components of E_1 at the positive and negative y axes cancels each other and the y direction component is superimposed on the focal plane. Therefore, the intensity distribution on the focal plane for linear polarization will be no longer uniform. The focal field of circular polarization can be regarded as a time average of all possible linear polarizations.

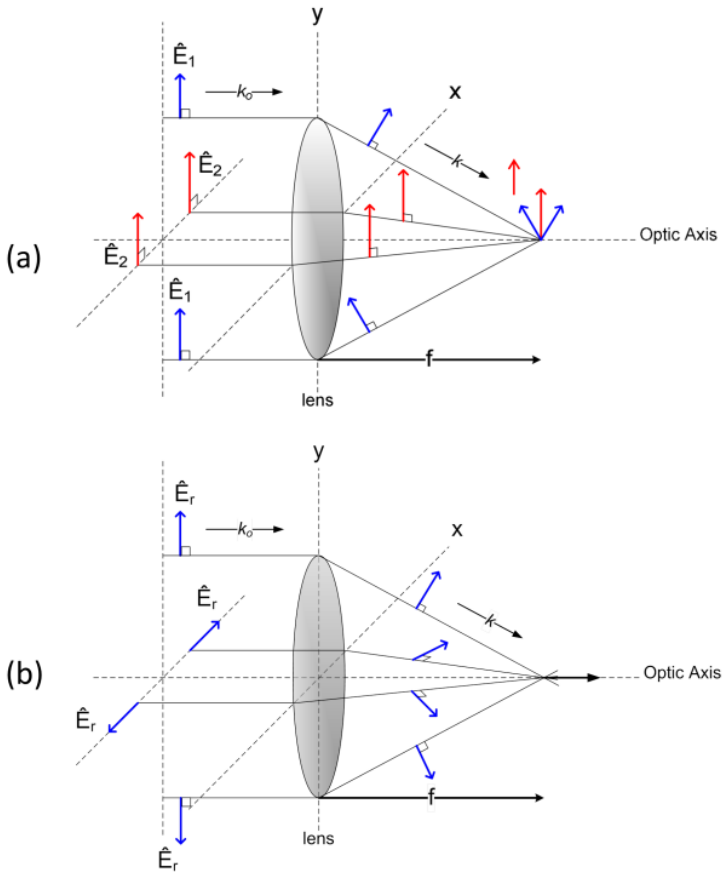

Fig. 2.17 Vector components of (a) linear polarization and (b) radial polarization in the focusing system.

In Fig. 2.17(b), for radial polarization, electric fields are in radial directions. There will be rotationally symmetrical vector components at the focal plane. After the superposition of these components on the focal plane, a strong longitudinal electric field is formed. The strong longitudinal field of focused RPB has important applications such as particle trapping and acceleration. Focused by a lens with NA approximately equal to 1, the cross section area of the focused spots of RPB and linearly polarized beam can reach $0.16\lambda^2$ and $0.26\lambda^2$ on the focal plane respectively [68, 69], which are determined by the contour of the intensity distribution at half the maximum value.

2.4.4 Surface plasmon excitation by focused radially polarized beam

The surface plasmon excitation has a strong dependence on the polarization of incident light. Only p polarization can excite SPPs in the ATR configuration. This leads to an interesting application of using RPB in a rotationally symmetrical setup for surface plasmon excitation. When RPB is launched into a dielectric-metal structure, the entire beam is p polarized with respect to the dielectric-metal interface [Fig. 2.17(b)]. A circle of light at the same specific angle will excite a circle of SPPs on a metal film. The incident light will experience corresponding loss as shown in Fig. 2.18. The SPPs will propagate to the center of the excitation area with the same phase and have a constructive interference, and then a symmetrical and locally enhanced plasmonic field will be generated. When focused linearly polarized beam is launched in the focusing system, one main direction of SPPs will be excited. These SPPs will propagate to the center of the excitation area with π phase difference and have a destructive interference, and then a minimum intensity occurs at the center of the excitation area. The surface plasmon excitation by focused RPB

and linearly polarized beam can be used to generate SP-VP and SP-VP pair respectively. The SP-VP and SP-VP pair can be used to manipulate a metallic particle and a metallic particle dimer respectively, the topic of which will be discussed in the following chapters.

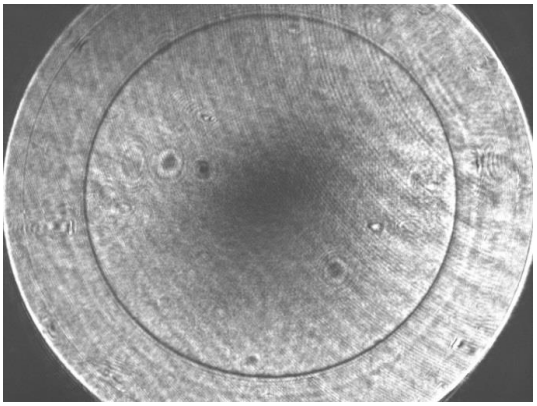

Fig. 2.18 A pupil plane image of the reflected beam when RPB is used as the excitation source in the system of Fig. 2.8. This image was collected at the back focal plane. The axis symmetrical dark ring appears due to the surface plasmon excitation.

2.5 Surface enhanced Raman scattering

Discovered about forty years ago, SERS has been widely used in applications such as biosensing, chemical material detection and environmental pollutant identification. SERS has become a main application branch of surface plasmon. SERS is a sensitive analysis technique that enhances the Raman scattering cross section of a molecule located on rough metal surface or at the vicinity of nanostructure. The enhancement factor can be as much as 10^{14}, which is comparable to that of fluorescence. The enhanced Raman spectrum allows the fingerprint information of molecule to be detected. Single molecule SERS detection that requires very strong enhancement is a frontier research area.

2.5.1 Raman enhancement

The exact mechanisms of SERS are still a matter of debate since the discovery of SERS. It is accepted that chemical and electromagnetic effects contribute to the Raman enhancement, and it is believed that the electromagnetic effect is the main factor.

The chemical effect arises from chemical interaction, which relates to the charge transfer between the sample and the metal surface. The chemical effect includes three types of enhancements: chemical bonding enhancement, surface complex resonance enhancement and photo-induced charge-transfer enhancement. The photo-induced charge-transfer enhancement is the main factor of the three foregoing enhancements.

The electromagnetic enhancement arises from the interaction between light and the metal substrate. Both incident light and scattering light are engaged. The electromagnetic enhancement includes three effects: SPR effect, the lightning rod effect and the image field effect, of these three effects the SPR effect is the main factor. The SPR frequency and the electromagnetic field enhancement are affected by the SERS substrate morphology, the environment medium and the incident light polarization. If the shape and size of metallic particles are fixed, controlling the gap distance of metallic particles and adjusting the orientation of metallic particle pair are alternative options for obtaining a desired enhancement.

Theoretical modelling indicates that the Raman enhancement of chemical effect is on the order of 100. The Raman enhancement of electromagnetic effect is related to both incident and scattering light fields, which can be expressed as

$$L(\lambda) = \left|E_{loc}(\lambda)\right| / \left|E_0\right| \tag{2.30}$$

where $|E_{loc}(\lambda)|$ and $|E_0|$ represent the amplitudes of the local field and the incident field at the Raman active site, respectively. The total power of the Stokes scattering can be expressed as [72]

$$P(\lambda_s) = N\sigma_{SERS} L(\lambda_L)^2 L(\lambda_s)^2 I(\lambda_L) \tag{2.31}$$

where *N* is the number of Stokes scatters within the Raman active site, σ_{SERS} is the scattering cross section, and I is the intensity of the incident light. Generally, the wavelength difference ($\triangle\lambda = \lambda_s - \lambda_L$) between the incident and emitted photons is much smaller than the line width of surface plasmon, and $L(\lambda)$ can be approximated to $L(\lambda_s)$. So we can obtain

$$P(\lambda_s) = N\sigma_{SERS} L(\lambda_L)^4 I(\lambda_L) = N\sigma_{SERS} \cdot RE \cdot I(\lambda_L) \tag{2.32}$$

where *RE* represents the Raman enhancement. *RE* can be expressed as follows:

$$RE = |E_{loc}(\lambda)|^4 / |E_0|^4 \tag{2.33}$$

Eq. (2.33) is the common expression for calculating the enhancement factor of the Stokes Raman scattering. From this expression, we obtain that the Raman enhancement factor is proportional to the fourth power of the electric field enhancement.

2.5.2 SERS structures

2.5.2.1 Common SERS structures

The electric field enhancement factor of LSP can easily reach three orders of magnitude more than that of SPPs. Metallic nanoparticle and nanotip are the basic elements of SERS structure, as shown in Fig. 2.19 (a) and (b) respectively. The free electrons density of a nanotip is relatively higher than that of a metallic nanoparticle, thus a nanotip is more likely to have interaction with incident photons, and the

resonance is relatively stronger. The electric field enhancement of Tip Enhanced Raman Scattering (TERS) using a nanotip is enough for single molecule detection. However, for detection of molecules inside a biological cell, the nanotip has to puncture the biological cell. Later, researchers found a vertical gap mode for the electric field enhancement, as shown in Fig. 2.19 (c) and (d). When a metallic particle or nanotip is close to a metal film, the LSPs couple with the SPPs on the metal film, and this leads to a stronger electric field enhancement. The vertical gap mode system has a scanning function, and it can be used for scanning imaging. However, the enhanced field is limited to the metal surface hence only the sample attached to the metal film can be measured. Fig. 2.19 (e) and (f) show the metallic particle dimer and bowtie respectively, which are two typical horizontal gap mode systems. LSP-LSP coupling can occur in the gap between them, and thus much stronger electric field enhancement can be obtained. Similar to these two dimers, nanorod dimer and nanoatenna are also widely used. However, these gap mode systems are horizontal and fixed, hence they are not able to do scanning.

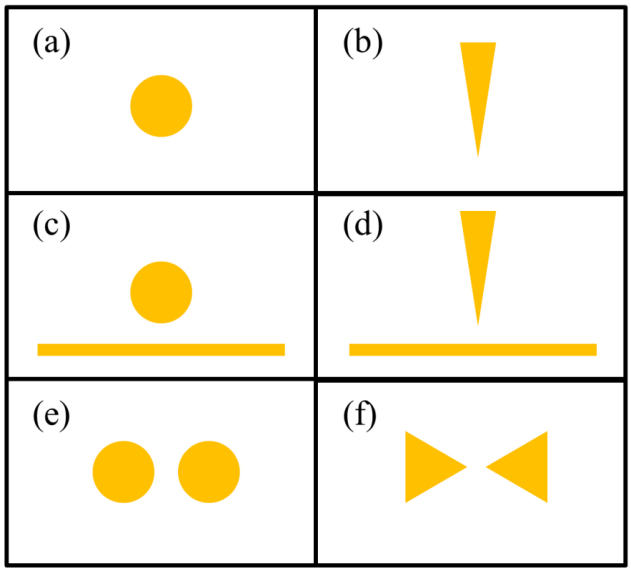

Fig. 2.19 Common SERS structures: (a) metallic nanoparticle; (b) nanotip; (c) nanoparticle-film; (d) nanotip-film; (e) metallic nanoparticle dimer; (f) bow-tie.

2.5.2.2 Metallic particles for intracellular SERS detection

As mentioned before, metallic particles can enter into biological cells for intracellular Raman measurement. In 2011, Ando *et al* demonstrated SERS imaging inside a living cell with the use of a gold nanoparticle, which travels through the intracellular space, to detect local molecular information [20]. They achieved 65 nm spatial resolution and 50 ms temporal resolution of the SERS detection for intracellular measurement. This work showed that metallic nanoparticles could work as Raman nanosensors in cells for medical and biological applications. However, they had to do laser tracking of the nanoparticle motion, as shown in Fig. 2.20. The measurement can only be performed in limited places.

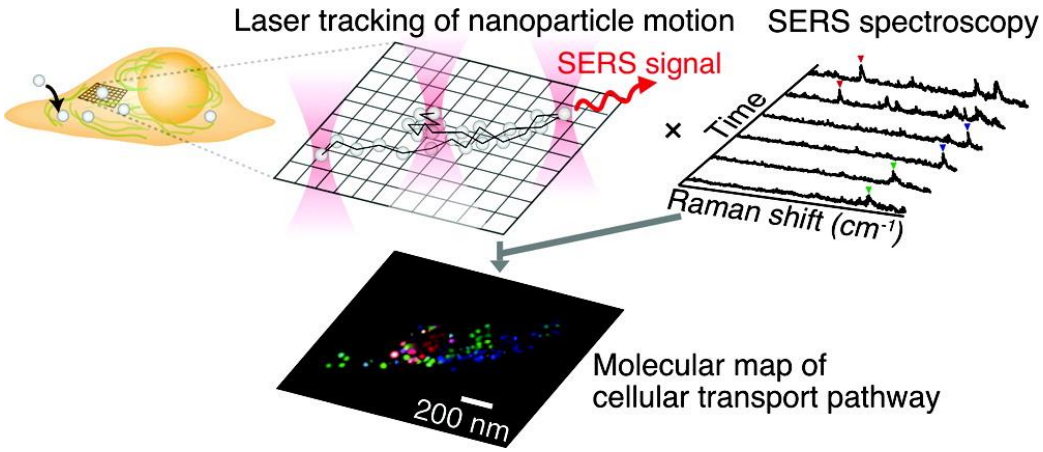

Fig. 2.20 Flow diagram of the experiment for the SERS measurement inside a cell. [20]

2.5.2.3 Metallic particle dimer: gap distance and orientation

A metallic particle dimer is a structure in which two dimer particles are very close. The dimer gap distance is significantly shorter than the size of the particle. Light illuminating on each particle will excite the LSP around the surface of each particle. When these two particles are very close, there will be a LSP-LSP coupling in the dimer gap. At the vicinity of the gap, the electric field will be dramatically enhanced, which is much stronger than that of a single particle. The enhanced field,

also called ‘hot-spot’, can be used for Raman enhancement. As mentioned before, the gap distance and the incident polarization direction will affect the Raman enhancement when the size and shape of particles are fixed.

In 2010, Lin *et al* investigated the electric field enhancement in the gap with near-field measurement by Near-field Scanning Optical Microscopy (NSOM) [73]. They directly obtained the quantitative electric field in the gap. As we can see from Fig. 2.21, the shorter the gap distance, the stronger the optical signal. The optical response of the particle dimer is also polarization dependent. When the incident polarization is the same as the orientation of the dimer (blue curve in Fig. 2.21), the enhancement is highest. Whereas, when the direction of the polarization is perpendicular to the dimer orientation (red curve in Fig. 2.21), the enhancement is lowest.

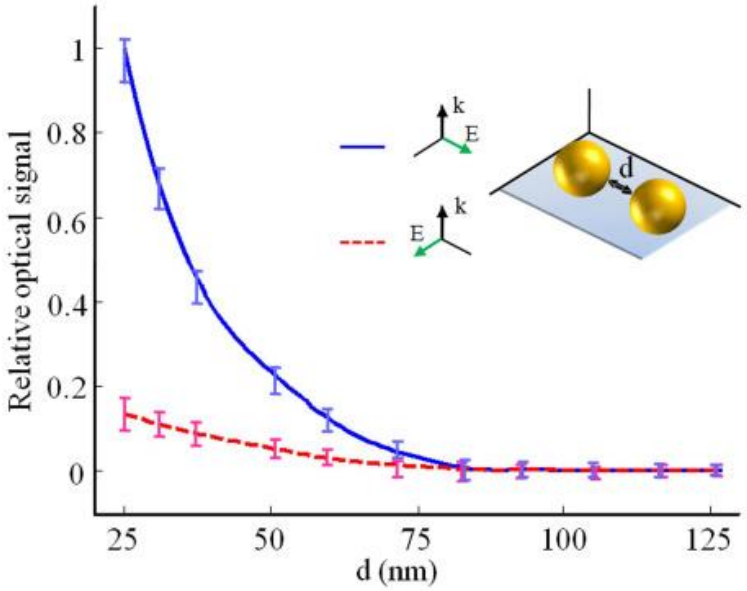

Fig. 2.21 Graph of optical field intensities in the gap of gold particle dimers against gap distance for the parallel-polarised excitation (blue curve; normalized result), and for orthogonal-polarised excitation (red-dotted curve; relative to blue curve result). [73]

In 2009, Li *et al* investigated the silver nanosphere dimer structure obtained by a special ‘one-pot’ method [74]. The dimer gap distance can reach 1.8 nm while

the diameter of the silver nanosphere is about 30 nm. The hot-spot can have up to 10^7 SERS enhancement factor. As we can see from Fig. 2.22, the intensities of Raman spectra by the dimer structure rely on the directions of the laser. The more the direction of the polarization is aligned to the orientation of the dimer the stronger the Raman signal.

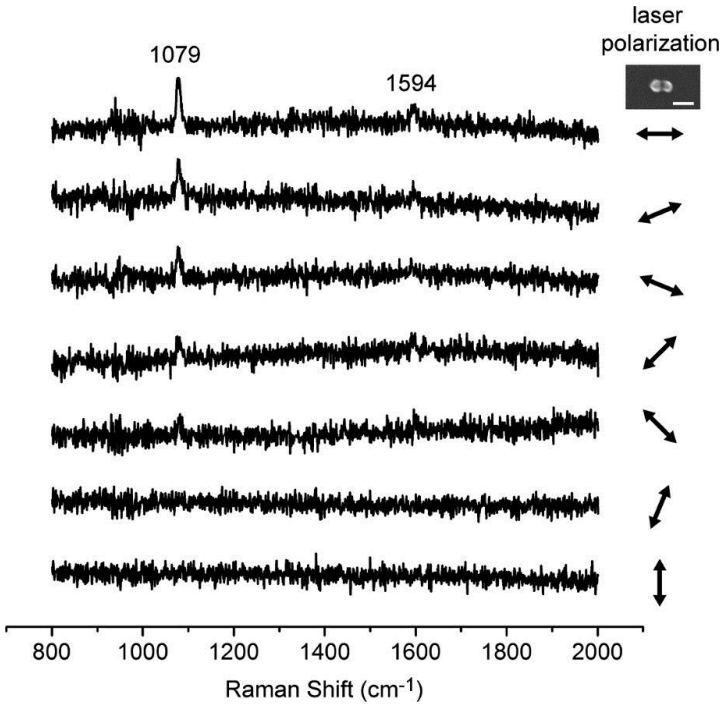

Fig. 2.22 SERS spectra by silver nanopshere dimer under illumination with different polarization directions. [74]

After review of these two reports, we can conclude: (1) the shorter the gap distance, the stronger the electric field enhancement at the gap; (2) the more the orientation aligns with the polarization direction the stronger the enhancement. The gap distance and orientation are two key issues of a dimer. For the orientation issue, most previous dimer structures are in horizontal direction, there is no work studying the orientation issue. A vertical dimer structure will be introduced in Chapter 5. This is the first time to study the orientation in a different direction. For the gap distance

issue, the previous studies about gap distance will be reviewed in the following part. The work of tuning the gap distance will be introduced in Chapter 3.

2.4.2.4 Metallic particle dimer: gap distance

For getting a dimer with nanoscale size gap distance, there are many fabrication techniques such as Electron Beam Lithography (EBL) and electrochemical growth methods. However, the fabricated or self-assembled metal nanostructures are fixed and the gap distances are predetermined and unable to be changed afterwards. Researchers have tried some other ways to obtain a metallic particle dimer with a nanoscale gap, as show in Fig. 2.23.

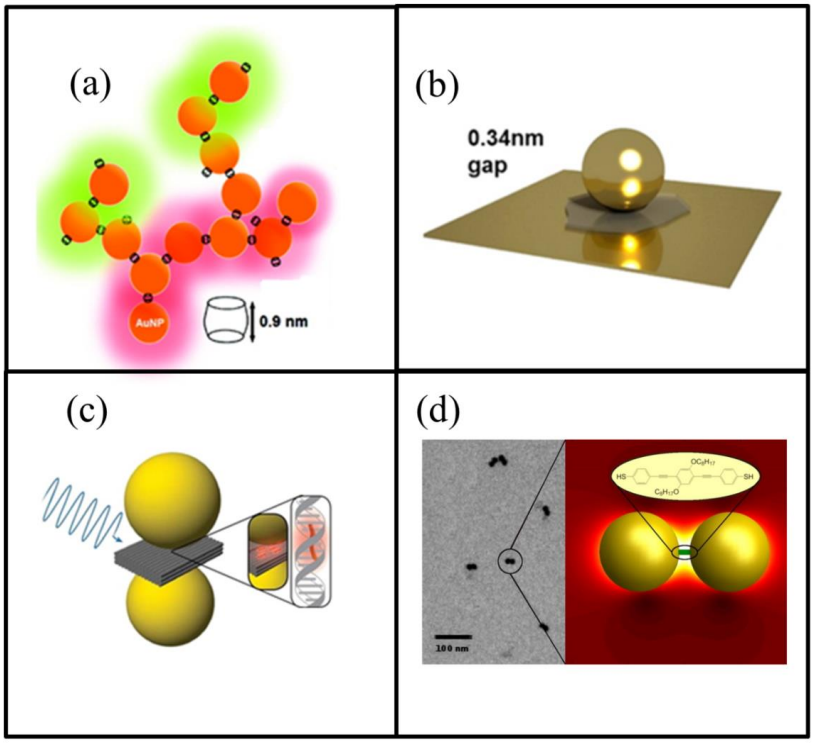

Fig. 2.23 (a) The Cucurbit[n]uril assisted metallic particle dimers [31]. (b) The graphene assisted gap mode structure [28]. (c) The DNA origami technique assisted metallic particle dimer [29]. (d) The rigid rod molecule assisted metallic particle dimer [30].

In 2011, Taylor *et al* proposed using Cucurbit[n]uril molecules to link gold nanoparticle, and 0.9 nm gap distance dimers were generated [31]. In 2012, Lee *et al*

studied the single molecule SERS by a DNA molecule linked gold particle dimer [75]. The gap distance can be adjusted from the original ~4.8 nm to less than 1 nm. The maximum electrical enhancement factor can be up to 5.9×10^{13} and the average enhancement factor is 1.8×10^{13} when the gap distance is below 1 nm. In 2013, Mertens *et al* reported a gap distance tuning method by graphene, one of the thinnest materials [28]. When single-layer graphene was inserted between 80 nm gold nanoparticle and gold substrate, a dimer made up of the gold particle and the gold particle image with 0.34 nm gap was formed. In 2014, Kuhler *et al* investigated a metallic particle dimer with the DNA origami technique [29]. The dimer is formed with two gold nanoparticles, which are linked by a three-layered DNA block. A dimer with 6 nm gap is obtained, and the technique shows great performance in enhancing Raman signals. In 2015, Fruhnert *et al* investigated a metallic nanoparticle dimer whose dimer particles are linked by a rigid rod molecule [30]. They obtained optical and geometrical properties of the molecule through efficient SERS measurement.

However, these methods mainly introduced fillers between the two dimer particles to obtain a nanoscale gap. The fillers themselves are likely to be measured in the SERS measurement. These may limit the applications and can become sources of noise during measurements. Empty gap is highly desirable for reproducible measurements. In order to obtaining an empty gap, controlling the metallic particles with external forces is needed. As possible solutions, optical manipulation techniques will be introduced in the following sections.

2.6 Optical tweezers

Optical tweezers is a modern technique for manipulating tiny objects with laser beam focusing. With this technique, objects can be attracted, held and moved by the force exerted on them. The force is usually at piconewton (pN) level, which makes biological cells, molecules and atoms totally controllable. Optical tweezers is facilitating research in many disciplines. Nowadays, this technique has been integrated to systems and developed to commercial products. For example, Optical Tweezers Raman Spectroscopy (OTRS) as a state-of-the-art technology has been invented to study a single cell in suspension [76-82]. The combination of Raman spectroscopy and optical trapping enables the manipulation and detection of samples to be performed in one system.

In this section, the history of optical tweezers will be firstly outlined briefly. Then the principles of optical tweezers will be described. Finally, optical trapping and rotation of metallic particles will be introduced.

2.6.1 History of optical tweezers

Optical tweezers belongs to the area of interaction between light and matter. In the early 17^{th} century, Kepler observed interesting phenomena when a comet passes by the sun. The closer a comet gets to the sun, the longer the comet tails are. In addition, the tails always directed away from the sun [83]. These reminded people of what Newton said: 'For every action force, there is a corresponding reaction force which is equal in magnitude and opposite in direction'. In 1873, Maxwell proposed the concept of optical radiation pressure based on his electromagnetic theory, then he proved the existence of optical radiation pressure after derivation of equations for calculating optical radiation pressure [84]. He then put forward his argument: 'In a

medium in which waves are propagated there is a pressure in the direction normal to the wave, and numerically equal to the energy contained in unit of volume'. Lebedev was the first to measure the pressure of light, by hanging an object on a filament [85], and the experiment confirmed the existence of optical radiation pressure. He was also the first to show that the pressure is twice as great for reflecting surfaces as for absorbing surfaces. In 1909, Einstein proposed an optical radiation pressure theory based on his study of linear polarized wave acting on homogeneous spherical particles. Nichols and Hull also measured the optical radiation pressure in the following years [86].

In the 1960s, the coherent light source laser with very high brightness was invented, and it brought revolutionary change to the studying of optical radiation. In 1969, through theoretical calculation, Ashkin pointed out that focused laser beam can push several micro-sized particles [87], and he demonstrated pushing transparent colloidal particles (diameter 0.6-2.5 μm) suspended in water away along the optical axial by using focused Argon ion laser beam. Meanwhile, he observed particles could be pulled into the beam center in the lateral direction. After making a lot of comparisons by repeated experiments using bubble and droplet, Ashkin thought lateral pulling force existed on the particle whose refractive index is higher than that of the ambient medium while lateral pushing force existed on the particle whose refractive index is lower than that of the ambient medium. In 1970, based on the study of these two opposite phenomena, Ashkin came up with the idea of trapping a particle by means of optical radiation. He tried two laser beams illuminating on the particle from two opposite directions. Finally, he achieved the trapping of the glass ball in aqueous solution. This series of work established the foundation of optical tweezers technique. In 1986, Ashkin *et al* found single beam laser is enough to make

a Three Dimensional (3D) trapping that attracts particle to the laser focus, and he built the first optical tweezers system. From then on, optical tweezers became known as single-beam optical gradient force trap [88].

2.6.2 Principles of optical tweezers

Basically, light not only has power but also has momentum according to the electromagnetic theory. When light illuminates an object, there is a momentum change due to the scattering of the incident photons, then an optical radiation pressure is exerted on the illuminated object. When the object is a transparent dielectric particle, there are reflections inside the particle, and a trapping force may be exerted on this particle. A typical optical tweezers system is formed through a laser beam being focused onto a particle by an objective lens. Take Gaussian beam as an example, as shown in Fig. 2.24.

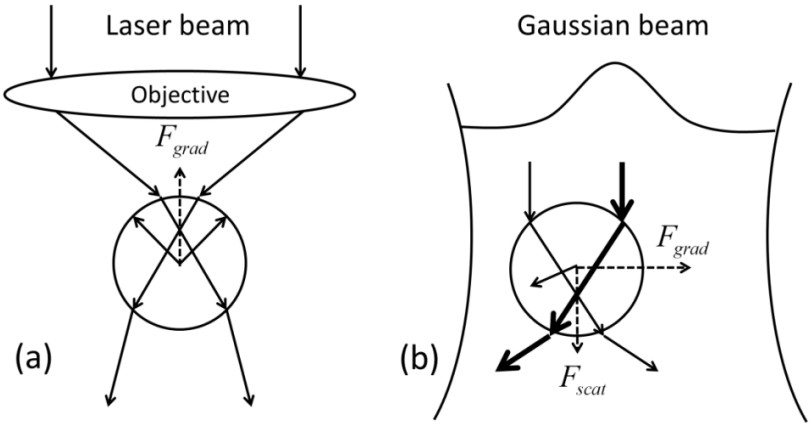

Fig. 2.24 Optical trapping principle schematic diagram, which consists of (a) axial trapping and (b) lateral trapping of a dielectric particle in a laser beam (Gaussian beam) focused by an objective. (a) The particle is in the optical axial offset of the laser's focal spot. (b) The particle is laterally offset to the optical axis.

Optical trapping can be broken down to two parts, namely, axial trapping and lateral trapping. In axial trapping, the particle will experience a force due to scattering and refraction [Fig. 2.24(a)]. The force is composed of two components.

One is scattering force, which usually pushes the particle along the light propagation direction. It is proportional to the Poynting vector of the optical field. The other is gradient force, which normally attracts the particle to the laser focus area. It is proportional to the gradient of the light intensity.

Lateral trapping is also indispensable for a 3D manipulation. The axial gradient force pulls the particle towards the focal spot, overcoming the scattering force, the gravity and the buoyancy of the particle. When the particle comes to the Gaussian laser beam, the light at the center of the beam is usually stronger than the light at the edge, so the gradient force will pull the particle to the center of the beam [Fig. 2.24(b)].

Fig. 2.25 shows a typical optical tweezers setup. According to the principles, the laser beam focused through the objective lens can be used to achieve optical trapping. A Charge Coupled Device (CCD) is used to record the movement of the trapped particle, and the recorded video is displayed on a monitor. A filter is then used to subtract the laser light, allowing only the illumination light to pass through.

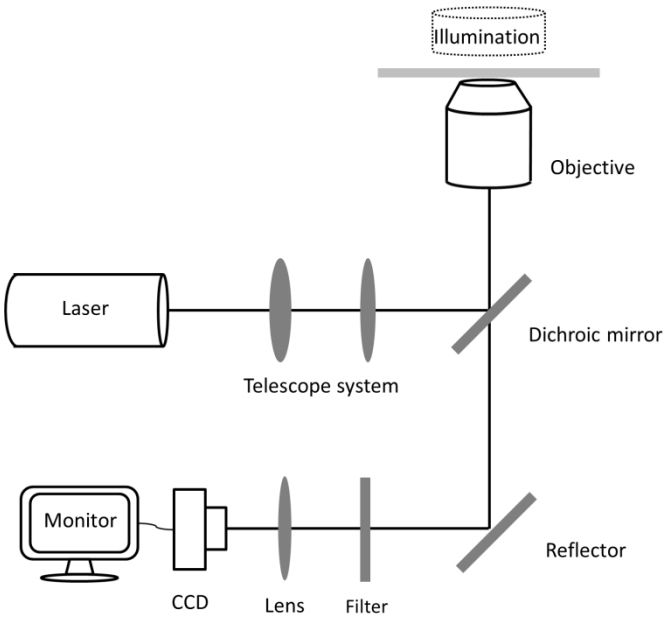

Fig. 2.25 The typical optical tweezers setup.

The size of the particle is an important factor in optical trapping. When the particle size is much larger than the wavelength of the incident laser (diameter $a \gg \lambda$), the particle is called Mie particle. The ray-optics method introduced in Fig. 2.24 can be used to explain optical trapping and this kind of geometric optics description can give a qualitative force analysis for a Mie particle.

Aside from the ray-optics method, Lorentz-Mie model is an alternative method for explaining the optical trapping of Mie particle [89]. Since this method is on the basis of Maxwell's equations, it is necessary to find the solution to the scattering problem by using corresponding boundary conditions. Then, we need to calculate the Mie coefficients and waveform factors relating to classical Mie scattering theory, so that we can calculate the laser scattering cross section on the particle. Lastly the resulting radiation pressure can then be obtained. The result by this method is reliable. However, computing and programming are complex. A simple description of this method is shown as follows.

If a laser beam propagates along the positive z direction and it illuminates a sphere particle, the scattering along the direction of optical axis can be expressed as [89]

$$C_{pr,z} = \frac{\lambda^2}{2\pi} \sum_{n=1}^{\infty} \left\{ \begin{array}{l} \dfrac{2n+1}{n(n+1)} \left| g_n \right| \mathrm{Re}\left(a_n + b_n - 2a_n b_n^{*}\right) \\ + \dfrac{n(n+2)}{n+1} \mathrm{Re}\left[g_n g_{n+1}^{*} \left(a_n + b_n + a_{n+1}^{*} + b_{n+1}^{*} - 2a_n a_{n+1}^{*} - 2b_n b_{n+1}^{*}\right)\right] \end{array} \right\} \tag{2.34}$$

where a_n and b_n are classical Mie scattering coefficients, which are associated with the size and material of the particle; and g_n is the beam waveform factor, which is associated with the wavelength and the beam waist. Note that the particle is at the center of the waist.

When the particle size is much smaller than the wavelength of the incident laser ($r \ll \lambda$), the particle is called Rayleigh particle, and the force can be calculated by treating the particle as a dipole. The gradient force and scattering force can be readily separated with this approximation. For a sphere with radius r, the gradient force arises from the interaction between the induced dipole with the inhomogeneous field (E) [90],

$$F_{grad} = -\frac{n_m}{2}\alpha \nabla E^2 \tag{2.35}$$

$$\alpha = n_m{}^2 r^3 \left(\frac{m^2 - 1}{m^2 + 2} \right) \tag{2.36}$$

where α is the polarizability of the sphere, n_m is the refractive index of the medium, and m (n_p / n_m) is the ratio of the refractive index of the sphere (n_p) to the refractive index of the medium (n_m). Also,

$$F_{scat} = \frac{I_0 \sigma n_m}{c} \tag{2.37}$$

$$\sigma = \frac{128\pi^5 r^6}{3\lambda^4} \left(\frac{m^2 - 1}{m^2 + 2} \right)^2 \tag{2.38}$$

where I_0 is the intensity of the incident light, σ is the scattering cross section of the sphere, c is the speed of light in vacuum and λ is the wavelength of the incident light [90].

When the particle size is comparable to the wavelength of the incident light (diameter $a \sim \lambda$), neither the ray-optics nor the dipole approximation is applicable. More complex theory is needed to give an accurate description. To study particles in optical field, there are some other theoretical research methods such as FDTD and Finite Element Method (FEM). Many commercial software have been developed following these methods, for example Rsoft and Comsol. MST method is based on

simulation or Lorentz-Mie model, and can be used for the calculation of optical force, and this will be discussed further in Section 3.3.

2.6.3 Optical trapping of metallic particles

It is generally accepted that it is hard to trap metallic particles with optical tweezers technique because of strong scattering from the metallic particles, which goes against optical trapping. There are still many reports about trapping metallic particles due to the importance of metallic particles. The review of optical trapping of metallic particles is mainly divided to two parts according to the size of the metallic particles. For Rayleigh metallic particles, they can be regarded as dipoles and the gradient force can be calculated by Eq. (2.35). Generating a sharply varying electric field in the focus is crucial for the trapping. For Mie metallic particles, the scattering force is dominant. Making use of the scattering force and transferring the scattering force to trapping force is crucial for the trapping. Literature for optical trapping of Rayleigh and Mie metallic particles will be reviewed in the following subsections.

2.6.3.1 Optical trapping of Rayleigh size metallic particles

In 1994, Svoboda *et al* reported single beam trapping of 36 nm gold nanoparticle [91]. They experimentally proved that the gradient force of a Rayleigh particle is proportional to its polarizability. They found the trapping force of a 36 nm gold particle is about 7 times stronger than that of a 38 nm dielectric particle, because the ratio of the trapping forces is equal to the ratio of their polarizabilities. In 2005, Hansen *et al* reported single beam trapping of diameter 18~254 nm gold nanoparticles [92]. They found that trapping becomes more difficult with increasing size in the range under 100 nm. For particles with size over 100 nm, the increase in

trap stiffness with particle size becomes less steep. In 2008, Bosanac *et al* reported 3D trapping of 20~275 nm silver nanoparticles [93], which was achieved by reducing spherical aberrations at the focus. Through quantitative force analysis, they found the optical force increases with the size of the particle. In 2004, Zhan proposed a novel method for trapping of metallic Rayleigh particles with RPB [94]. As mentioned previously, the longitudinal component is dominant in focused RPB field. At the focal spot, a metallic Rayleigh particle can be vastly polarized, and then strong gradient force can be generated. The calculated focal components of strongly focused RPB are shown in Fig. 2.26.

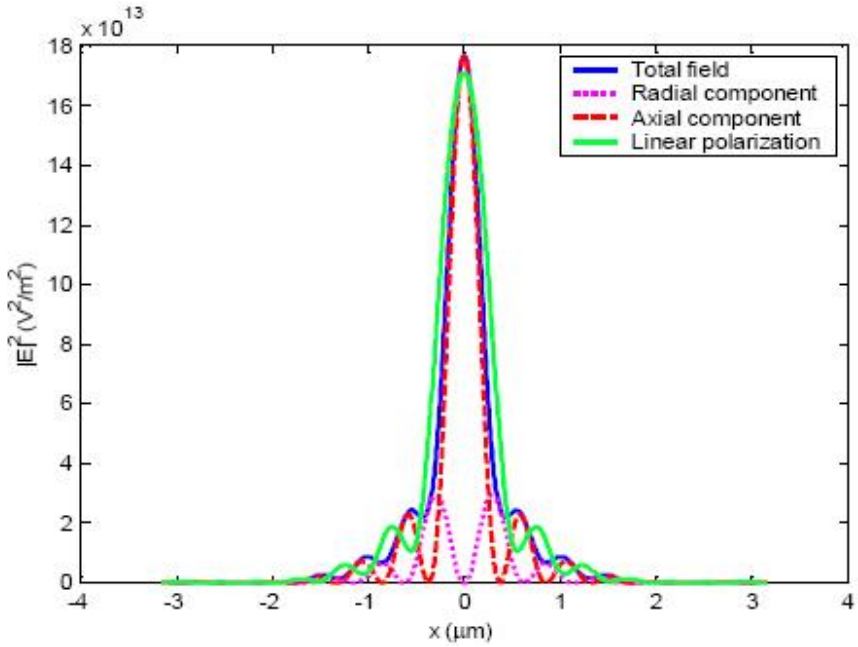

Fig. 2.26 Calculated focal components of strongly focused RPB. [94]

For Rayleigh metallic particles (with radius $a<<\lambda$, where λ denotes the incident wavelength), stable trapping using optical tweezers is possible for particles with diameter from 18 nm to 254 nm , where scattering forces are small because of sub-wavelength particle sizes, and thus easily overcome by gradient forces [78, 92, 94]. The increasing of laser power or beam shaping of the laser beam can be used to gain enough gradient force for the trapping. Regardless, the trapping of Rayleigh size

metallic particles by optical tweezers technique has high requirement of the laser beam.

2.6.3.2 Optical trapping of Mie size metallic particles

In 1992, Sasaki *et al* used scanning laser method to achieve trapping of micro size metallic particle [95]. This is the earliest work of metallic particle trapping. As shown in Fig. 2.27, the circularly scanning laser beam pushes other metallic particles away while it constrains a metallic particle inside the circle where the laser focus spot passes.

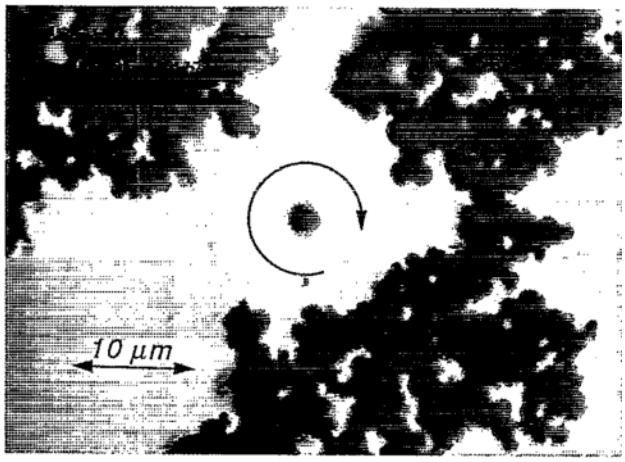

Fig. 2.27 Scanning laser beam trapping technique for metallic particles. [95]

In 1994, Sato *et al* experimentally achieved two dimensional trapping of the micro sized metallic particles by using a fixed single laser [96]. As shown in Fig. 2.28(a), the laser beam focal spot is set at the bottom of the particle. Pulling force will be generated towards the focal center of the incident beam in the horizontal plane. Then the particle can be manipulated in two dimensions. In contrast, as shown in Fig. 2.28(b), the laser beam is focused on the center of the particle, and as expected, the particle will be pushed away.

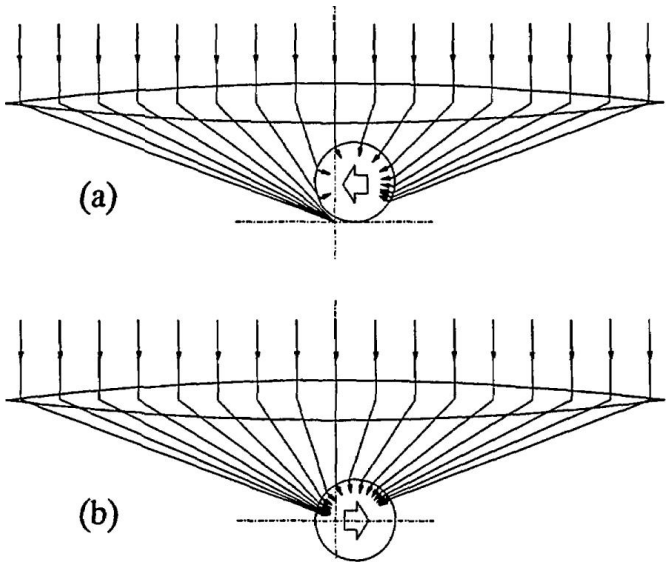

Fig. 2.28 Laser beam was focused to (a) bottom and (b) top of metallic spheres respectively. [96]

In 1998, Furukawa *et al* achieved trapping of 0.5~3 μm gold particles using single Gaussian light beam [97]. Their method is similar to the method in [96]. They found the scattering force exerted on a gold particle can point towards the beam axis, as shown in Fig. 2.29(b).

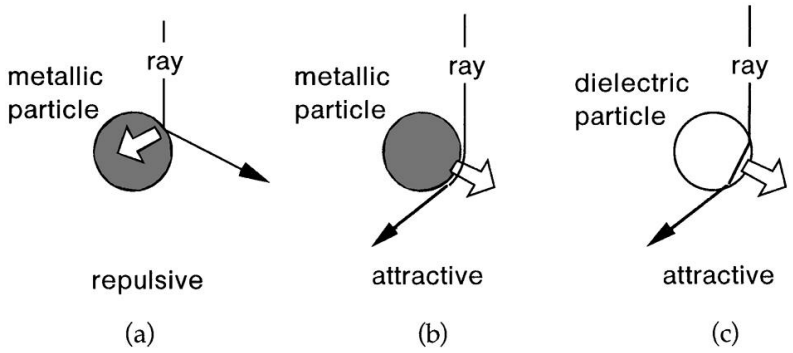

Fig. 2.29 (a) Pushing force is generated when laser beam is focused to the inside of the metallic particle, (b) pulling force is generated when laser beam is focused to the bottom of the metallic particle, and (c) pulling force is generated when laser beam is focused to the inside of the dielectric particle. [97]

In 2000, Gu *et al* reported using obstructed laser beam to enhance the transverse trapping of metallic particles [98]. The obstructed laser beam is generated with an opaque disk, as shown in Fig. 2.30. The focusing of rays at the edge will push the metallic particle to the center, where the metallic particle is confined.

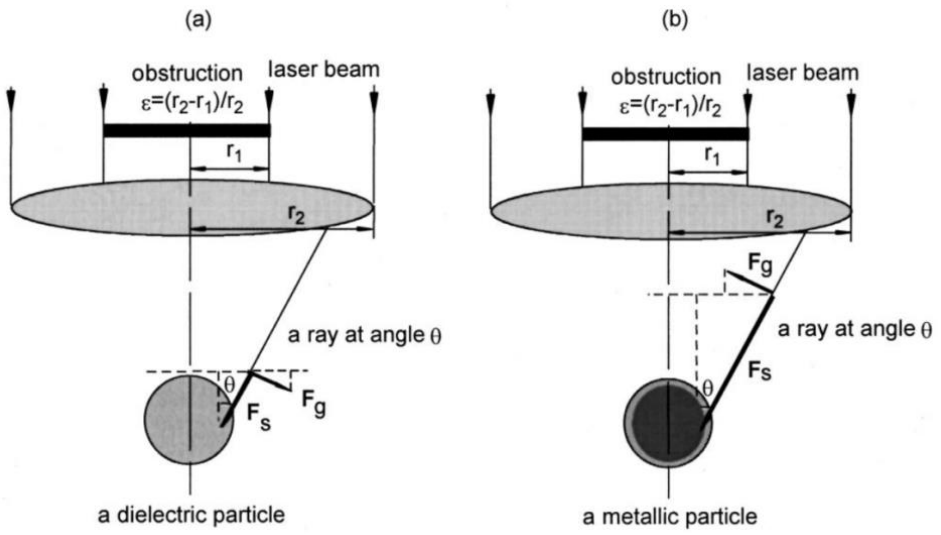

Fig. 2.30 Simple models for two different configurations of trapping of (a) dielectric particle and (b) metallic particle. [98]

Although several special optical tweezers rely on the scattering force to confine Mie metallic particles in a ring-shaped potential well [95, 96, 98, 99], in practice these methods suffer drawbacks, such as high-precision requirements in shaping and adjusting the laser beams and narrow trapping regions. In addition, since scattering force is utilized, the trapping of Mie size metallic particles by optical tweezers technique is not stable. The trapping is mainly two dimensional and thus it is not an active way.

2.6.4 Optical rotation of metallic particles

Optical rotation of particles is another optical manipulation form. Optical vortex regarded as optical spanner can cause the optical rotation of particles, which has potential applications in micro-fluidics devices.

In 2007, Zhao *et al* used tightly focused circularly polarized optical vortex to rotate metallic particles [100]. Due to the high absorption of metallic particles, they were used to represent the OAM of the focused beam since rotation speed is positively related to the OAM of the focused beam, which is in turn associated with

the topological charge of the optical vortex. As shown in Fig. 2.31, the difference between the rotations of metallic particles in right and left circularly polarized optical vortex proves the optical spin-to-orbital angular momentum conversion.

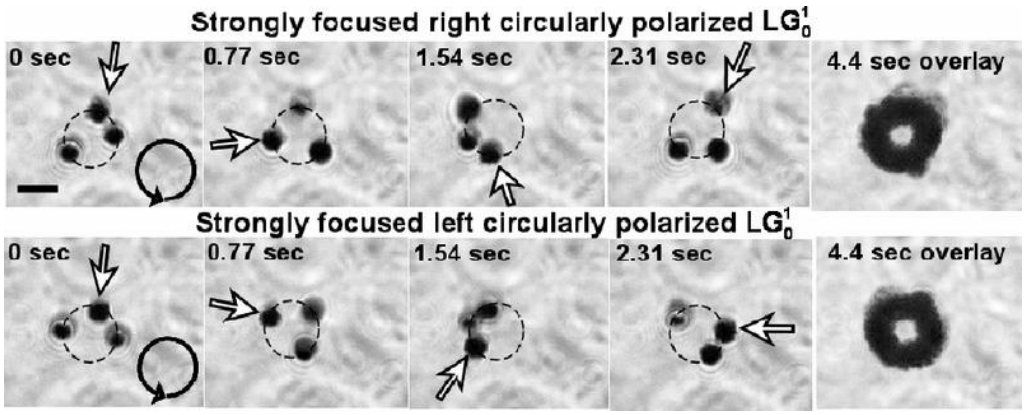

Fig. 2.31 Successive images of a video recording the rotation of three gold particles (diameter: 3.0~5.5 μm), which are trapped by tightly focused circularly polarized optical vortex. The scale bar is 5 μm. The circle arrows indicate the rotation directions. The rightmost panels show the rotation trajectory overlaying of 40 frames in 4.4 s. [100]

However, the rotation was not steady, and this can be clearly seen in the rightmost panels. That the distances among the metallic particles always change indicates the trapping was not stable.

In 2008, Dienerowitz *et al* reported the trapping of metallic nanoparticles in optical vortex [101], as shown in Fig. 2.32. The nanoparticles are confined at the dark core area of the focused optical vortex. Since the size of the particles is much smaller than that of the dark core, the trapped two particles have no interaction in the center of the dark core.

In 2015, Zhang *et al* performed the experiments of metallic particles in optical vortex. Metallic particle could be pushed away due to the strong scattering from the bright ring of the optical vortex, as shown in Fig. 2.33(a). Metallic particle could be trapped and rotated inside the bright ring of the optical vortex [Fig. 2.33(b)]. Only single metallic particle manipulation was demonstrated in this work. The

trapping and rotation of multiple metallic particles in optical vortex will be studied. These will be introduced in Chapter 6.

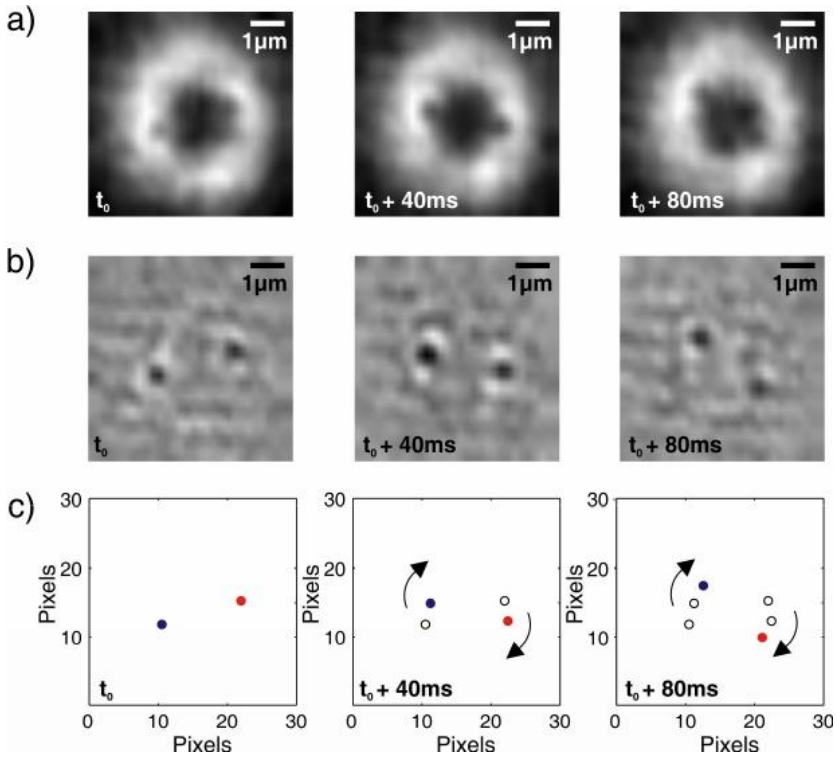

Fig. 2.32 Three subsequent pictures showing the rotation of two trapped 100 nm gold nanoparticles in optical vortex. Displayed in row (a) are the noise-reduced movie stills out of a video sequence that are further processed with a background subtraction in row (b). Points are used to represent the particles in row (c). [101]

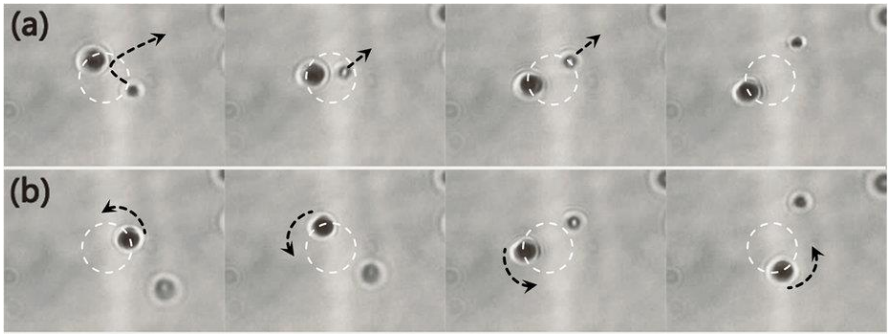

Fig. 2.33 (a) Repulsive interaction between optical vortex and a gold particle. The dotted arrow indicates the particle is pushed away. The two particles are the same size but located at different distances from the focal plane. (b) Rotation of a gold particle in the focused optical vortex field. [102]

In these previous studies, the rotation of metallic particles is not steady in terms of rotation path and speed. The steadiness of the rotation needs to be improved.

Also, the trapped metallic particles in the experiments of all previous studies were individual particles. The trapping of multiple metallic particles need to be further investigated.

2.7 Plasmonic tweezers

Surface plasmon can break the optical diffraction limit and has near-field enhancement effect. With these two characteristics, it can improve the performance of the traditional optical device, induce many novel physical phenomena, and realize new device functionality. Developed in the last ten years, plasmonic tweezers is a novel technique in optical manipulation using surface plasmon. The surface plasmon field can significantly improve the gradient force, greatly reduce the requirement of the intensity of light source, and solve the problem of weak field in the evanescent wave tweezers system. LSP excited among metallic particles can have a coupling with the surface plasmon excited in the plasmonic tweezers system, thus enhancing the electric field and the gradient force. Therefore, particles are more easily to trap by plasmonic tweezers.

2.7.1 Plasmonic force

Optical tweezers based on surface plasmon has attracted more and more attention from researchers in the world. In recent breakthroughs, the research of surface plasmon optical force is fundamental.

In 2001, Song *et al* theoretically studied the forces on the metallic and dielectric microspheres in the surface plasmon field [103], as shown in Fig. 2.34. Based on Lorenz-Mie model, they found that the gradient force generated within the surface plasmon field can be improved by 1~2 orders of magnitude compared to that generated within the evanescent wave field. They also found that the force exerted

on metallic particles is 1~2 orders of magnitude higher than that exerted on dielectric particles. This is the first theoretical demonstration of the feasibility of optical manipulation based on surface plasmon.

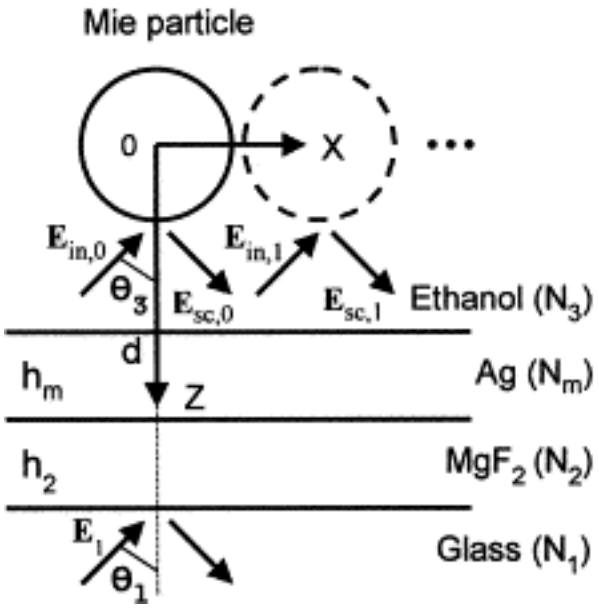

Fig. 2.34 Schematic diagram of the calculation model in [103]. A Mie particle is close to a system of multilayer films.

In 2006, Quidant's group from the institute of photonic sciences in Spain observed the plasmonic force exerted on a micro sized dielectric particle [104]. This is the first time plasmonic force was observed experimentally. They found the closer the particle gets to the metal surface the faster the growth ratio of tangential force. Fig. 2.35 shows the plasmonic forces of the dielectric particle when it approaches the metal surface.

In 2009, Wang *et al* experimentally demonstrated the enhanced pushing force on gold nanoparticles by SPPs [105], as shown in Fig 2.36. Their FDTD simulation results indicate the enhanced force comes from the near-field SPP-LSP coupling between the gold particles and the film. Since the excited SPPs are in propagating status, only propulsion was achieved.

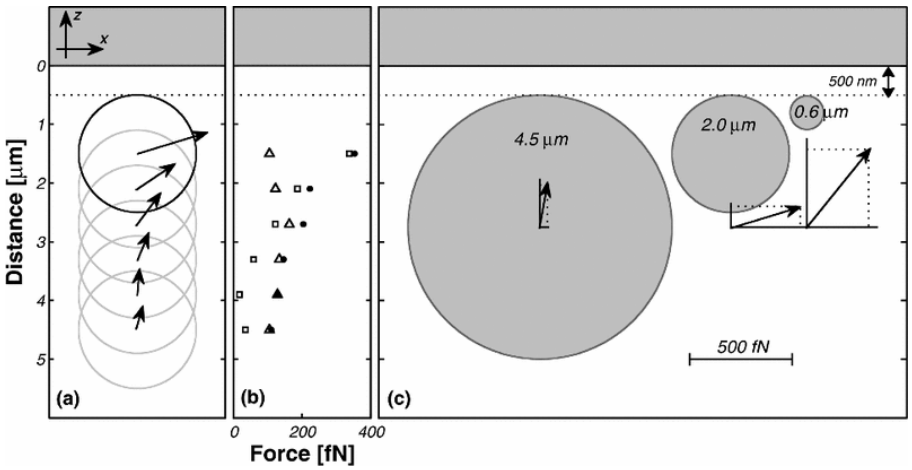

Fig. 2.35 (a) Force vector and (b) module (circles), x component (squares), and z component (triangles) of the force versus distance from the surface for a 2.0 μm bead. (c) Force on beads of different sizes placed at 500 nm from the surface. [104]

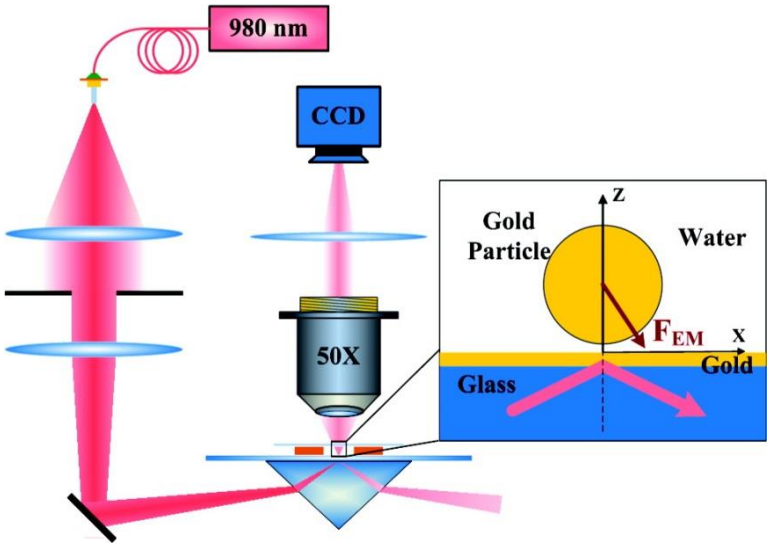

Fig. 2.36 The schematic setup for demonstrating surface plasmon force based on ATR structure [105].

2.7.2 Plasmonic tweezers through metal structures

Quidant's group continued to study the surface plasmon optical tweezers. In 2007, they experimentally achieved the capture and arrangement of micro-sized particles by using surface plasmon disc array structure [21], as shown in Fig. 2.37. Trapping multiple particles with this kind of pattern on metal film is ascribed to LSPR effects on the discs. The experimental trapping requires low incident laser

power. Based on their work, they formally proposed the concept of surface plasmon optical tweezers, also known as plasmonic tweezers.

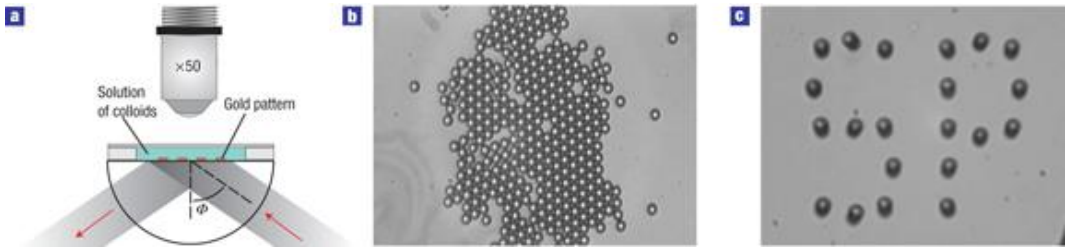

Fig. 2.37 (a) Schematic diagram of surface plasmon tweezers array; (b, c) the experiment results using this SP tweezers. [21]

In 2010, Zhang *et al* experimentally demonstrated the trapping of a 10 nm metallic particle using surface plasmon dipole antenna structure [22]. As shown in Fig. 2.38, the hot-spot structure in their system is capable of trapping nano-sized particles.

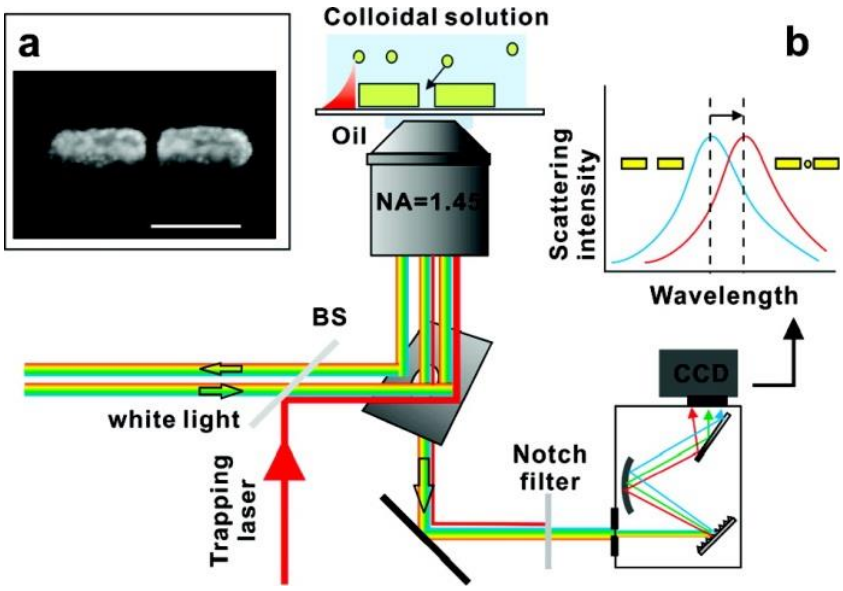

Fig. 2.38 The experimental schematic of plasmonic tweezers using nanoantenna structure. (a) SEM image of a typical nanofabricated antenna with a 10 nm gap. The scale bar is 100 nm. (b) Schematic drawing of the experimental setup. [22]

In 2011, Crozier's group experimentally studied the surface plasmon optical trapping effect using gold pillar structure. They found 110 nm dielectric particles can be trapped and rotated around the gold pillar [23]. As shown in Fig. 2.39(a), position

of the trapped polystyrene sphere around the gold pillar changes along with the polarization direction of the incident light.

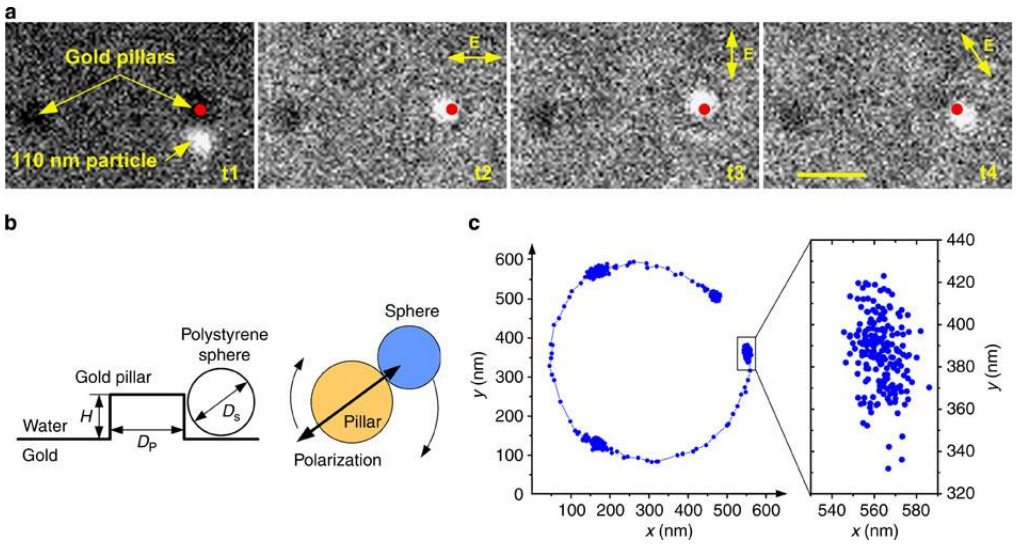

Fig. 2.39 Plasmonic trapping of dielectric particles using pillars structure on gold surface. (a) Fluorescence images, obtained at successive times, of trapping and rotating 110 nm diameter polystyrene sphere by gold nanopillar. At time t1, sphere is close to nanopillar, but not trapped. At times t2, t3 and t4, sphere is trapped by nanopillar. Input polarization is manually rotated, resulting in sphere rotating clockwise about pillar. Red dots represent positionand size of nanopillar. Scale bar, 2 μm. (b) Schematic illustration of trapping and manual rotation of nanosphere by gold nanopillar with linearly polarized illumination. D_p=280 nm and H=130 nm. (c) Left: Centroid of trapped sphere (D_s=200 nm) while polarization is being manually rotated. Right: centroid of trapped sphere measured without polarization rotation. [23]

Developed about ten years ago, plasmonic tweezers has become rapidly developing optical manipulation technique, although international research on plasmonic tweezers is still in its infancy. There are still a lot of scientific problems and potential applications deserving of study.

2.8 Summary

In this chapter, the concepts of SPPs and LSPs were reviewed. Their excitation mechanisms will be beneficial for explaining the surface plasmon coupling in the interactions among metallic particles and metal film. Then the RPB

and its application in surface plasmon excitation in the laser focusing system were reviewed. Next, the SERS mechanisms and structures were reviewed. The localized enhanced electric field around metallic particles can be used to enhance Raman signal. Compared to other nanostructures such as nanoprobes and nanoantennas, metallic particles can be used for intracellular measurement. In order to measure a full cell, the movement of metallic particles needs to be controlled. However, optical trapping of metallic particles is hard, especially for big-sized metallic particles, a topic which has been discussed in subsection 2.6.3. As a potential solution, the plasmonic tweezers was reviewed. Reviewed in subsection 2.7.2, previous studies about plasmonic tweezers are mainly based on nanostructures. The structures used are fixed and need complex fabrication techniques, hence they cannot satisfy the requirement of dynamic manipulation. Therefore, focused plasmonic tweezers method was proposed to solve this problem, which will be discussed further in Chapter 3. In addition, metallic particle dimer application in SERS was also reviewed. Both theoretical and experimental studies indicate gap distance and the orientation of the dimer are crucial for the electric field enhancement. In order to study these two issues, plasmonic trapping of horizontally- and vertically- oriented metallic particle dimers were proposed, which will be discussed further in Chapter 4 and Chapter 5, respectively.

Chapter 3 Focused plasmonic trapping of metallic particles

3.1 Introduction

Besides the applications introduced in section 3.1, metallic particles have extensive applications including biotechnology and micro-fabrication [1]. This strongly motivates the development of trapping and manipulation technologies for metallic particles. Optical tweezers, one of the contenders of trapping technologies, has naturally become the first choice because of its tremendous success in trapping dielectric particles. However, optical tweezers is not always successful in trapping metallic particles. In contrast, optical tweezers usually pushes metallic mesoscopic particles (diameter $a \sim \lambda$) and Mie particles away from the light spot, because scattering forces strengthen more rapidly than gradient forces [106].

In recent years, plasmonic tweezers, based on SPPs excited in metal nanostructures, have exhibited an enhanced attractive force for both dielectric and metallic particles [21, 22, 104, 105, 107-110]. This provides a potential mean for trapping and manipulating metallic particles. In this chapter, a variant of the plasmonic tweezers for trapping and manipulating metallic particles that is based on a highly focused plasmonic field on a flat metal film excited by a RPB (also called SP-VP [111-113]) will be reported [24]. This variant (see Fig. 3.1) can attract and trap both Rayleigh and Mie metallic particles. Trapping of mesoscopic-sized particles (diameter $a \sim \lambda$) is particularly successful. 1 μm metallic particle can be trapped by focused plasmonic tweezers will be theoretically demonstrated.

To determine the plasmonic force, a 3D FDTD calculation was performed to obtain the electric field distribution around the particle. Furthermore, the MST

method was applied to analyse the gradient and scattering forces exerted on the particle for both types of tweezers. The resultant total force in optical tweezers is composed of weakly attracting gradient forces and a stronger repulsive scattering force. Contrary to common assumptions, it was found in the numerical analysis that the resultant total force in plasmonic tweezers is the result not of a stronger gradient force dominating an opposing scattering force, but instead of a dominant gradient force assisted by a weak scattering force acting in the same direction. In focused plasmonic tweezers system, the dominant gradient force originates with the coupling between a greatly enhanced surface plasmon field and metallic particles, whereas the unusual scattering force is due to pushes exerted through focused SPPs propagation.

Focused plasmonic tweezers not only has capability of trapping metallic spheres, but also has potential in trapping and manipulating other shape objects, such as nanowires or even complex metal structures. Compared with other plasmonic tweezers system based on metallic microdiscs or bowtie structures [22, 109, 110], focused plasmonic tweezers system benefits from the structureless excitation of SPPs in a dynamic configuration, thereby reduces the need to fabricate complex nano-sized structures.

3.2 Surface plasmon virtual probe

3.2.1 Surface plasmon virtual probe generation configuration

The most important part in the focused plasmonic tweezers is generating SP-VP. Fig. 3.1 is the schematic diagram of focused plasmonic tweezers system. Focused RPB has a transverse-magnetic polarization with respect to the metal film, SPPs can be excited on a metal film at a Surface Plasmon Resonance (SPR) angle, resulting in a near-zero reflection. When the gold film is located before the focal

plane of the objective lens, the excited SPPs will act as a secondary circular source propagating towards the center. As a result, a sharp peak (virtual probe) of ultra-high intensity is formed at the center by constructive superposition of SPPs. The SP-VP can serve as a highly concentrated source to trap metallic particles, which is similar to hot-spot in the metallic bowtie trapping structure.

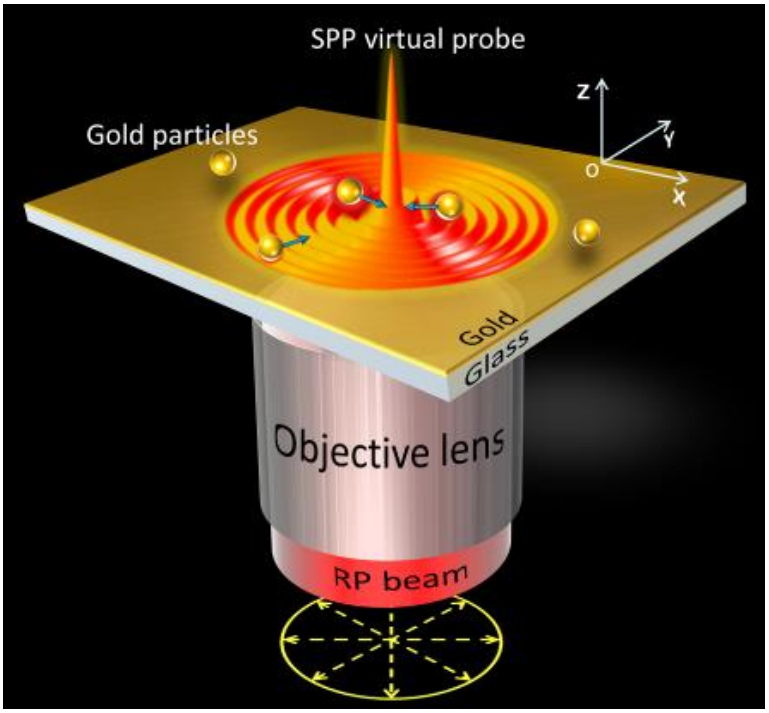

Fig. 3.1 Schematic diagram of focused plasmonic tweezers system: bottom yellow arrows indicate the polarized directions of the RPB, blue arrows indicate the direction of force on each gold particle in the plasmonic field.

3.2.2 Simulation of the surface plasmon virtual probe

Have known the configuration for the SP-VP generation, we can perform the simulation of the SP-VP using the structure and parameters of the configuration. For characterization of the electric field of near-field, many theoretical analysis methods such as Green's tensor [114, 115], plasmon hybridization [116, 117], multiple-scattering [118], FDTD [116, 119], and FEM [120] have been previously used. In this thesis, FDTD method was used to simulate the system by using a commercial

FDTD software (Rsoft v8.1). The excitation source, RPB, a special vector beam cannot be obtained in the software directly. We need to establish the model of the RPB first.

RPB can be calculated as a user defined light source in the software with the following derivation. Mathematically, a left-handed and right-handed circularly polarized beam can be expressed as

$$\vec{E}_{LHC} = A(r)\frac{\vec{e}_x + i\vec{e}_y}{\sqrt{2}} = \frac{A(r)}{\sqrt{2}} e^{i\phi}\left(\vec{e}_r + i\vec{e}_\phi\right) \tag{3.1}$$

$$\vec{E}_{RHC} = A(r)\frac{\vec{e}_x - i\vec{e}_y}{\sqrt{2}} = \frac{A(r)}{\sqrt{2}} e^{-i\phi}\left(\vec{e}_r - i\vec{e}_\phi\right) \tag{3.2}$$

RPB can be achieved by the superposition of a left-handed circularly polarized beam and a right-handed circularly polarized beam with a 2φ phase difference, where φ is the azimuthal angle,

$$\vec{E}_{Radial} = \vec{E}_{LHC}e^{-i\phi} + \vec{E}_{RHC}e^{i\phi} = \sqrt{2}A(r)\vec{e}_r \tag{3.3}$$

With Eq. (3.3), RPB can be loaded in the software with common optical beams. Then FDTD simulation of near-field intensity distribution of the virtual probe on a thin gold film was presented. This can be used to study the characteristics of the SP-VP.

Fig. 3.2 shows the electric field distribution of surface plasmon on gold film. In the simulation, the incident wavelength (λ_0) is 1064 nm, the NA of the objective is 1.49, the refractive index of the glass substrate is 1.515, and the thickness of the thin gold film is 45 nm. The theoretical Full Width at Half maximum (FWHM) of the SP-VP is 261 nm (~0.245 λ_0).

The integral of the MST method is used to calculate the force, since it is definite integral and as long as the simulation results are converged, the force after

the integral should be converged. For example, when calculating the results in Fig. 3.2, a time monitor of the Ez component was set, a computing time (cT, in unit of μm) of 15 μm was employed to guarantee the convergence for the simulation. As shown in Fig. 3.3, the recorded monitor value became invariable after 9 μm.

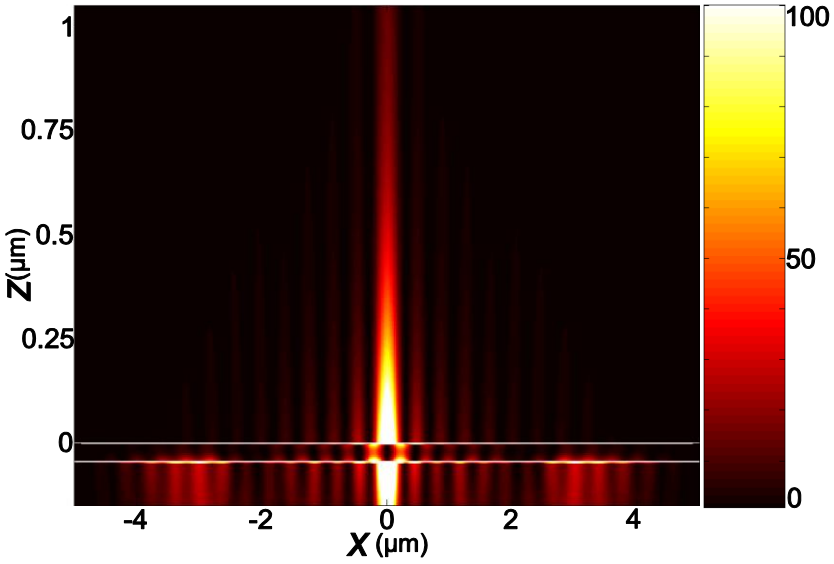

Fig. 3.2 The intensity distribution of electric field of a SP-VP in x-z plane at y=0, the while lines show the profile of gold film.

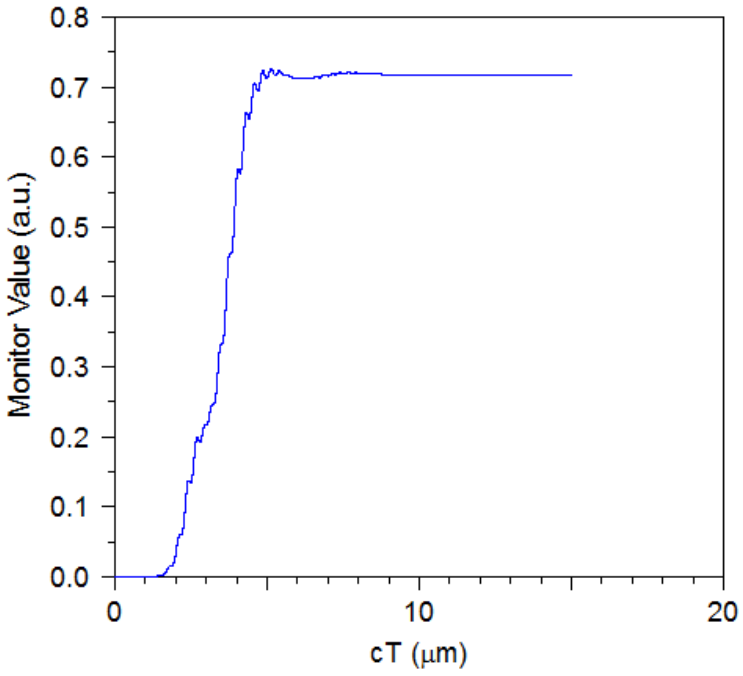

Fig. 3.3 The time mintor result in one computing process of FDTD simulation.

3.3 Force analysis methods for metallic particles

3.3.1 Total force calculation method

In order to demonstrate the focused plasmonic trapping of metallic particles, we need to calculate the optical force exerted on the particle. Thus a derivation of the total electromagnetic force on the particle was done.

The electromagnetic force on particle is the Lorentz force:

$$\vec{f} = \rho\vec{E} + \vec{J} \times \vec{B} \tag{3.4}$$

Dynamical Coulomb force (gradient or polarization force):

$$\vec{F}_{grad}(t) = \int_v \rho(\vec{r},t)E(\vec{r},t)dv \tag{3.5}$$

Dynamical Laplace force (scattering force):

$$\vec{F}_{scat}(t) = \frac{1}{c}\int_v \vec{j}(\vec{r},t) \times \vec{H}(\vec{r},t)dv \tag{3.6}$$

According to the inhomogeneous Maxwell equations:

$$\begin{cases} \nabla \bullet \vec{E} = \rho / \varepsilon \\ \nabla \bullet \vec{B} = \mu\vec{J} + \mu\varepsilon\dfrac{\partial\vec{E}}{\partial t} \end{cases} \tag{3.7}$$

then Eq. (3.4) becomes

$$\vec{f} = \varepsilon(\nabla \bullet \vec{E})\vec{E} + \frac{1}{\mu}(\nabla \times \vec{B}) \times \vec{B} - \varepsilon\frac{\partial\vec{E}}{\partial t} \times \vec{B} \tag{3.8}$$

Because $\dfrac{\partial(\vec{E} \times \vec{B})}{\partial t} = \dfrac{\partial\vec{E}}{\partial t} \times \vec{B} + \vec{E} \times \dfrac{\partial\vec{B}}{\partial t} = \dfrac{\partial\vec{E}}{\partial t} \times \vec{B} + \vec{E} \times (-\nabla \times \vec{E})$, then Eq. (3.8) yields:

$$\vec{f} = \varepsilon(\nabla \bullet \vec{E})\vec{E} + \frac{1}{\mu}(\nabla \times \vec{B}) \times \vec{B} - \varepsilon\frac{\partial(\vec{E} \times \vec{B})}{\partial t} - \varepsilon\vec{E} \times (\nabla \times \vec{E}) \tag{3.9}$$

$$\vec{f} = \varepsilon[(\nabla \bullet \vec{E})\vec{E} - \vec{E} \times (\nabla \times \vec{E})] + \frac{1}{\mu}(\nabla \times \vec{B}) \times \vec{B} - \varepsilon\frac{\partial(\vec{E} \times \vec{B})}{\partial t} \tag{3.10}$$

$$\vec{f} = \varepsilon[(\nabla\bullet\vec{E})\vec{E} - \vec{E}\times(\nabla\times\vec{E})] + \frac{1}{\mu}[(\nabla\bullet\vec{B})\vec{B} - \vec{B}\times(\nabla\times\vec{B})] - \varepsilon\frac{\partial(\vec{E}\times\vec{B})}{\partial t} \quad (3.11)$$

Using vector calculus identity $\frac{1}{2}\nabla(\vec{A}\bullet\vec{A}) = \vec{A}\times(\nabla\times\vec{A}) + (\vec{A}\bullet\nabla)\vec{A}$, we have

$$\vec{f} = \varepsilon[(\nabla\bullet\vec{E})\vec{E} + (\vec{E}\bullet\nabla)\vec{E} - \frac{1}{2}\nabla E^2] + \frac{1}{\mu}[(\nabla\bullet\vec{B})\vec{B} + (\vec{B}\bullet\nabla)\vec{B} - \frac{1}{2}\nabla B^2] - \varepsilon\frac{\partial(\vec{E}\times\vec{B})}{\partial t} \quad (3.12)$$

$$\vec{f} = \varepsilon[\nabla(\vec{E}\vec{E}) - \frac{1}{2}\nabla(\vec{I}E^2)] + \frac{1}{\mu}[\nabla(\vec{B}\vec{B}) - \frac{1}{2}\nabla(\vec{I}B^2)] - \varepsilon\frac{\partial(\vec{E}\times\vec{B})}{\partial t} \quad (3.13)$$

Because $\vec{E}\vec{E}$ and $\vec{B}\vec{B}$ are tensors and $\vec{I}$ an unit tensor, we obtain

$$\vec{f} = \nabla[\varepsilon(\vec{E}\vec{E}) - \frac{\varepsilon}{2}\vec{I}E^2 + \frac{1}{\mu}(\vec{B}\vec{B}) - \frac{1}{2\mu}\vec{I}B^2] - \varepsilon\frac{\partial(\vec{E}\times\vec{B})}{\partial t} \quad (3.14)$$

Using the Poynting vector $\vec{S} = \vec{E}\times\vec{H} = \frac{1}{\mu}\vec{E}\times\vec{B}$, we have

$$\vec{f} = \nabla\bullet\vec{\vec{T}} - \varepsilon\frac{\partial(\vec{E}\times\vec{B})}{\partial t} = \nabla\bullet\vec{\vec{T}} - \varepsilon\mu\frac{\partial\vec{S}}{\partial t} \quad (3.15)$$

where $\vec{\vec{T}} = \varepsilon\varepsilon_0\vec{E}\vec{E} + \mu\mu_0\vec{H}\vec{H} - \frac{\vec{I}}{2}(\varepsilon\varepsilon_0\left|\vec{E}\right|^2 + \mu\mu_0\left|\vec{H}\right|^2)$ represents the MST matrix. In scalar form, the MST matrix is written as $\sigma_{ij} = \frac{1}{4\pi}[E_iE_j + H_iH_j - \frac{1}{2}(E^2 + H^2)\delta_{ij}]$, where δ_{ij} is Kronecker delta.

Thus, the total electromagnetic force (Lorentz force) on the particle can be described as

$$\vec{F} = \int_v \vec{f}\bullet dv = \int_v \nabla\bullet\vec{\vec{T}}dv - \varepsilon\mu\int_v \frac{\partial\vec{S}}{\partial t}dv \quad (3.16)$$

According to the divergence theorem $\int_v \nabla\bullet\vec{A}dv = \oint_s \vec{A}\bullet\vec{n}ds$, Eq. (3.16) becomes

$$\vec{F} = \oint_s \vec{\vec{T}} \bullet \vec{n} ds - \varepsilon\mu \frac{\partial}{\partial t} \int_v \vec{S} dv \tag{3.17}$$

In a static electromagnetic field, $\frac{\partial \vec{S}}{\partial t} = 0$ after time-averaging, the total averaged force is

$$\left\langle \vec{F} \right\rangle = \left\langle \oint_s \vec{\vec{T}} \bullet \vec{n} ds \right\rangle \tag{3.18}$$

where $\vec{n}$ is the unit normal perpendicular to the small area ds on the particle surface.

For the MST method, denoting the three force components by F_x, F_y, and F_z, the time-average force <F> can be written as [121]:

$$\langle F \rangle = \oint \left\{ \frac{\varepsilon}{2} Re[(\vec{E} \bullet \vec{n})\vec{E}^*] - \frac{\varepsilon}{4}(\vec{E} \bullet \vec{E}^*)\vec{n} + \frac{\mu}{2} Re[\mu(\vec{H} \bullet \vec{n})\vec{H}^* - \frac{\mu}{4}(\vec{H} \bullet \vec{H}^*)\vec{n} \right\} ds \tag{3.19}$$

where ε and μ are the permittivity and permeability of the medium around the particle, respectively, and $\vec{n}$ is the unit normal perpendicular to the integral area ds. The electric and magnetic field components required in the MST method are obtained directly from the FDTD simulation data.

3.3.2 Gradient/scattering forces calculation method

The MST method only gives the total electromagnetic force exerted on the particle. To understand the different mechanisms underlying the two types of tweezers, we need to further separate the total electromagnetic force into gradient and scattering forces. For Rayleigh metallic particles, it is easy to calculate these two forces using the dipole approximation model [94]. However, it is not suitable for

mesoscopic and Mie metallic particles. Here, an alternative method to calculate these forces for mesoscopic/Mie metallic particles based on the MST method is developed. The derivation of the gradient and scattering forces is shown as follows.

According to classical electromagnetic theory, the total electromagnetic force is Lorentz force as shown in Eq. (3.4). The gradient force relating to the electric field and the scattering force relating to the magnetic field are shown as Eqs. (3.5) and (3.6) respectively.

The gradient force is essentially a Coulomb force that depends on the local electric field and the charge density induced in particle. The scattering force is a Laplace force related to local magnetic field. Thus, the electric field force (gradient force) component of the Lorentz force can be expressed as in Eq. (3.5). According to Eq. (3.8), we obtain:

$$\vec{f}_{grad} = \varepsilon(\nabla \bullet \vec{E})\vec{E} = \varepsilon(\frac{\partial E_x}{\partial x} + \frac{\partial E_y}{\partial y} + \frac{\partial E_z}{\partial z}) \begin{pmatrix} E_x \vec{e}_x \\ E_y \vec{e}_y \\ E_z \vec{e}_z \end{pmatrix} \tag{3.20}$$

$$\vec{f}_{grad} = \varepsilon \begin{pmatrix} \frac{\partial E_x}{\partial x} E_x + \frac{\partial E_y}{\partial y} E_x + \frac{\partial E_z}{\partial z} E_x \\ \frac{\partial E_z}{\partial x} E_y + \frac{\partial E_y}{\partial y} E_y + \frac{\partial E_z}{\partial z} E_y \\ \frac{\partial E_x}{\partial x} E_z + \frac{\partial E_y}{\partial y} E_z + \frac{\partial E_z}{\partial z} E_z \end{pmatrix} \begin{pmatrix} \vec{e}_x \\ \vec{e}_y \\ \vec{e}_z \end{pmatrix} \tag{3.21}$$

where $\vec{e}_x$, $\vec{e}_y$ and $\vec{e}_z$ are the unit vectors in x, y, and z directions, respectively. Thus $\vec{f}_{grad}$ is from the first term of $\varepsilon\nabla\bullet(\vec{E}\vec{E}) = \varepsilon[(\nabla\bullet\vec{E})\vec{E} + (\vec{E}\bullet\nabla)\vec{E}]$, shown in Eq. (3.13), and the second term $\varepsilon(\vec{E}\bullet\nabla)\vec{E}$ is a part of the magnetic force. To obtain $\vec{f}_{grad}$, we also need to calculate the second term $\varepsilon(\vec{E}\bullet\nabla)\vec{E}$, which can be derived as follows:

$$\varepsilon\ (\vec{E}\bullet\nabla)\vec{E}=\varepsilon(E_x\frac{\partial}{\partial x}+E_y\frac{\partial}{\partial y}+E_z\frac{\partial}{\partial z})\begin{pmatrix}E_x\vec{e}_x\\E_y\vec{e}_y\\E_z\vec{e}_z\end{pmatrix} \tag{3.22}$$

then

$$(\vec{E}\bullet\nabla)\vec{E}=\begin{pmatrix}E_x\frac{\partial}{\partial x}E_x+E_y\frac{\partial}{\partial y}E_x+E_z\frac{\partial}{\partial z}E_x\\E_x\frac{\partial}{\partial x}E_y+E_y\frac{\partial}{\partial y}E_y+E_z\frac{\partial}{\partial z}E_y\\E_x\frac{\partial}{\partial x}E_z+E_y\frac{\partial}{\partial y}E_z+E_z\frac{\partial}{\partial z}E_z\end{pmatrix}\begin{pmatrix}\vec{e}_x\\\vec{e}_y\\\vec{e}_z\end{pmatrix} \tag{3.23}$$

When a mesoscopic or Mie metallic particle is in an external electric field, the electric field vanishes inside the metal particle, and the charge only distributes on the surface of the particle. Thus, for the slope (or differential) of electric field component from the surface to an arbitrary point on the surface of metal sphere, we obtain

$$\frac{\partial E_x}{\partial x}=\frac{E_x(x,y,z)-E_x(x-\triangle x,y,z)}{\triangle x}=\frac{E_x(x,y,z)-0}{\triangle x}=\frac{E_x(x,y,z)}{\triangle x} \tag{3.24}$$

In a similar way, we find

$$\frac{\partial E_a}{\partial b}=\frac{E_a(x,y,z)}{\triangle b} \tag{3.25}$$

where $a=x,y,z$, $b=x,y,z$. Note that these differential results are approximate and only valid for large metallic particles (mesoscopic or Mie metallic particles). For Rayleigh metallic nanoparticles smaller than the skin depth of the metal, Eq. (3.25) is invalid because the electric field does not vanish inside the particle.

Substituting Eq. (3.25) into the expressions for $(\nabla\bullet\vec{E})\vec{E}$ and $(\vec{E}\bullet\nabla)\vec{E}$, we then have

$$(\nabla\bullet\vec{E})\vec{E} = Real\begin{pmatrix} \frac{E_x E_x^*}{\triangle x} + \frac{E_y E_x^*}{\triangle y} + \frac{E_z E_x^*}{\triangle z} \\ \frac{E_x E_y^*}{\triangle x} + \frac{E_y E_y^*}{\triangle y} + \frac{E_z E_y^*}{\triangle z} \\ \frac{\partial E_x E_z^*}{\triangle x} + \frac{E_y E_z^*}{\triangle y} + \frac{E_z E_z^*}{\triangle z} \end{pmatrix}\begin{pmatrix} \vec{e}_x \\ \vec{e}_y \\ \vec{e}_z \end{pmatrix} \tag{3.26}$$

$$(\vec{E}\bullet\nabla)\vec{E} = Real\begin{pmatrix} \frac{E_x E_x^*}{\triangle x} + \frac{E_y E_x^*}{\triangle y} + \frac{E_z E_x^*}{\triangle z} \\ \frac{E_x E_y^*}{\triangle x} + \frac{E_y E_y^*}{\triangle y} + \frac{E_z E_y^*}{\triangle z} \\ \frac{\partial E_x E_z^*}{\triangle x} + \frac{E_y E_z^*}{\triangle y} + \frac{E_z E_z^*}{\triangle z} \end{pmatrix}\begin{pmatrix} \vec{e}_x \\ \vec{e}_y \\ \vec{e}_z \end{pmatrix} \tag{3.27}$$

As Eqs. (3.26) and (3.27) are equal, we conclude

$$(\nabla\bullet\vec{E})\vec{E} = (\vec{E}\bullet\nabla)\vec{E} = \frac{1}{2}\nabla\bullet(\vec{E}\vec{E}) \tag{3.28}$$

Hence, we find from Eqs. (3.22) and (3.28) the gradient force components of the Lorentz force to be:

$$\vec{f}_{grad} = \varepsilon(\nabla\bullet\vec{E})\vec{E} = \frac{\varepsilon}{2}\nabla\bullet(\vec{E}\vec{E}) \tag{3.29}$$

As $\vec{E}\vec{E}$ is a tensor, the gradient force can also be expressed in tensor form similar to the total force given in Eq. (3.18). The total electric field force (gradient force) becomes

$$\left\langle \vec{F}_{grad} \right\rangle = \left\langle \int_v \vec{f}_{grad}\bullet dv \right\rangle = \left\langle \int_s \vec{\vec{T}}_{grad}\bullet\vec{n}ds \right\rangle \tag{3.30}$$

where the tensor of gradient force:

$$\vec{\vec{T}}_{grad} = \frac{\varepsilon}{2}\vec{E}\vec{E} = \frac{\varepsilon}{2}\begin{pmatrix} E_x E_x & E_x E_y & E_x E_z \\ E_y E_x & E_y E_y & E_y E_z \\ E_z E_x & E_z E_y & E_z E_z \end{pmatrix} \tag{3.31}$$

Because the MST matrix $\vec{\vec{T}}$ consists of two components: $\vec{\vec{T}} = \vec{\vec{T}}_{grad} + \vec{\vec{T}}_{scat}$, the total

magnetic field force (scattering force)

$$\left\langle \vec{F}_{scat} \right\rangle = \left\langle \int_v \vec{f}_{scat} \bullet dv \right\rangle = \left\langle \int_s \vec{\vec{T}}_{scat} \bullet \vec{n} ds \right\rangle \tag{3.32}$$

where the tensor of the scattering gradient force is:

$$\begin{aligned} &\vec{\vec{T}}_{scat} = \vec{\vec{T}} - \vec{\vec{T}}_{grad} \\ &= \begin{bmatrix} \frac{1}{2}\varepsilon E_x E_x - \frac{\varepsilon}{2}E^2 + \frac{\mu}{2}(H_x H_x - \frac{H^2}{2}) & \frac{1}{2}\varepsilon E_x E_y - \frac{\varepsilon}{2}E^2 + \frac{\mu}{2}(H_x H_y - \frac{H^2}{2}) & \frac{1}{2}\varepsilon E_x E_z - \frac{\varepsilon}{2}E^2 + \frac{\mu}{2}(H_x H_z - \frac{H^2}{2}) \\ \frac{1}{2}\varepsilon E_y E_x - \frac{\varepsilon}{2}E^2 + \frac{\mu}{2}(H_y H_x - \frac{H^2}{2}) & \frac{1}{2}\varepsilon E_y E_y - \frac{\varepsilon}{2}E^2 + \frac{\mu}{2}(H_y H_y - \frac{H^2}{2}) & \frac{1}{2}\varepsilon E_y E_z - \frac{\varepsilon}{2}E^2 + \frac{\mu}{2}(H_y H_z - \frac{H^2}{2}) \\ \frac{1}{2}\varepsilon E_z E_x - \frac{\varepsilon}{2}E^2 + \frac{\mu}{2}(H_z H_x - \frac{H^2}{2}) & \frac{1}{2}\varepsilon E_z E_y - \frac{\varepsilon}{2}E^2 + \frac{\mu}{2}(H_z H_y - \frac{H^2}{2}) & \frac{1}{2}\varepsilon E_z E_z - \frac{\varepsilon}{2}E^2 + \frac{\mu}{2}(H_z H_z - \frac{H^2}{2}) \end{bmatrix} \end{aligned} \tag{3.33}$$

Finally, the gradient force and scattering force can be calculated by substituting $\vec{\vec{T}}_{grad}$ and $\vec{\vec{T}}_{scat}$. Thus, we can calculate the gradient and scattering forces by integrating the tensor $\vec{\vec{T}}_{grad}$ and $\vec{\vec{T}}_{scat}$.

All electric and magnetic field components in the x, y, and z directions are obtained from FDTD simulation data. In contrast to the well-known optical gradient force that basically depends on the gradient of the electric field intensity, the scattering force for a large metal particle is more complicated and determined by both electric and magnetic fields on the particle surface.

3.4 Trapping mechanisms for metallic particle

The force of particle at the center of SP-VP was firstly calculated. In the simulation, the incident wavelength (λ_0) is 1064 nm, the NA of the objective is 1.49, the refractive index of the glass substrate is 1.515, the thickness of the thin gold film is 45 nm, and the diameter of the gold particle is 1 μm. The actual vertical distance (*d*) between the bottom of the gold particle and the top of the metal film was unknown. *d*=50 nm was chosen in simulation in accord with the Debye length, which

is a typical length for electrostatic interactions commonly used in similar computations [105]. The focal field after a high NA lens is used as the input source in the simulation. The grid size is nonuniform ranging from 5 nm near material interfaces to 25 nm further from these boundaries. Note that the simulations in this chapter use these parameters and settings.

As can be seen from Fig. 3.4, most of the forces are downwards. This proves the SP-VP has the capability to trap the particle in proximity to the gold film. Since the particle is at the center of the SP-VP and the system is symmetrical around z direction, so the calculated forces are symmetrical. The majority of the forces are located at the bottom of the particle. The hot-spot locates between the gap of the particle and the film. The electric field intensity is highest there, where there is strong Coulomb interaction. This may explain the enhanced force.

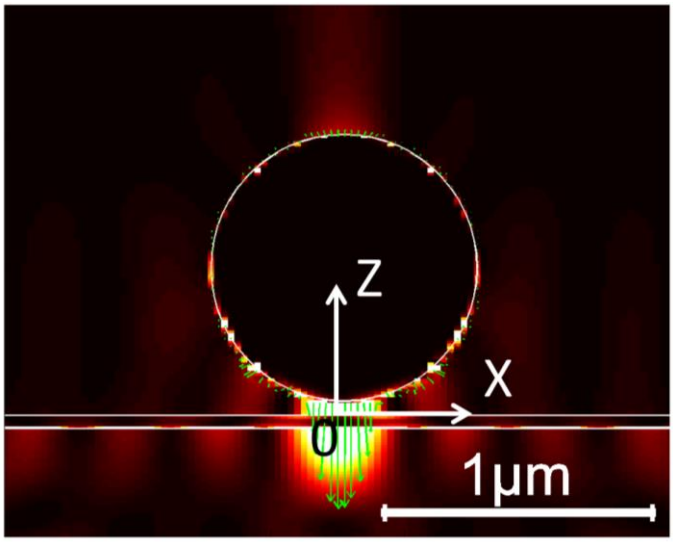

Fig. 3.4 The force of gold particle. The particle is at the center of SP-VP. Background is the distribution of electric field intensity. Green arrows indicate the forces around the particle.

Force distribution can be used for calculating trapping potential, which represents whether the particle can overcome the Brownian movement. Here, we only consider the two-dimensional trapping in the x-y plane on the metal surface.

Therefore, trapping or pushing only depends on horizontal forces F_x and F_y. Furthermore, owing to the cylindrical symmetry of incident light, only F_x needs to be considered in describing trapping if choosing y=0 for the position of the particle.

As we can see from Fig. 3.5, the force in x direction from 8 μm away to center is calculated. The negative value of F_x means the x direction force is along with the direction of the negative x axis. Particle in simulation is on the positive x axis. Particle at most positions in the range of under 5 μm experiences pulling force more than 25 fN. At the center of the SP-VP, the force is close to zero, which represents the balance state for particle. When the particle is about 0.6 μm offset, it experiences largest force. When the particle is far away, the force becomes weak. The gradient force and scattering force have the same trend. Both of them contribute to the total force.

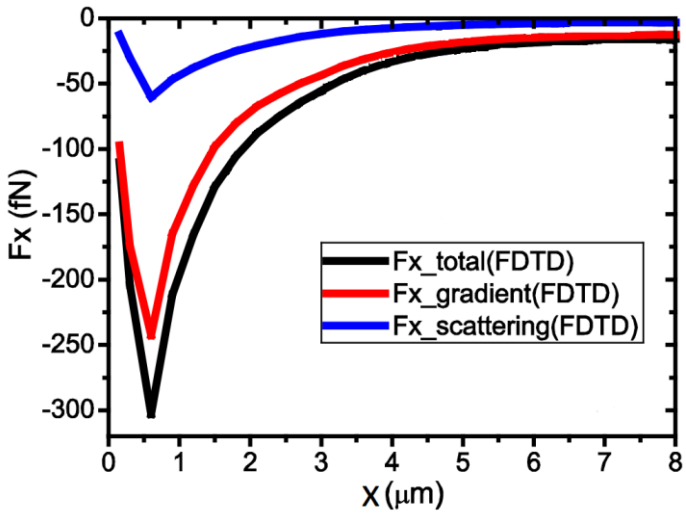

Fig. 3.5 Horizontal force (F_x) exerted on a metallic particle in focused plasmonic tweezers at different particle positions. Abscissa represents the position of the particle.

As shown in Fig. 3.6, the one-dimensional distribution of forces along the vertical direction (F_z) is also plotted. This is found to be different from the horizontal

forces (F_x). The former increase exponentially in magnitude all the way when close to the gold film, while the latter reach a maximum and then decrease in magnitude when close to the SP-VP center. The vertical direction force is responsible to balance the gravity and buoyancy on the metallic particle.

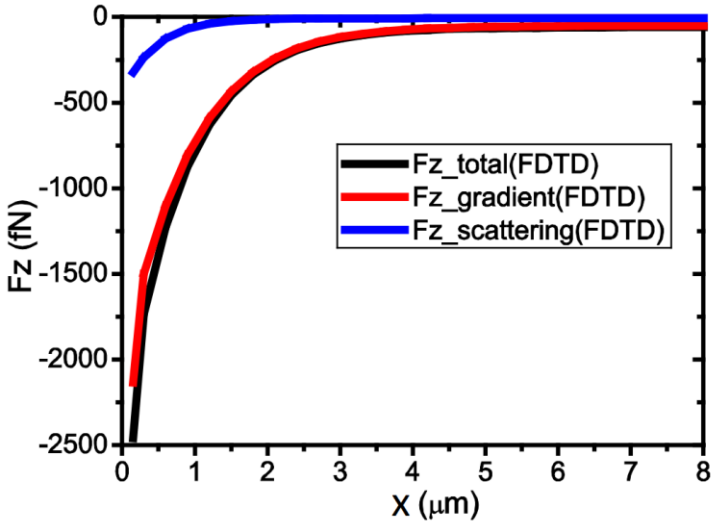

Fig. 3.6 Vertical force (F_z) exerted on a metallic particle in focused plasmonic tweezers at different particle positions. Abscissa represents the position of the particle.

3.5 Comparison of focused plasmonic tweezers and optical tweezers

3.5.1 Poynting vectors

Fig. 3.7 shows the distributions of electric field intensity and Poynting vectors in x-y plane of the virtual probe and the focused RPB systems without particles 100 nm above the metal/water and glass/water interfaces, respectively. These results can be obtained from simulations using software Rsoft v8.1. We can observe that the electric field intensity of central virtual probe is much stronger than the spot of focused RP beam due to the great enhancement of surface plasmon. However, we can also find that the magnitudes of Poynting vectors in Fig. 3.7(a) are

approximately zero compared to those in Fig. 3.7(b), indicating that the maximum Poynting vector in the field of virtual probe is much more smaller than that of the focused RP laser beam, due to the fact that the virtual probe is a standing wave pattern of surface plasmon without great power flux. These differences provide clues to understanding the pull instead of push exerted by the plasmonic tweezers. Such result suggests that the radiation pressure corresponding to power flux of the virtual probe is very small, and therefore it is easy to be overcome by a pulling force. In contrast, the Poynting vectors of the focused RP laser beam are much greater from center to outward, revealing that the radiation pressure is strong and could push the particles away from the center.

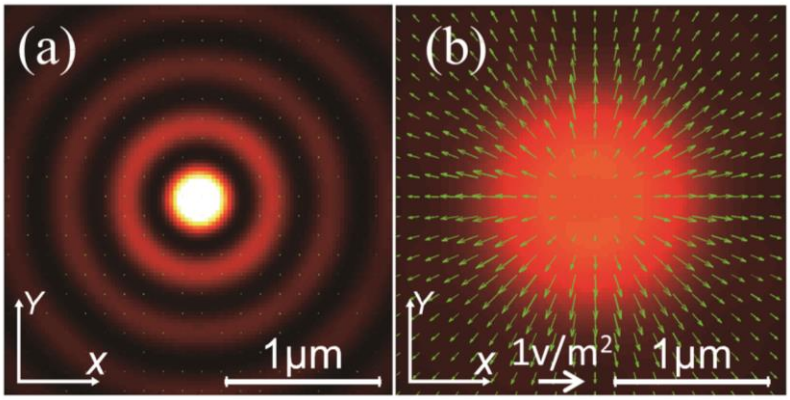

Fig. 3.7 The comparison of electrical fields (a) above metal/water interface in focused plasmonic tweezers and (b) above glass/water interface in optical tweezers. The background is the electric field intensity. Green dots in (a) indicate the Poynting vectors are closed to zero. Green arrows in (b) indicate the Poynting vectors.

3.5.2 Total forces

To obtain further insight into the trapping and pushing of gold particles, the electric field distributed around the particle was calculated in a 3D FDTD simulation, and further applied Eq. (3.19) to obtain the total electromagnetic force exerted on the particle, for both types of tweezers, i.e. focused plasmonic tweezers and optical tweezers.

Fig. 3.8 presents intensity distributions of the electric field and the total force (including gradient force and scattering force) exerted on a particle in x-z plane of the virtual probe and the focused RPB systems, respectively. The arrows represent the forces exerted on each segment of the particle surface orientated from the center of particle. In Fig. 3.8(a), the high-intensity region at the left lower corner of the particle shows a strong coupling between the virtual probe and the metallic particle. Lengths of the arrows located in this region also indicate that such coupling produces strong forces in x- and z- directions, and therefore pulls the particle towards the center. The arrows in Fig. 3.8(b) depict that the particle suffers horizontal pushing forces at most segments of particle surface, resulting in a high radiation pressure to push the particle away from the beam. Note that the results in Figs. 3.8(a) and (b) are not directly comparable. They only show typical results of focused plasmonic tweezers and optical tweezers. The theoretical results in Fig. 3.8 demonstrate that the force on metallic particle in horizontal direction is pulling/pushing corresponding to the presence/absence of the metal film and excitation of surface plasmon.

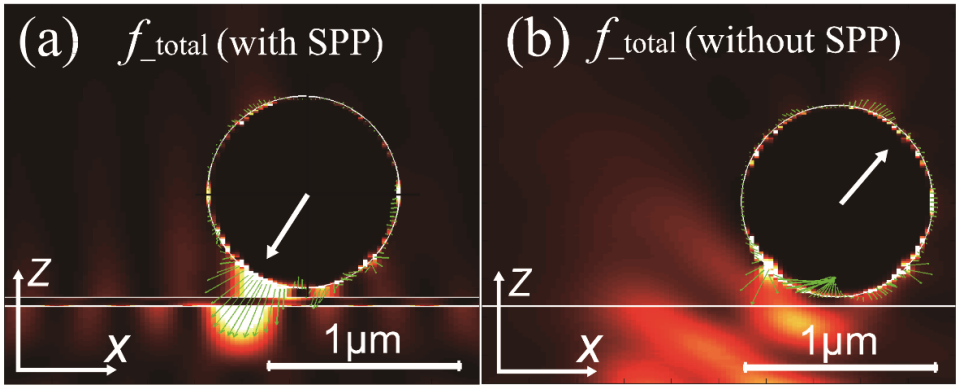

Fig. 3.8 The comparison of total forces in focused plasmonic tweezers (a) and optical tweezers (b). The white arrows starting from the centers of the spheres denote the resultant forces on the particles. The background is the electric field intensity, while the white lines indicate the spherical particle and gold film. The gold particle is in the vertical x-z plane for both tweezers. The particle in (a) is 50 nm above the gold surface and 300 nm away from the surface plasmon peak at the horizontal center. In (b), there is no metal film and the particle is 600 nm away from the horizontal center.

3.5.3 Gradient/scattering forces

To understand the different mechanisms underlying the two types of tweezers, we need to further separate the total electromagnetic force into gradient and scattering forces with calculations by Eqs. (3.30-3.33). As shown in Fig. 3.9, both gradient forces tend to attract particles towards the center. Plasmonic tweezers produced a relatively stronger force. The scattering force for the optical tweezers opposes the gradient force, whereas the scattering force for the plasmonic tweezers in contrast augments the gradient force in the horizontal direction.

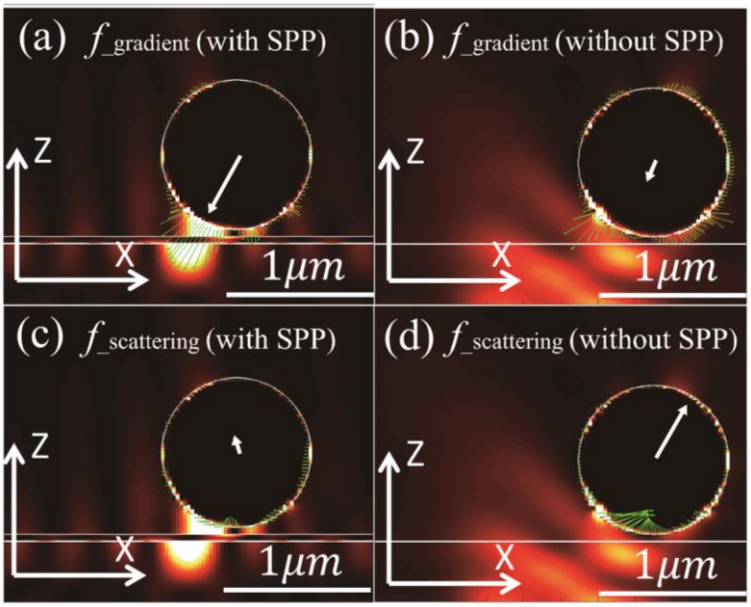

Fig. 3.9 The comparison of gradient forces and scattering forces in focused plasmonic tweezers and optical tweezers.

3.5.4 Electric field line distributions

As shown in Fig. 3.10, the electric field line distributions were also calculated using the same indicators and parameters in Fig. 3.8. The electric field lines always flows from positive charges to negative charges. There is no charge in the metal and metallic particle. The charges exist on the surfaces of the metal and metallic particles. The more the charges the Coulomb interaction will be more

significant. The electric field line distributions agree well with the total force distributions.

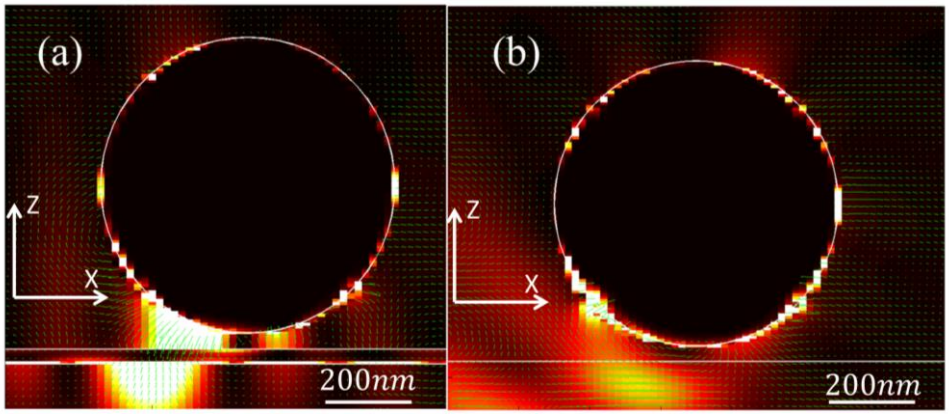

Fig. 3.10 The comparison of electric field lines (indicated by green arrows) in (a) focused plasmonic tweezers and (b) optical tweezers. The indicators and parameters are same as in Fig. 3.8.

3.6 Discussion

For metallic particles, the attractive gradient force is essentially the Coulomb force related to the local electric field [Eq. (3.5)]. The pushing scattering force is essentially the Laplace force related to the local magnetic field [Eq. (3.6)]. The gradient force can be enhanced by a stronger and sharper electric field. The gradient force always points to the peak of the field, whereas the scattering force is determined by the light propagation as well as the power flux. In focused plasmonic tweezers, the successful trapping of metallic particles is, as stated earlier, due to a surface plasmon enhanced gradient force accompanied with a scattering force in the horizontal direction [Fig. 3.6(a) and 3.7(a)]. The key to the unusual contribution of the force is the highly focused field of SP-VP, whose FWHM of focus is sized in deep sub-wavelength (~0.245 λ_0) because the plasmonic wave is an evanescent wave beyond the diffraction limit.

Compared with the diffraction-limited focusing of a Gaussian beam in optical tweezers, the sharper focusing of the plasmonic wave produces stronger gradient

forces. Furthermore, the scattering force in focused plasmonic tweezers system aligns with the gradient force, and then helps trapping. Thus, even if a Gaussian beam can be focused up to the size of the virtual probe, it is still very hard to trap the mesoscopic/Mie size metal particle, because as the focus size decreases, the repulsive scattering force of the Gaussian beam strengthens more rapidly than the gradient force at the focus region, and then disrupts the trapping.

In plasmonic tweezers, the generation process of the virtual probe is similar to that described in [111, 112]. First the SPPs are excited by a focused RPB at a typical SPR angle, then act as secondary circular sources on the metal film propagating inward to the center, and finally form sharp and strong plasmonic virtual probes after constructive interference. In this process, the scattering force derives from the pushing as excited SPPs propagate inward toward the central peak. The direction of push is hence in the same direction as the attractive gradient force. The scattering force is weaker than the gradient force, because after interference the final focused surface plasmon field approximates a standing wave pattern and then produces a low power flux [as evidenced by the Poynting vectors in Fig. 3.4(a)]. The dominant gradient force originates from the greatly enhanced coupling between the SP-VP and the metallic particle [as seen in Fig. 3.6(a) by the high field intensity at the lower left surface of the particle].

When the particle approaches the SP-VP center, the gradient force first reaches a maximum due to the increasing field intensity, and then decreases in magnitude at the center as a result of force equilibrium in the horizontal direction (Fig. 3.9), which forms a potential well to confine the particle. The dominant role of the gradient force is also reflected by the charge distribution in Fig. 3.10, because the vertical force correlates strongly with coupling strength.

In contrast, for the optical tweezers without metal film, the optical focus is not as sharp as the SP-VP. The coupling between optical focus and metallic particle is weak [Fig. 3.4(b)] while the power flux from center to outer is strong [Fig. 3.4(b)]. Thus, with the scattering force being greater than the gradient force, metallic particles are pushed away from the focus. For similar reasons, in the unfocused surface plasmon field, the metallic particles are also pushed away by the stronger scattering force [105].

Besides optical gradient and scattering forces, it was reported that the heating effects, including thermophoresis and convection, play a complicated role in plasmonic tweezers systems [23, 122-126]. Thermophoresis can generate forces either in the direction of heat gradient or in the opposite direction [123], while the convection could help trapping by circulating fluid around to draw particles to the hot region [124]. In plasmonic tweezers system, because only a very small amount of incident light could couple to surface plasmon and contribute to the heating effect, the temperature increase in the plasmonic tweezers system is maintained in the order of several Kelvins [127]. This temperature increase creates a convection force by circulating fluid to further strengthen the trapping force along the horizontal dimension.

3.7 Summary

In conclusion, this research revealed an unusual feature enabling stable trapping of metallic particles above metal film, especially in the mesoscopic/Mie size range. In contrast to the strong scattering force leading to push on metallic particles in optical tweezers, the surface plasmon enhanced gradient force dominates in focused plasmonic tweezers. Augmented by a like-directed scattering force, metallic

particles are therefore attracted towards the central peak of the highly focused surface plasmon field. The key to the successful trapping of particles in plasmonic tweezers is the highly focused surface plasmon field. Thus, focused plasmonic tweezers could be employed for trapping and manipulating various metallic objects from nanometer to micrometer scales. Moreover, because of the enhancement from coupling between SPPs and LSPs of the metallic particles, the plasmonic tweezers have great potential in SERS and other applications. It is believed that this work not only provides an alternative way of trapping and manipulating metallic particles, it also delivers an important contribution towards a comprehensive understanding and optimization of trapping forces produced by surface plasmon enhanced evanescent fields.

Chapter 4 Plasmonic trapping and tuning of a horizontally-oriented metallic particle dimer

4.1 Introduction

Gold nanoparticle dimers have attracted much attention in plasmonic sensing, because strong electric field, also known as hot spots, can be excited in the nanoscale gap between the two gold nanoparticles [128-131]. This makes them useful for the electric field enhancement in plasmonic sensing and measurement applications including SERS [74, 132]. Compared to other nanostructures for hot-spot excitation, such as nano-antenna [133] and metallic nano-tips [134], gold nanoparticle dimers offer great flexibility and can be used for intracellular detections. In SERS, the nanoscale gap or void formed by gold nanostructures is important for the electric field enhancement [132]. As we have known, the electric field enhancement factor is inversely-proportional to the size of the gap [135, 136]. Therefore, we aim to find an alternative way to obtain a controllable nanoparticle gap for LSPR excitation.

On the basis of optical tweezers, optical tweezer array is capable of trapping and moving multiple particles [63]. However, it is very challenging to manipulate metallic particles using optical tweezers due to the high scattering in the interaction between metallic particles and the focused laser beam. Although beam shaping method was used to trap metallic Rayleigh particles, i.e. particles with radius less than the incident wavelength [91, 94, 137], the tuning of the nanoscale gap is very difficult, as is constrained by the diffraction limit of the light.

Recently, plasmonic tweezers was used to manipulate metallic particles ranging in size from tens of nanometers to hundreds of micrometers [22, 104, 105, 107-110, 138-140]. In these studies, the trapping force was enhanced to move gold

particles, based on the coupling of SPPs and LSPs. In Chapter 3, focused plasmonic trapping of metallic particles was demonstrated by using a virtual probe on a smooth gold film [24]. It was showed that the enhanced surface plasmon field was able to trap metallic particle as a result of the rapidly varying electric field.

In this chapter, the first study on plasmonic trapping and tuning of a gold nanoparticle dimer is presented [33]. A linearly polarized beam is focused onto a silver film to excite SPPs. Note that both silver film used in this chapter and gold film used in previous chapter and are applicable for surface plasmon excitation. The interference between the excited SPWs forms two symmetrical virtual probes, which are used to trap two nanoparticles. To interpret the trapping process, Richards-Wolf vectorial diffraction theory and angular spectrum representation are used to calculate the plasmonic field. A relation between the virtual probes spacing and the excitation wavelength is obtained. Subsequently, 3D FDTD simulations are carried out to analyse the electric field interacting with the gold nanoparticles. The forces are calculated using MST method. Both gold nanospheres and nanorods are used in simulations to test the plamonic tweezers system.

4.2 Surface plasmon virtual probe pair

4.2.1 Surface plasmon virtual probe pair excitation configuration

The proposed plasmonic tweezers system is shown in Fig. 4.1. The plasmonic field is excited on the Ag film by a focused linearly polarized beam, and a virtual probe pair is formed for gold nanoparticles trapping. Since the surface plasmon excitation is polarization selective (p-polarization), it has the maximum efficiency along the polarization direction (x direction).

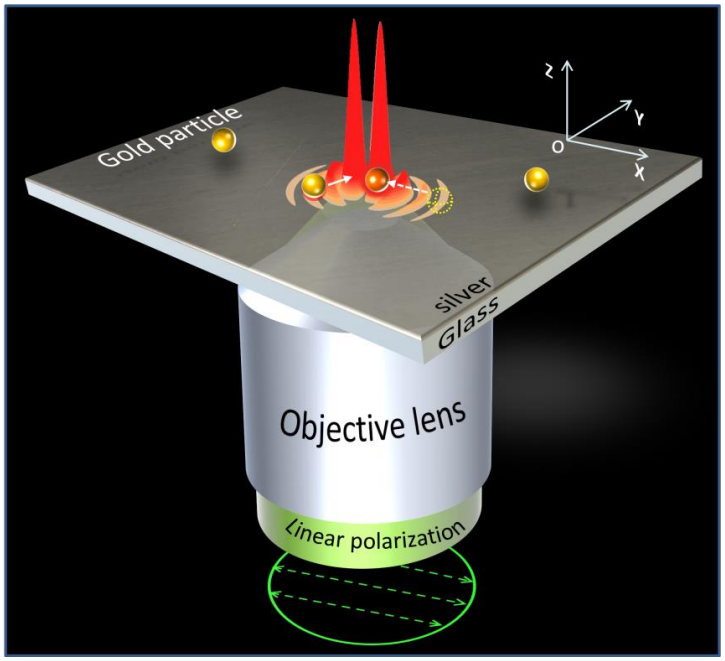

Fig. 4.1 The proposed plasmonic tweezers system. The incident light is linearly-polarized and is focused to a 45 nm-thick silver film through a 1.49-NA objective lens. Green-colored arrows indicate the polarization direction of the incident light (x direction). Red-colored field is the calculated surface plasmonic field, excited by the focused linearly-polarized beam.

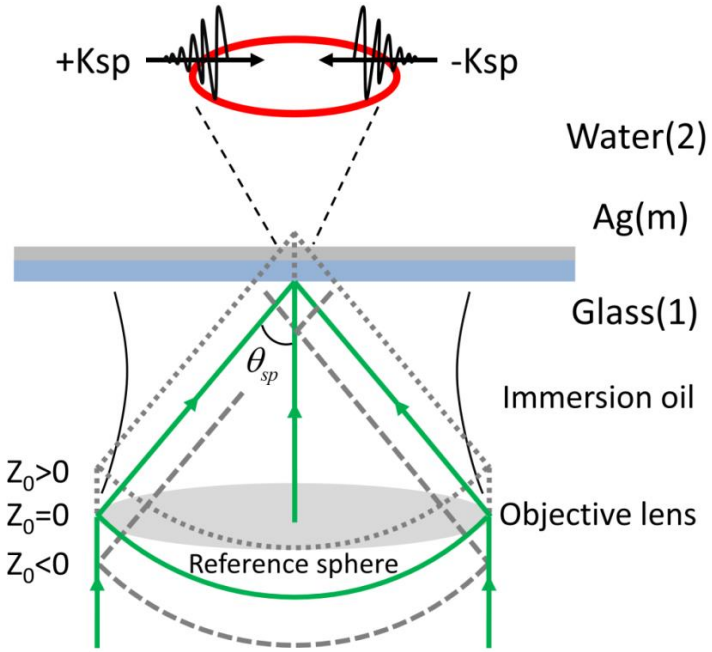

Fig. 4.2 Front view of the system in x-z plane, showing the plasmonic virtual probe pair generated by interference. 2, m and 1 indicate different substrates, and are used as subscripts in following derivations and equations. The solid green lines indicate the incident light at an angle close to θ_{sp}.

A simplified structure (x-z plane) of the system is shown in Fig. 4.2. Z_0 represents the distance from the laser focus to the metal film. If $Z_0>0$, two sets of symmetrical plane waves are incident at angles $\pm\theta_{sp}$ and excite a pair of counter-propagating SPWs with wave vectors $\pm k_{sp}$. The π phase delay between these two SPWs causes a destructive interference and two enhanced lobes in the standing wave are formed. Evidence of such counter-propagating waves was presented experimentally in [141, 142] .

4.2.2 Theoretical calculation of the surface plasmon virtual probe pair

The angular spectrum representation of an optical field can be expressed as [143]

$$\mathbf{E}(x,y,z)=\iint_{-\infty}^{\infty}\hat{E}(k_x,k_y;0)e^{i[k_x x+k_y y\pm k_z z]}dk_x dk_y \tag{4.1}$$

The Fourier spectrum $\hat{\mathbf{E}}$ can be expressed in terms of the far-field as [143]:

$$\hat{\mathbf{E}}(k_x,k_y;0)=\frac{ire^{-ikr}}{2\pi k_z}\mathbf{E}_\infty(k_x,k_y) \tag{4.2}$$

where $r=(x^2+y^2+z^2)^{1/2}$ is the distance between $\mathbf{r}_\infty$ and the origin. k is the wavevector. $\mathbf{r}_\infty$ is on the object plane. Substitute Eq. (4.2) to Eq. (4.1), we can obtain

$$\mathbf{E}(x,y,z)=\frac{ire^{-ikr}}{2\pi}\iint_{(k_x^2+k_y^2)\le k^2}\mathbf{E}_\infty(k_x,k_y)e^{i[k_x x+k_y y+k_z z]}\frac{1}{k_z}dk_x dk_y \tag{4.3}$$

The focal fields can be calculated according to the boundary condition of the focusing system and the incident light. Following the theory proposed by Richards and Wolf [144], the fields close to a lens can be presented by the rules of geometrical optics.

The unit vectors $\mathbf{n}_\rho$, $\mathbf{n}_\phi$ and $\mathbf{n}_\theta$ are introduced to describe light refraction at the reference sphere, as shown in Fig. 4.3. Refraction can be easily understood with decomposing the incident vector $\mathbf{E}_{inc}$ into two components indicated by $\mathbf{E}_{inc}^{(s)}$ and $\mathbf{E}_{inc}^{(p)}$. The superscripts (s) and (p) indicate s- and p- polarizations, respectively. The two unit vector fields can be expressed as

$$\mathbf{E}_{inc}^{(s)} = [\mathbf{E}_{inc} \cdot \mathbf{n}_\phi]\mathbf{n}_\phi, \mathbf{E}_{\mathbf{inc}}^{(p)} = [\mathbf{E}_{inc} \cdot \mathbf{n}_\rho]\mathbf{n}_\rho \tag{4.4}$$

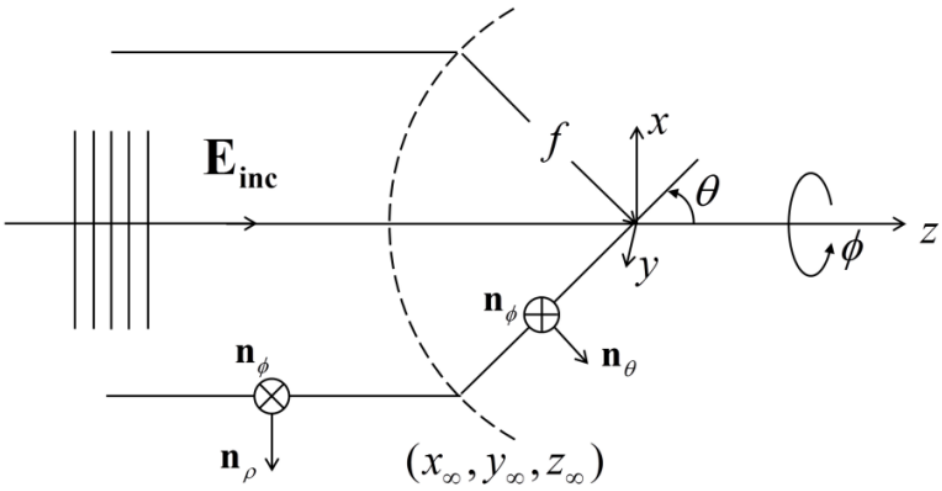

Fig. 4.3 Representation of plane wave focusing by Geometrical Optics.

As we can see in Fig. 4.3, the two fields refract at the spherical surface in a different way. The unit vector $\mathbf{n}_\phi$ remains unchanged and the unit vector $\mathbf{n}_\rho$ is mapped into $\mathbf{n}_\theta$ .Therefore, the total electric field $\mathbf{E}_\infty$ after refraction can be expressed as

$$\mathbf{E}_\infty = [t^s[\mathbf{E}_{inc} \cdot \mathbf{n}_\phi]\mathbf{n}_\phi + t^p[\mathbf{E}_{inc} \cdot \mathbf{n}_\rho]\mathbf{n}_\theta]\sqrt{\frac{n_1}{n_2}}(\cos\theta)^{1/2} \tag{4.5}$$

where t^s and t^p are the transmission coefficients for s- and p- polarizations, respectively. The factor outside the bracket is to ensure energy conservation according to the intensity law. The subscript ∞ was added to indicate the field evaluated is far away from the focal point (x, y, z) = (0, 0, 0).

The unit vectors $\mathbf{n}_\rho$, $\mathbf{n}_\phi$ and $\mathbf{n}_\theta$ can be expressed by Cartesian unit vectors $\mathbf{n}_x$, $\mathbf{n}_y$, $\mathbf{n}_z$ and spherical coordinates θ and φ, which are defined in Fig. 4.4.

$$\mathbf{n}_\rho = \cos\phi\mathbf{n}_x + \sin\phi\mathbf{n}_y \tag{4.6}$$

$$\mathbf{n}_\phi = -\sin\phi\mathbf{n}_x + \cos\phi\mathbf{n}_y \tag{4.7}$$

$$\mathbf{n}_\theta = \cos\theta\cos\phi\mathbf{n}_x + \cos\theta\sin\phi\mathbf{n}_y - \sin\theta\mathbf{n}_z \tag{4.8}$$

Substitute these three vectors to Eq. (4.5), we can obtain

$$\begin{aligned}\mathbf{E}_\infty(\theta,\phi) = t^s(\theta)\left[\mathbf{E}_{\mathbf{inc}}(\theta,\phi)\cdot\begin{pmatrix}-\sin\phi\\ \cos\phi\\ 0\end{pmatrix}\right]\begin{pmatrix}-\sin\phi\\ \cos\phi\\ 0\end{pmatrix}\sqrt{\frac{n_1}{n_2}}(\cos\theta)^{1/2}\\ +t^p(\theta)\left[\mathbf{E}_{\mathbf{inc}}(\theta,\phi)\cdot\begin{pmatrix}\cos\phi\\ \sin\phi\\ 0\end{pmatrix}\right]\begin{pmatrix}\cos\phi\cos\theta\\ \sin\phi\cos\theta\\ -\sin\theta\end{pmatrix}\sqrt{\frac{n_1}{n_2}}(\cos\theta)^{1/2}\end{aligned} \tag{4.9}$$

which is the field in Cartesian vector components after being focused to the right side of the reference sphere. $\mathbf{E}_\infty$ can be expressed in terms of the spatial frequencies k_x and k_y by employing the following substitutions:

$$k_x = k\sin\theta\cos\phi, k_y = k\sin\theta\sin\phi, k_z = k\cos\theta \tag{4.10}$$

Since the system is symmetrical, the angular spectrum representation Eq. (4.3) can be conveniently expressed in terms of the angles θ and φ instead of k_x and k_y. This is readily achieved with the substitutions in Eq. (4.10) and the transverse coorfinates (x, y) of the focal point shown as follows:

$$x = \rho\cos\varphi, y = \rho\sin\varphi \tag{4.11}$$

In order to represent the double integration over k_x, k_y by a spherical integration over θ and φ, we can use the transforming of the differentials as

$$\frac{1}{k_z}dk_x dk_y = k\sin\theta dx\theta d\phi \tag{4.12}$$

which has been illustrated in Fig. 4.4. The angular spectrum representation of the focal field [Eq. (4.3)] can be expressed as

$$\mathbf{E}(\rho,\varphi,z)=\frac{ikfe^{-ikf}}{2\pi}\int_0^{\theta_{\max}}\int_0^{2\pi}\mathbf{E}_\infty(\theta,\phi)e^{ikz\cos\theta}e^{ik\rho\sin\theta\cos(\phi-\varphi)}\sin\theta d\phi d\theta \tag{4.13}$$

where $NA=n\sin\theta_{\max}(0<\theta_{\max}<\pi/2)$.

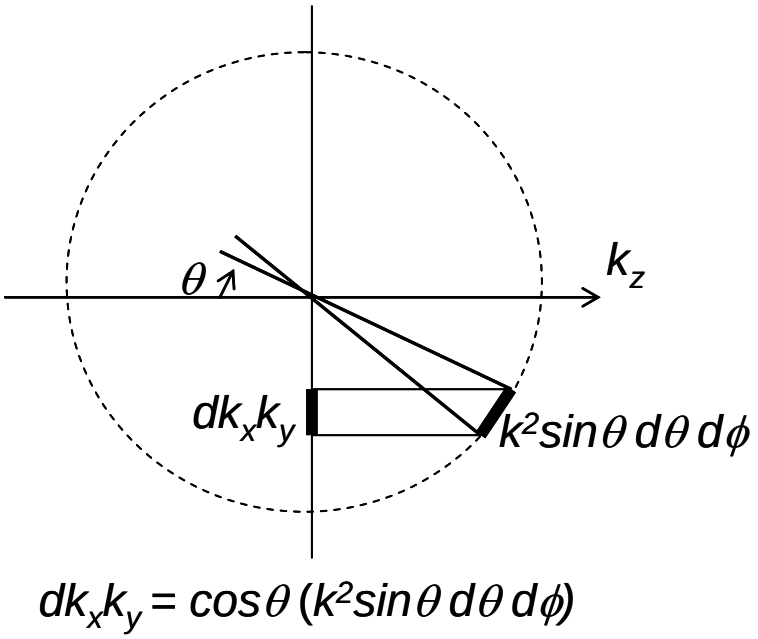

Fig. 4.4 Illustration of the wavevector substitution

According to Fresnel functions, for Kretschmann configuration (three-layer structure: substrate-Ag-water), the transmission coefficients for E_r , E_φ and E_z transmitting through a metal film are given as [46]:

$$\begin{cases} T_r^p(\theta)=\dfrac{E_{2r}^{\ p}}{E_{1r}^{\ p}}=\dfrac{\varepsilon_1 k_{z2}}{\varepsilon_2 k_{z1}}\cdot\dfrac{(1+r_{m2}^p)(1+r_{1m}^p)\exp(ik_{zm}d)}{1+r_{m2}^p r_{1m}^p\exp(2ik_{zm}d)} \\ T_\varphi^s(\theta)=\dfrac{E_{2\varphi}^{\ s}}{E_{1\varphi}^{\ s}}=\dfrac{(1+r_{m2}^s)(1+r_{1m}^s)\exp(ik_{zm}d)}{1+r_{m2}^s r_{1m}^s\exp(2ik_{zm}d)} \\ T_z^p(\theta)=\dfrac{E_{2z}^{\ p}}{E_{1z}^{\ p}}=\dfrac{\varepsilon_1}{\varepsilon_2}\cdot\dfrac{(1+r_{m2}^p)(1+r_{1m}^p)\exp(ik_{zm}d)}{1+r_{m2}^p r_{1m}^p\exp(2ik_{zm}d)} \end{cases} \tag{4.14}$$

where $k_{zi}=k_0\sqrt{\varepsilon_i-\varepsilon_1\cdot\sin^2\theta}$ is the longitudinal wave vector, ε_1 is the dielectric constant of the substrate, d is the thickness of the metal film, r_{ij}^s and r_{ij}^p are the

Fresnel reflection coefficients for s- and p- polarizations at the *i* (incident) and *j* interfaces respectively.

Fig. 4.5 shows that the transmission coefficients as a function of the light incident angles for different electric fields at both s- and p- polarizations. The dielectric constant of Ag in the calculation is obtained according to Johnson and Christy [145]. It can be seen that T_φ is relatively small over the entire angle range. This suggests that E_φ is significantly attenuated by the Ag film. Compared to T_φ, both T_r and T_z are relatively large with the values of 7.6 and 8.9 at $\theta_{sp} = 72.3^\circ$. The maximum incident angle can be achieved by 1.49-NA objective lens is 79.6°, which is sufficient for surface plasmon excitation.

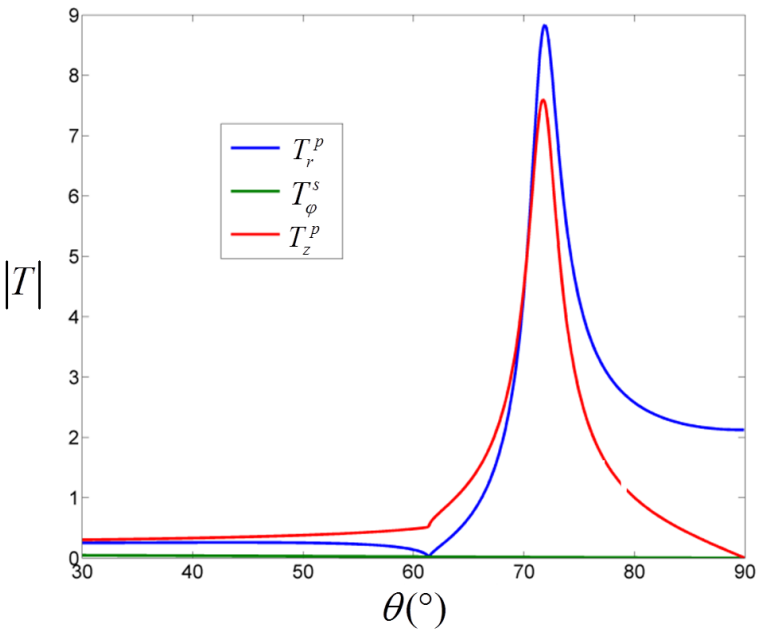

Fig. 4.5 Calculated transmission coefficients as a function of incident angles for s- and p-polarization for different electric field components. $\varepsilon_2 = 1.33$, $\varepsilon_1 = 1.515^2$, the thickness of sliver film $d = 45\,nm$, the dielectric constant of Ag film is -11.76+0.37i at 532 nm, and the water layer thickness is 3 μm.

For a strongly focused system shown in Fig. 4.1, the angular spectrum representation can show how the field propagates and how it is mapped onto other planes [143]:

$$E_t(x,y,z)=\int_{k_x}\int_{k_y}E\left(k_x,k_y\right)\exp\left[i\left(k_x x+k_y y\pm k_z z\right)\right]dk_x dk_y \tag{4.15}$$

where k_x, k_y and k_z are the transverse and longitudinal components of the wave vector, respectively, and $E\left(k_x,k_y\right)$ is the incident electromagnetic field. Considering asymptotic far-zone approximation of this field, Eq. (4.15) becomes

$$E_t(x,y,z)=\frac{ife^{-ik_1 f}}{2\pi}\iint_{k_x,k_y}E_t^{\infty}(k_x,k_y)\frac{1}{k_{z2}}e^{i\left(k_x x+k_y y+k_z z\right)}dk_x dk_y \tag{4.16}$$

Invoking the boundary conditions at $Z=Z_0$ in Eq. (4.16), and using Fresnel coefficients, we obtain

$$E_t^{\infty}=E_{inc}(k_x,k_y)e^{i(k_{z1}-k_{z2})z_0}\begin{bmatrix}t^s{k_y}^2+t^p{k_x}^2k_{z2}/k_2\\-t^s k_x k_y+t^p k_x k_y k_{z2}/k_2\\0-t^p({k_x}^2+{k_y}^2)k_x/k_2\end{bmatrix}\frac{k_{z2}}{k_{z1}}\frac{\sqrt{k_{z1}/k_1}}{{k_x}^2+{k_y}^2} \tag{4.17}$$

where t^s and t^p are the transmission coefficients of the s- and p- polarization light, respectively. We are interested in the longitudinal component in Eq. (4.17):

$$E_z^{\infty}=-E_{inc}(k_x,k_y)e^{i(k_{z1}-k_{z2})z_0}t^p\frac{k_x}{k_2}\frac{k_{z2}}{k_{z1}}\sqrt{k_{z1}/k_1} \tag{4.18}$$

Following the theory established by Richards and Wolf [144, 146], cylindrical coordinates are used in the following analysis,:

$$E_t(\rho,\varphi,z)=\frac{ife^{-ik_1 f}}{2\pi}\int_0^{\theta_{\max}}\int_0^{2\pi}-E_{inc}(\theta,\phi)e^{i(k_{z1}-k_{z2})z_0}t^p e^{ik_2\rho\sin\theta\cos(\phi-\varphi)}e^{izk_{z2}}\frac{{k_2}^2}{k_1}\sin^2\theta\sqrt{\cos\theta}\cos\phi\,d\theta d\varphi \tag{4.19}$$

By using the mathematical identity:

$$\int_0^{2\pi}\cos\phi\exp[ik_2\rho\sin\theta\cos(\phi-\varphi)]=2\pi i\cos\varphi J_1(k_2\rho\sin\theta) \tag{4.20}$$

where $J_1(x)$ is the first order Bessel function of the first kind, we have

$$E_t(\rho,\varphi,z)=\cos\varphi\, f e^{-ik_1 f}\int_0^{\theta_{\max}} E_{inc}(\theta,\phi)e^{i(k_{z1}-k_{z2})z_0}t^p J_1(k_2\rho\sin\theta)e^{ik_{z2}z}\frac{{k_2}^2}{k_1}\sin^2\theta\sqrt{\cos\theta}\,d\theta d\varphi \tag{4.21}$$

Assuming the incident light as a linearly polarized Gaussian beam, we can obtain

$$E_{inc}(\theta,\phi)=E_0 e^{-f^2\sin^2\theta/\omega_0^2}=E_0 e^{-\sin^2\theta/f_0^2\sin^2\theta_{\max}}=E_0 e^{-\frac{{n_1}^2\sin^2\theta}{(f_0 NA)^2}} \tag{4.22}$$

where $f_0=\dfrac{w_0}{f\sin\theta_{\max}}$ is the filling factor and the identifier [34], and n_1 is the refractive index of the substrate. The plasmonic electric field in Eq. (4.21) becomes

$$E_t(\rho,\varphi,z)=\cos\varphi\, f e^{-ik_1 f}\int_0^{\theta_{\max}} E_0 e^{-\frac{{n_1}^2\sin^2\theta}{(f_0 NA)^2}}e^{i(k_{z1}-k_{z2})z_0}t^p J_1(k_2\rho\sin\theta)e^{ik_{z2}z}\frac{{k_2}^2}{k_1}\sin^2\theta\sqrt{\cos\theta}\,d\theta \tag{4.23}$$

where ρ is the distance from the excitation point, φ is the angle with respect to the polarization direction and z is the distance to the metal film, k_1 and k_2 are the propagating wave vectors in the substrate and in the sample respectively, subscript z indicates the longitudinal component, and t^p is the transmission coefficient defined in Eq. (4.14).

Given Z_0=1 μm and Z_0=2 μm, the plasmonic fields were calculated using Eq. (4.23), as shown in Fig. 4.6. The fringe period of the plasmonic field is approximately 185 nm, which is in close agreement with the half surface plasmon wavelength [147]. The electric distribution patterns are similar, but the electric field values differ. When Z_0 is larger, the focused beam has better angle for surface plasmon excitation. The initiated SPPs will have stronger fields. The electric field of the standing wave after the interference will be stronger.

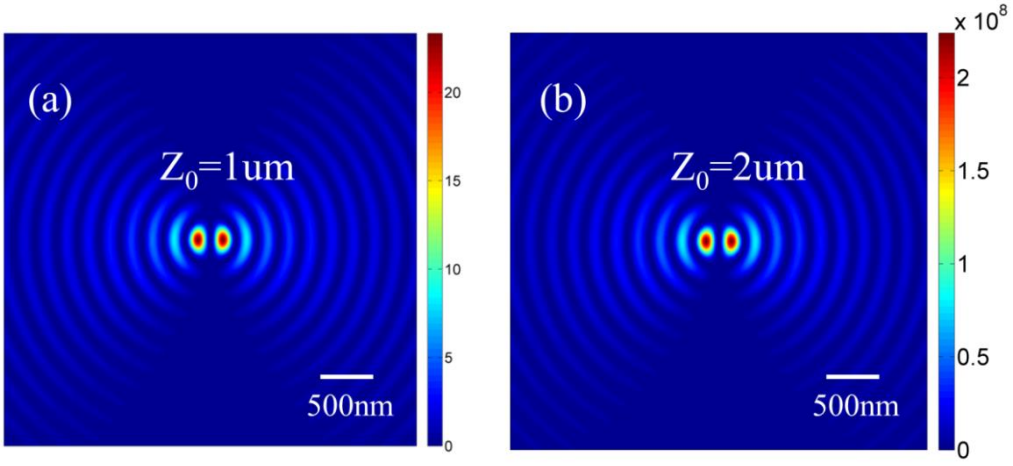

Fig. 4.6 Top-view of the plasmonic field (showing the electrical-field distribution 10 nm above the silver layer. $f_0 = 1$ [f_0 is the filling factor and the identifier defined in Eq. (4.22)]. Z_0=1 μm for (a) and Z_0=2 μm for (b).

When Z_0=0 μm, as shown in Fig. 4.7, there will be interference in a small central area, two maximum field peaks are generated, but there is no obvious interference fringes.

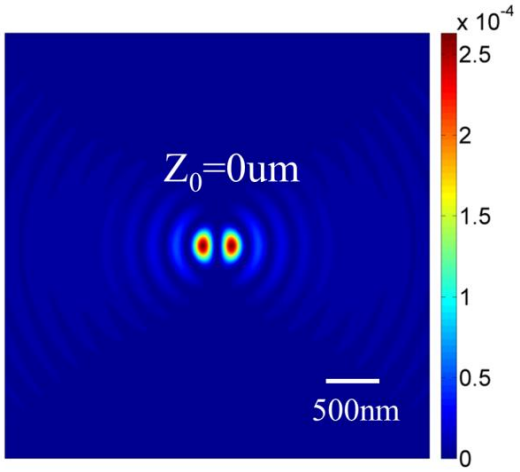

Fig. 4.7 Top-view of the plasmonic field (showing the electrical-field distribution 10 nm above the silver layer. Z_0=0 μm and $f_0 = 1$.

The situation when Z_0 below zero was also calculated. The excited two SPWs will not have interference and they propagate outwards the center in the opposite directions. Along with the focus spot away from the surface, the gap of the initiated excitation spots will be increased, which can be clearly seen in Fig. 4.8 (c) and (d).

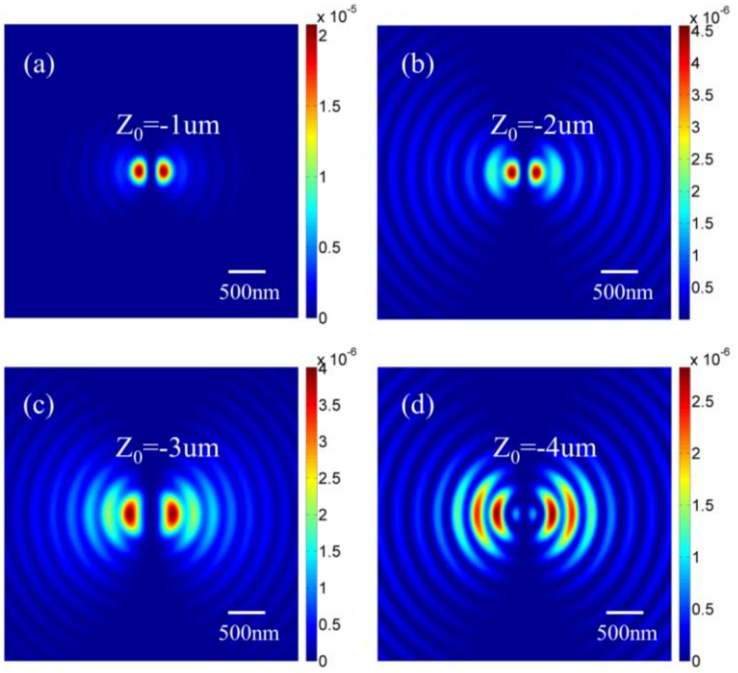

Fig. 4.8 Top-view of the plasmonic field (showing the electrical-field distribution 10 nm above the silver layer. $f_0 = 1$. Z_0=-1 μm for (a), Z_0=-2 μm for (b), Z_0=-3 μm for (c) and Z_0=-4 μm for (d).

Based on the discussions above, Z_0>0 scheme is chosen, and two hot-spots in a standing wave are generated for plasmonic trapping purpose. Z_0=1 is used in the following calculations.

4.3 Trapping mechanisms for metallic particle dimers

4.3.1 Trapping force for metallic dimer particles by virtual probes

The average force using Eq. (3.19). 5 nm grids were used in the FDTD simulation was calculated and the electromagnetic fields in the 3D space can be obtained. The simulation results were converged under this grid parameter. The total force was the combination of the individual force calculated for each surface point on the nanoparticle. Fig. 4.9 showed the calculated force in x-z plane. Since the field distribution was symmetrical with respect to x-z plane, forces in y direction

cancelled each other. Therefore, the force distribution in Fig. 4.9 indicated the actual force exerted on the particles.

In Fig. 4.9(a), when a single particle was considered and placed on the left virtual probe (0.1 μm off the center), the force direction was in negative z direction. This suggested that the particle can be stably trapped by the virtual probe on the left.

In Fig. 4.9(b), a gold nanosphere was placed slightly off the center and to the left of the virtual probe. Apart from the main force in the negative z direction, there was additional forces exerted on the particle in positive x direction (white arrow), which can move the particle to the left virtual probe.

Then the situation when the second particle was introduced into the system was examined, as shown in Fig. 4.9(c). It was found that these two particles were trapped by pulling forces to the surface due to enhanced localized field of the virtual probes. This proved that the virtual probe pair in the model formed two trapping wells for gold nanoparticles. This further suggested that the spacing between the two particles can be adjusted by changing the lobe locations in the plasmonic field. In the simulation, the virtual probe spacing was approximately 210 nm and the radius of the nanosphere was 100 nm. As a result, the gap was a 10 nm [Fig. 4.9(c)]. In practice, the particle size and shape could be irregular. Nevertheless, simulations suggested that the spacing tuning of a dimer was possible in plasmonic tweezers.

The trapping of nanorods in the system was further investigated, as the nanorod is a common type of nanoparticles and can be easily synthesized in solution. Fig. 4.9(d) shows the force distribution around the nanorods, most of the forces are downwards and upwards. The forces exerted on both nanorods were similar, leading to a stable spacing. The trapping force was resulted from the coupling between SPPs and LSPs. Essentially the force comes from the interaction between charges. The

free electrons were redistributed as a result of interaction between the optical field and free electrons. These results demonstrated that other nanoparticles at different shapes and sizes could be trapped by the plasmonic field in the system described here.

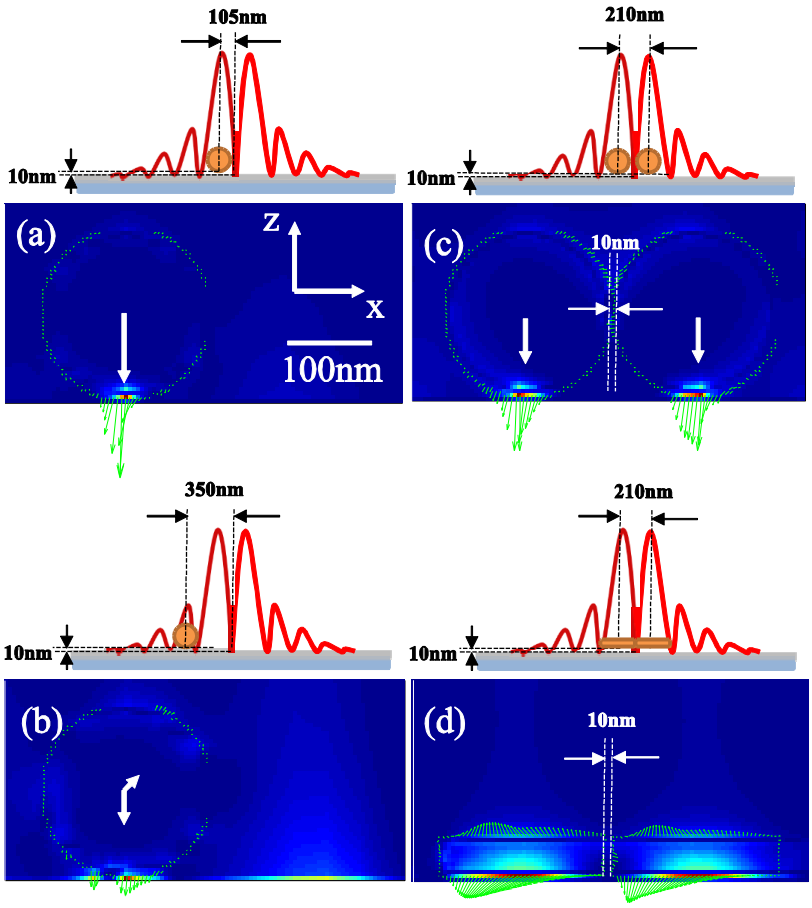

Fig. 4.9 The force analysis for: a single 200 nm diameter gold nanosphere (a) placed on the left virtual probe, 0.1 μm off the center and (b) placed 0.35 μm off the center; (c) two gold nanospheres (diameter 200 nm), trapped by the plasmonic field; and (d) two gold nanorods (200 nm long and 40 nm in diameter). Green and yellow arrows show the force around the particle in x-z plane. The white arrows show the total force. The schematic diagrams show the locations of particles in the plasmonic field.

4.3.2 Force distribution of a gold nanosphere in the plasmonic field

In order to explain further the plasmonic trapping mechanisms, the exerted forces on a gold nanosphere at different locations in the plasmonic field were calculated. Firstly, the particle was placed above the left plasmonic lobe and was

moved away from the substrate along z direction. It can be seen in Fig. 4.10 that the force increased exponentially when the particle was moved closer to the substrate. Note that the buoyancy of the particle and the upwards force from thermal convection can counteract that the particle would accelerate into surface. As was proven by Zhan *et al*. [113], since the excited field was a non-diffraction field, the force distributions in x direction remain similar for particles with different z coordinates.

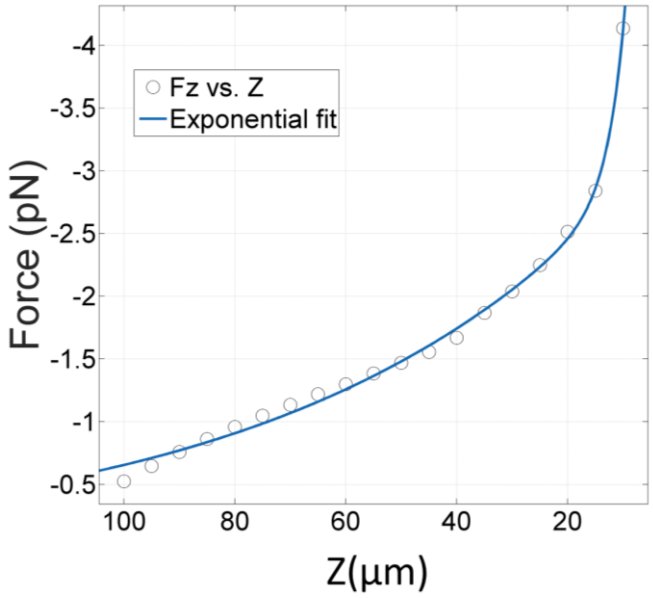

Fig. 4.10 Calculated forces on gold nanoparticles in the plasmonic field when the gold nanoparticle was placed above the trapping lobe and moved towards the Ag-film substrate. z indicates the distance between the particle bottom and the film surface. Negative force means the force direction is in negative z.

Fig. 4.11 shows how forces vary in x direction. The plasmonic field force was strongest at around 100 nm away from the center (the location of the virtual probe) and became smaller when moved away from the center. The fluctuation was a result of the Bessel distribution of the plasmonic field.

In Fig. 4.12, the forces in x direction were calculated. It can be seen that the force in x direction (F_x) was much smaller than the force in z direction (F_z), and therefore forces in z direction was dominant in the particle trapping. In addition,

when the distance to the center was less than 0.615 μm, the force became an attracting force, which can move the particle towards the virtual probe.

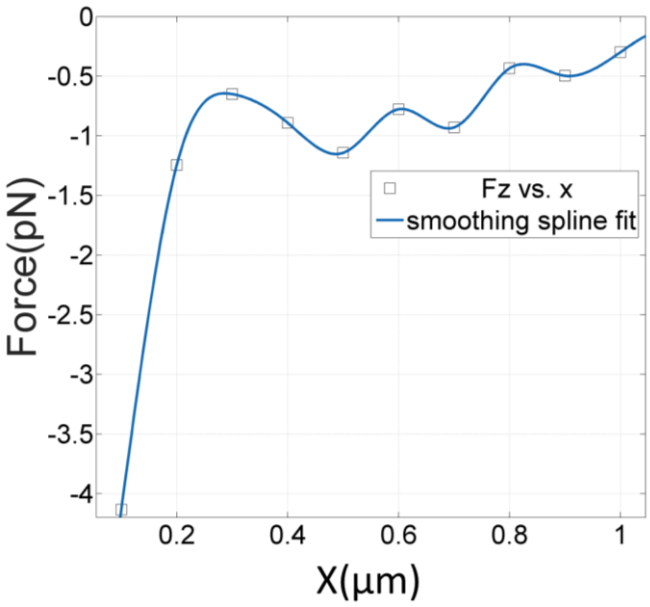

Fig. 4.11 Calculated forces on gold nanoparticles in the plasmonic field when the gold nanoparticle was placed 10 nm above the Ag film and moved away from the center of virtual probe (x=100 nm) in x direction.

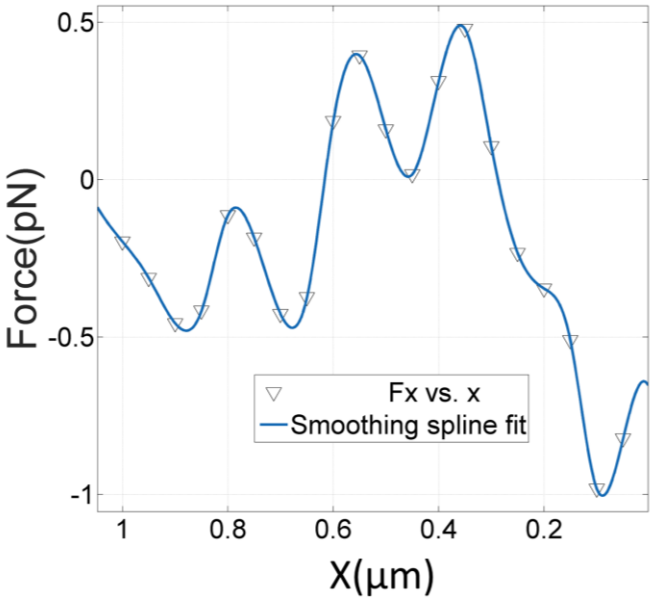

Fig. 4.12 Calculated forces on gold nanoparticles in the plasmonic field when the calculated force in x direction under the same condition as that in Fig. 4.11, and the negative force means the direction away from the center.

The trapping mechanisms for metallic particle dimers have been investigated from two aspects. In subsection 4.3.1, the trapping force for metallic dimer particles by virtual probes has been studied. This result shows the virtual probes have the capability to attract the particles. In subsection 4.3.2, the force distribution of a gold nanosphere in the plasmonic field has been calculated. This result shows the virtual probes have the capability to confine the particles. The designed SP-VP pair can be regarded as trapping potential wells.

4.4. Tuning mechanism for metallic particle dimers

The possibility of controlling the spacing between the two virtual probes was also studied for dimer spacing control. This spacing can be calculated by using Eq. (4.23). It was assumed that the two virtual probes were located on x axis and the light was linearly polarized in x direction ($\varphi = 0$). Since the transmission efficiency for p polarization components was maximum at θ_{sp}, we can obtain the relation $E_t(\rho) \sim J_1(k_2 \rho \sin\theta_{sp})$ based on Eq. (4.23), by assuming the integration variable to be θ_{sp}. Therefore, the virtual probes spacing was a function of θ_{sp}, as $k_i = k_0 n_i$ can be regarded as a constant.

According to surface plasmon excitation dispersion relation, θ_{sp} was determined by both the incident wavelength and the permittivity of Ag. The permittivity of Ag was wavelength-dependent and can be approximated based on Drude-Lorentz model described in [148]. By taking into account the frequency dependent permittivity of Ag using Drude-Lorentz model. Consider multiple Lorentz resonance terms,

$$\varepsilon_r(\omega) = \varepsilon_r^{(f)}(\omega) + \varepsilon_r^{(b)}(\omega) = 1 - \frac{{\Omega_p}^2}{\omega(\omega - i\Gamma_0)} + \sum_{j=1}^{k} \frac{f_j {\omega_p}^2}{({\omega_j}^2 - \omega^2) + i\omega\Gamma_j} \qquad (4.24)$$

The intraband part $\varepsilon_r^{(f)}(\omega)$ of the dielectric function is described by the free-electron or Drude model. The interband part of the dielectric function $\varepsilon_r^{(b)}(\omega)$ is described by the simple semiquantum model resembling the Lorentz result for insulators. k is the number of oscillators with frequency ω_j, strength f_j, and lifetime $\Omega_P = \sqrt{f_0}\omega_p$, while Ω_p is the plasma frequency associated with intraband transitions with oscillator strength f_0 and damping constant Γ_0. ω_p is the plasma frequency. These parameters are available in Table 3 in [148].

Therefore, the virtual probe pair spacing was a function of the excitation wavelength and the calculated result was given in Fig. 4.13. The kink around 630 nm could be caused by the surface plasmon resonance. The spectrum from 330 nm was chosen, as the real part of the silver permittivity is no more negative below 320 nm and it works as bulk silver. Therefore, no SPPs will be excited below that wavelength. This result suggested that the particle spacing in the dimer can be tuned by changing the excitation wavelength.

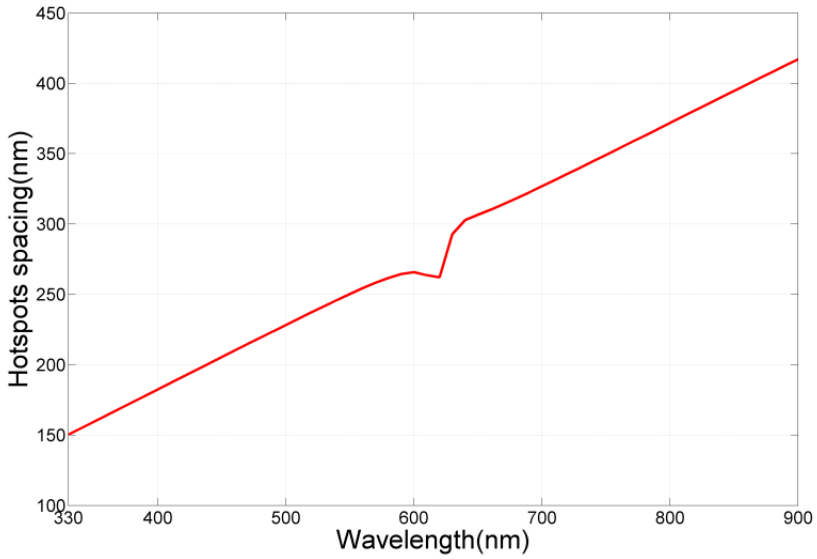

Fig. 4.13 Calculated virtual-probe-pair spacing as a function of the incident light wavelength

4.5 SERS application of the horizontal dimer

Finally the LSPR and the electric field enhancement were investigated in the proposed system. The incident laser wavelength is 532 nm. The relation in Eq. (2.29) was used to estimate the filed enhancement [149].

In Fig. 4.14(a), the surface plasmon was excited by a linearly polarized beam. Two strong LSPRs can be seen clearly, leading to an enhancement of ~20 times, which agreed well with the theoretical results based on Fresnel transmission calculation (Fig. 4.5). The field distribution in z direction matched the force curve shown in Fig. 4.10.

By placing a single gold nanosphere of diameter 200 nm on the Ag film, as shown in Fig. 4.14(b), the SPR became more localized with a greater enhancement near 130 in the 10 nm gap between the particle and the film, while the other virtual probe reduced in intensity due to the strong absorption resulted from the gold nanosphere.

Fig. 4.14(c) shows the situation when a dimer was introduced into the system. The gap of the gold nanosphere dimer was set to 10 nm and the distance between the nanospheres and the film remained at 10 nm. The hot spots were localized in the gaps between the particles and the film, and no strong LSPR was observed between two nanoparticles. This is because that LSPR is highly dependent by the direction of polarization of the incident light. The plasmonic field in the dimer gap was perpendicular to the light polarization direction, and a weaker LSPR occurs. In Fig. 4.14(c), the electric field enhancements for both particle-film gaps were about 60 (less than half of 130). Strong LSPR in particle-film gaps and weak LSPR between particles was a result of the plasmonic field distribution.

Further comparison was made in Fig. 4.14(d) to show the potential applications of trapped gold nanoparticle dimer in SERS. An excitation beam linearly-polarized in x direction was used to achieve an electric field enhancement factor near 1300.

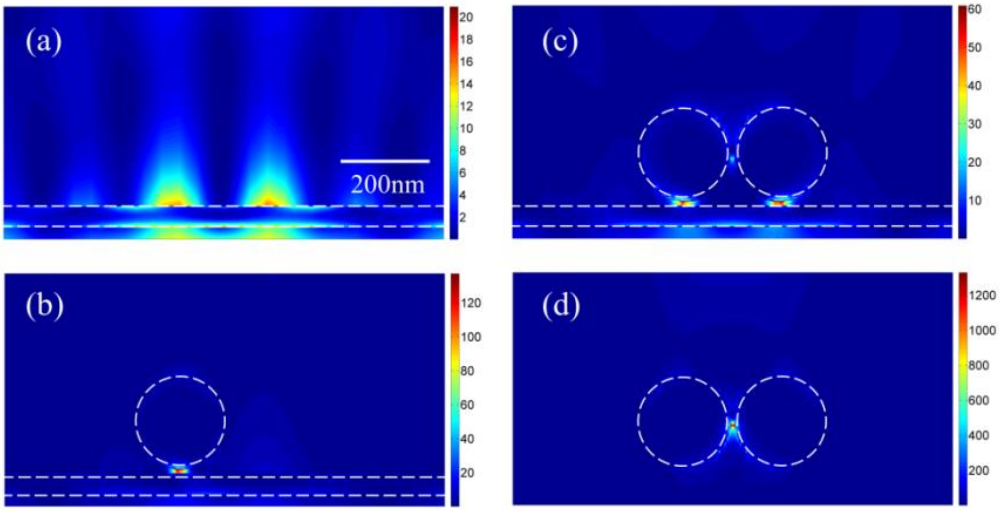

Fig. 4.14 The calculated electric field enhancement in x-z plane, when: (a) no gold particles; (b) one gold nanosphere placed on the Ag film; (c) a gold nanosphere dimer placed on the gold film; (d) the nanosphere dimer was illuminated by a focused linearly polarized beam, the polarization direction in horizontal. Dashed circles are the gold nanospheres (diameter: 200 nm). The gap between the Ag film and the nanoparticle is 10 nm. The spacing between two nanospheres in the dimer is 10nm. The dashed lines are the top and bottom of the Ag film (thickness: 45 nm).

4.6 Summary

In conclusion, a focused plasmonic tweezers system was presented for manipulating the metallic nanoparticle dimers. It was found that the field of virtual probe pair with strong field concentration can be formed by focused linearly-polarized beam excitation. This virtual probe pair is capable of trapping simultaneously two free-standing nanoparticles including nanospheres or nanorods. It has also been theoretically proved that the gap spacing between the nanoparticles in the dimer can be tuned by changing the excitation wavelength. This work presented is the first study on the trapping of metallic particle dimer. This can be

considered as a step towards the development of new plasmonic trapping technologies for multiple metallic particles, where no nanofabrication is involved. This technique can achieve a high resolution beyond the optical diffraction limit for nanoscale manipulation. The proposed method may serve as a new way of realizing strong LSPR hot spots for SERS detections with single molecule sensitivity.

Chapter 5 Vertically-oriented metallic particle dimer based on focused plasmonic tweezers

5.1 Introduction

Metal nanostructures have been intensively studied both theoretically and experimentally. Due to the interaction between the incident photons and the free electrons in the metal nanostructures, plasmon resonance can be generated at the vicinity of the nanostructure and an enhanced electric field can be observed. A typical application is in SERS where the metal nanostructures causes significantly increase Raman signals. These metal nanostructures can be simply divided into horizontal and vertical orientations. Horizontal direction structures can be in the form of horizontal-oriented nanoparticle dimer [74, 132], nanorods antenna [150, 151] and bow-tie nanostructure [133, 152]. Vertical direction structures include nanoparticle-dielectric substrate [153], tip-dielectric substrate [154], nanoparticle-film [155, 156] and tip-film [157, 158]. Compared to horizontally-oriented structures, vertically-oriented structures provide additional benefit with its scanning capability. Therefore, vertically-oriented structures have great potential in the area of scanning Raman imaging.

The ability to detect single molecule in solution with high sensitivity and molecular specificity is of great scientific and practical interest in many fields such as chemistry, biology, medicine, pharmacology and environmental science. Single molecule detection using SERS was first achieved using nanoparticles where the Raman signal enhancement can be explained by simple LSPR [159]. It has been shown that gap mode nanostructures such as horizontally- or vertically- oriented dimers provide much greater Raman enhancement, owing to the SPP-LSP coupling

or LSP-LSP coupling. The electric field enhancement created from the LSP hybridization could be three orders of magnitude larger than that from monomers, depends on the shape, size, and orientation of the dimer nanoparticles [25]. Horizontally-oriented dimer structures can be physically fabricated or assembled on a plane substrate using nanofabrication techniques and they have been a subject of extensive investigations [133, 150, 151]. For dynamic control of the forming of the dimer structure, plasmonic trapping of nanoparticle is a promising technique [21, 22, 104, 105, 107, 109]. In Chapter 4, it has been shown that horizontally-oriented dimer structures can also be formed through plasmonic trapping by virtual probe pairs. However, these horizontally-oriented dimer structures have no scanning capability thus they are not suitable for high-resolution Raman spectroscopy imaging applications.

In addition, the axis orientation of the dimer structure is of significant importance since the coupling efficiency reaches its maximum when the polarization of the incident light is aligned parallel to the axis of the dimer structure [26, 27]. Usually the focal light field has transverse and longitudinal components. The horizontally- and vertically- oriented dimers are sensitive to transverse and longitudinal components, respectively. Particularly for high-order laser mode beams such as RPB, their longitudinal components are dominant after being focused. The vertically-oriented dimer will be able to take this advantages thus provides even stronger Raman signal enhancement.

In this chapter, a vertically-oriented dimer (a particle-particle-film system) was proposed. It can serve as a simple conceptual model for revealing the electric field enhancement underlying SERS application [34]. In this vertically-oriented dimer system, the bottom nanoparticle is immobilized above the Ag film by the

focused plasmonic tweezers method introduced in Chapter 3 and the top nanoparticle can be regarded as the AFM tip which enables precise locating above the bottom particle. The gap distance of the dimer can thus be accurately adjusted by the AFM tip. SP-VP could be a great candidate in building vertical nanostructure system. On the one hand, SP-VP can provide strong gradient force that allows the bottom nanoparticle to be manipulated. On the other hand, SP-VP has dominant longitudinal component [113, 127] that couples very efficiently with the vertically-oriented dimers thus provide further improvement of the Raman enhancement.

The field distribution of SP-VP excited by focused RPB was firstly derived. MST method was applied to calculate the force based on the FDTD simulation of the system with RPB incidence. Trapping potential associated with force distribution was also calculated for the technical analysis. Extensive numerical simulations have subsequently been performed to study the effect of the gap distance of the proposed dimer structure on the electric filed enhancement. Lastly, a simply physical model was proposed based on simplified dipole approximation to understand the coupling mechanisms for the observed electric field enhancement in the proposed particle-particle-film system.

5.2 Theories about the vertical dimer system

5.2.1 Theoretical description of surface plasmon virtual probe

Employing angular spectrum representation [143] and theory established by Richards and Wolf [144], the focal field can be obtained as follows:

$$E_{t,z}(\rho,\varphi,z)=\frac{ife^{-ik_1 f}}{2\pi}\int_0^{\theta_{\max}}\int_0^{2\pi}-E_{inc}(\theta,\phi)\cos\phi e^{ik_2\rho\sin\theta\cos(\phi-\varphi)}e^{i(k_{z1}-k_{z2})z_0}t^p e^{izk_{z2}}\frac{k_2^{\,2}}{k_1}\sin^2\theta\sqrt{\cos\theta}\,d\theta d\varphi \tag{5.1}$$

where ρ is the distance from the excitation point, φ is the angle with respect to the polarization direction and z is the distance to the metal film, f is the radius of Gaussian reference sphere for the incident beam, E_{inc} is the incident electric field, k_1 and k_2 are the propagating wave vectors in the substrate and in the sample respectively, subscript z indicates the longitudinal component, Z_0 represents the distance from the laser focus to the metal film, and t^p is the transmission coefficient. According to the work by Zhan [113, 127], the longitudinal component is much stronger and dominates the total field distribution, which is sued in this study here.

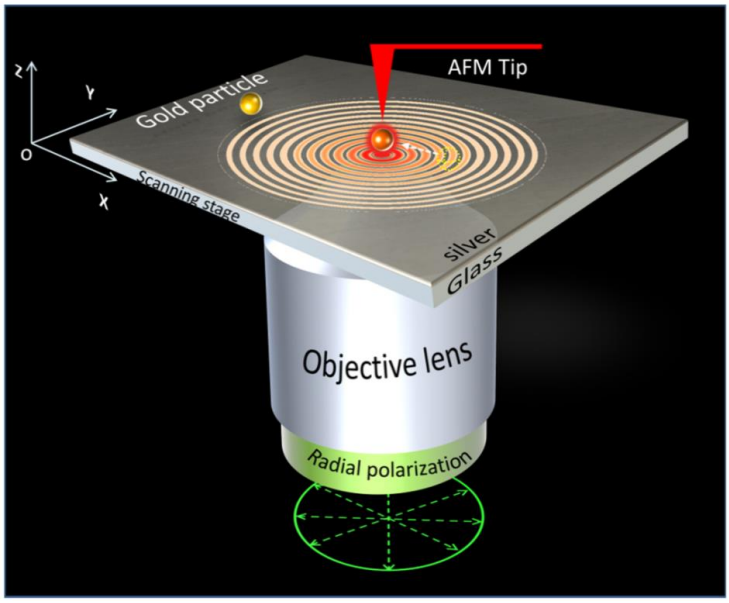

Fig. 5.1 (a) The proposed plasmonic tweezers system. The incident light is linearly-polarized and is focused to a 45 nm-thick silver film through a 1.49-NA objective lens.

The proposed plasmonic tweezers system is shown in Fig. 5.1. The plasmonic field is excited on the Ag film by a focused RPB. As the surface plasmon is sensitive to TM polarization, a circle of light can excite surface plasmon on the Ag film, when they propagate to the center, a virtual probe with its maximum electrical filed at the center (Fig. 5.2) will be formed as a result of a constructive interference.

This virtual probe can be used to trap gold nanoparticle. When the dimer structure is formed and fixed by both the trapped gold nanoparticle and the AFM tip, the scanning function can be achieved by the relative movement of the Ag film attached with solution sample.

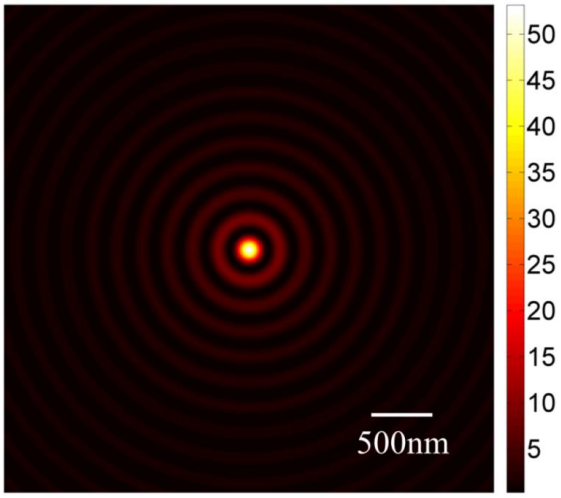

Fig. 5.2 Top-view of the plasmonic field (showing the z direction electrical-field distribution 10nm above the silver layer. Z_0=1 μm and $f_0 = 1$. The laser wavelength is 532 nm.

Radially polarized doughnut mode can be synthesized with (1,0) mode [160],

$$\mathrm{RP} = \mathrm{HG}_{10}\,\mathbf{n}_x + \mathrm{HG}_{10}\,\mathbf{n}_y \tag{5.2}$$

To determine the focal fields of the other two doughnut modes, we need to derive the focal fields for the y polarized modes. This is accomplished by rotating the existing fields by 90^o around the z axis.

Expressing the Cartesian coordinates $(x_\infty, y_\infty, z_\infty)$ by the spherical coordinates (f, θ, ϕ) we find the incident field of (1,0) mode,

$$E_{inc} = E_0(2x_\infty / \omega_0)e^{-(x_\infty^2+y_\infty^2)/\omega_\infty^2} = (2E_0 f / \omega_0)\sin\theta\cos\phi e^{-f^2\sin^2\theta/\omega_0^2} \tag{5.3}$$

where $f_0 = \dfrac{\omega_0}{f\sin\theta_{\max}}$ is the filling factor. ω_0 represents the beam waist for the Gaussian beam and $f\sin\theta_{\max}$ is the aperture radius of the reference lens.

For simplification, we can write the exponential function as

$$f_\omega(\theta) = e^{-\frac{\sin^2\theta}{f_0^2 \sin^2\theta_{\max}}} \tag{5.4}$$

This function is called the apodization function and can be viewed as a pupil filter.

Substitute the x- and y- polarized (1,0) mode incident field to the Eq. (5.1), we can get the focal field respectively as below:

$$E_{t,z}(\rho,\varphi,z) = \frac{ife^{-ik_1 f}}{2\pi} \int_0^{\theta_{\max}} \int_0^{2\pi} -(2E_0 f/\omega_0) f_\omega(\theta) \cos^2\phi e^{ik_2\rho\sin\theta\cos(\phi-\varphi)} e^{i(k_{z1}-k_{z2})z_0} t^p e^{izk_{z2}} \frac{k_2^2}{k_1} \sin^3\theta\sqrt{\cos\theta}\, d\theta d\phi \tag{5.5}$$

$$E_{t,z}(\rho,\varphi,z) = \frac{ife^{-ik_1 f}}{2\pi} \int_0^{\theta_{\max}} \int_0^{2\pi} -(2E_0 f/\omega_0) f_\omega(\theta) \sin^2\phi e^{ik_2\rho\sin\theta\cos(\phi-\varphi)} e^{i(k_{z1}-k_{z2})z_0} t^p e^{izk_{z2}} \frac{k_2^2}{k_1} \sin^3\theta\sqrt{\cos\theta}\, d\theta d\phi \tag{5.6}$$

The total focal field excited by focused RPB can be obtained by linear superposition of these two fields:

$$E_{t,z}(\rho,\varphi,z) = \frac{ife^{-ik_1 f}}{2\pi} \int_0^{\theta_{\max}} \int_0^{2\pi} -(2E_0 f/\omega_0) f_\omega(\theta) e^{ik_2\rho\sin\theta\cos(\phi-\varphi)} e^{i(k_{z1}-k_{z2})z_0} t^p e^{izk_{z2}} \frac{k_2^2}{k_1} \sin^3\theta\sqrt{\cos\theta}\, d\theta d\phi \tag{5.7}$$

Using the mathematical identity $\int_0^{2\pi} e^{ix\cos(\phi-\varphi)} = 2\pi J_0(x)$, we can simplify this equation:

$$E_{t,z}(\rho,\varphi,z) = ife^{-ik_1 f} \int_0^{2\pi} -(2E_0 f/\omega_0) f_\omega(\theta) J_0(k_2\rho\sin\theta) t^p e^{i(k_{z1}-k_{z2})z_0} e^{izk_{z2}} \frac{k_2^2}{k_1} \sin^3\theta\sqrt{\cos\theta}\, d\theta \tag{5.8}$$

5.2.2 Dipole approximation of single or two nanoparticles

In order to study the behaviors of nanoparticles on the metal film, simplified dipole approximation was used for analytical analysis. It was used only to qualitatively explain the electric field enhancement, while quantitative results were obtained using the FDTD simulation. Radiative corrections will not be discussed in this approximation, and interested readers can refer to [161]. For single particle system as shown in Fig. 5.3(a), its polariability is [162]

$$\alpha(\omega) = 4\pi R^3 \frac{\epsilon(\omega) - \epsilon_m}{\epsilon(\omega) + 2\epsilon_m} \tag{5.9}$$

where R is the radius of the sphere, $\epsilon(\omega)$ is the permittivity of the sphere and ϵ_m is the dielectric constant of the ambient.

The dipole moment of the sphere is

$$\mathbf{p} = \alpha\epsilon_0\epsilon_m\mathbf{E} \tag{5.10}$$

where ϵ_0 is the permittivity of vacuum.

The induced electric field by the sphere is

$$\mathbf{E} = \frac{3(\mathbf{p}\bullet\mathbf{r})\mathbf{r} - \mathbf{p}r^2}{4\pi\epsilon_0\epsilon_m r^5} \tag{5.11}$$

According to [162], the absorption cross section and scattering cross section are as follows:

$$C_{abs}(\omega) = k\,\mathrm{Im}\,\alpha(\omega) \tag{5.12}$$

$$C_{sca}(\omega) = \frac{k^4}{6\pi}\left|\alpha(\omega)\right|^2 \tag{5.13}$$

where $k = |\mathbf{k}|$ is the wavenumber.

For a particle-particle system as shown in Fig. 5.3(b), their effective polarizability can be calculated with considering the induced electric field

influencing each other [163, 164]. Since the incident electric field is parallel to the axis of the dimer structure (i.e., the line connecting the centers of the dimer spheres), the local electric dipole field induced by the other particle is $p_2/(2\pi\epsilon_0\epsilon_m l^3)$, so

$$\mathbf{E}_1^{loc} = \mathbf{E}_0 + \mathbf{p}_2/(2\pi\epsilon_0\epsilon_m l^3) \tag{5.14}$$

$$\mathbf{E}_2^{loc} = \mathbf{E}_0 + \mathbf{p}_1/(2\pi\epsilon_0\epsilon_m l^3) \tag{5.15}$$

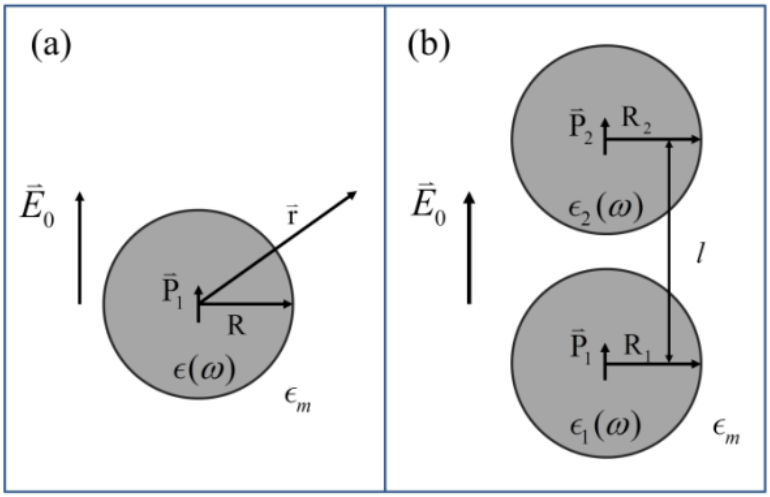

Fig. 5.3 Geometry of the dipole model: (a) single sphere; (b) vertical spheres dimer.

Substituting the expressions for the dipole moments $\mathbf{p}_1 = \alpha\epsilon_0\epsilon_m\mathbf{E}_1^{loc}$ and $\mathbf{p}_2 = \alpha\epsilon_0\epsilon_m\mathbf{E}_2^{loc}$ to the equation above and solving the two coupled linear equations, we can obtain the effective polarizability as follows:

$$\alpha_1^{eff} = \alpha_1 \frac{1+\alpha_2/(2\pi l^3)}{1-\alpha_1\alpha_2/(2\pi l^3)^2} \tag{5.16}$$

$$\alpha_2^{eff} = \alpha_2 \frac{1+\alpha_1/(2\pi l^3)}{1-\alpha_1\alpha_2/(2\pi l^3)^2} \tag{5.17}$$

The overall effective polarizability of the two particles is

$$\alpha^{eff} = \frac{\alpha_1+\alpha_2+2\alpha_1\alpha_2/(2\pi l^3)}{1-\alpha_1\alpha_2/(2\pi l^3)^2} \tag{5.18}$$

5.3 Force analysis of dimer particle

5.3.1 Optical forces of dimer particles

In Chapters 3 and 4, it has been demonstrated that 1 μm and 200 nm gold nanoparticles can be trapped by SP-VP. Here we will see that 50 nm diameter gold nanoparticle can also be trapped by the SP-VP. Optical force is important for the bottom particle being maintained in close proximity to Ag film. First the force distribution was calculated via Eq. (3.19) based on the 3D electrical and magnetic fields data obtained from the FDTD simulation. The incident fields in simulation are unit peak normalized with power 1 W. As shown in Fig. 5.4, the force in x-z plane was used to represent the force distribution on the gold nanoparticle. Although both the incident light and the system have symmetry, the force distribution around the particle is still a bit asymmetrical. This may be caused by the grid meshing. As shown in Fig. 5.4(a), the calculated total force is in z direction is -20.844 pN, and the forces in x- and y- directions are about one order of magnitude smaller.

We will now consider the situation when another gold nanoparticle intrudes from the top, e.g. a particle-particle dimer system, as shown in Fig. 5.4(b). The total force on the bottom particle of the dimer in z direction is -3.3561 pN, and the forces in x- and y- directions are about two orders of magnitude smaller. Compared with the single particle [Fig. 5.4(a)], the total force is still in positive z direction, but it is smaller, it is weakened by the attracting force owning to the charges of the two polarized particles, which can be seen from the charge distribution in Fig. 5.18. Nevertheless, the force at this level is still enough to control a nanoparticle above the silver film.

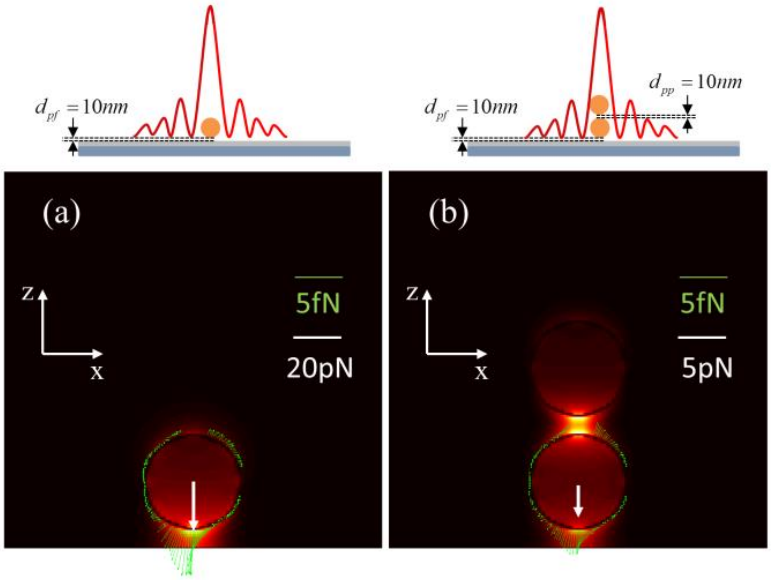

Fig. 5.4 The force analysis for: a single 50 nm diameter gold nanosphere: (a) placed on an Ag film; (b) a sphere is added to (a). The schematic diagrams show the locations of particles in the plasmonic field. d_{pp} and d_{pf} indicate the dimer gap distance and the particle-film gap dimer distance respectively. The green arrows show the forces at the points on the x-z section circle of the sphere. The white arrows indicate the total force as a result by the integral of the sphere surface. The background maps correspond to the electric fields.

About the force of the top particle, it is in negative z direction according the charge distribution in Fig. 5.17(b). The force has been calculated, as shown in Fig. 5.5. In practical application, the top particle can be substituted by an AFM tip/probe, which is mechanically controllable.

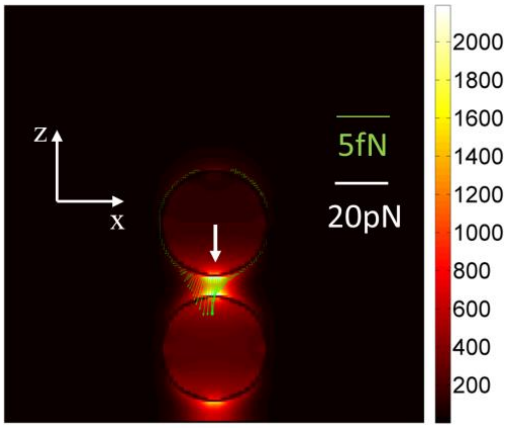

Fig. 5.5 The force analysis for the top particle of the vertical dimer. The indicators are same as in Fig. 5.4. The incident light wavelength is 532 nm. F_x=-3.3504 pN, F_z=-14.476 pN.

The working wavelength will affect the polarizability of metallic nanoparticle and the actual force as well. A force analysis has been done at a different working wavelength of 633 nm, as shown in the Fig. 5.6. Comparing to the working wavelength in 532 nm, the z direction forces increase in both without and with the top particle. A force analysis was also done for the top particle in the working wavelength of 633 nm, the force also increases, as shown in Fig. 5.7. These results indicate stronger interaction occurs in the wavelength of 633 nm.

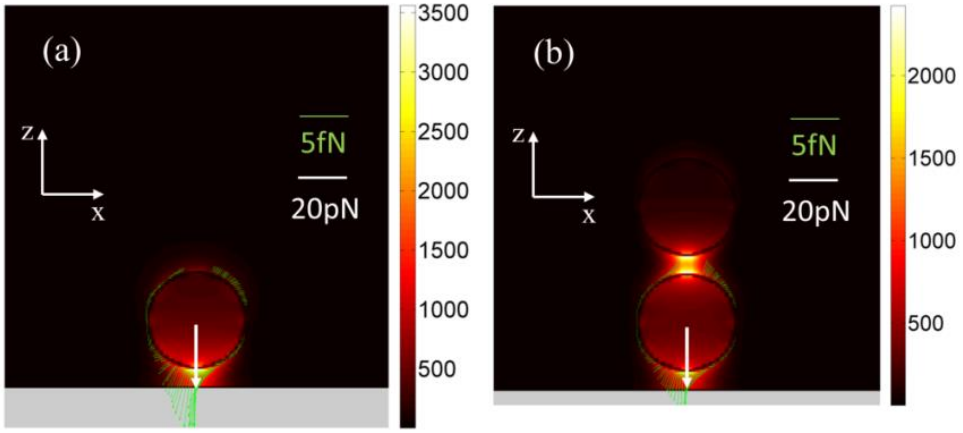

Fig. 5.6 The force analysis for: a single 50nm-diameter gold nanosphere: (a) placed on an Ag film; (b) a sphere is added to (a). The indicators are same as in Fig. 5.4. The incident light wavelength is 633 nm. (a) F_x=-6.0401 pN, F_z=-26.278 pN; (b) F_x=0.73192 pN, F_z=-6.2573 pN.

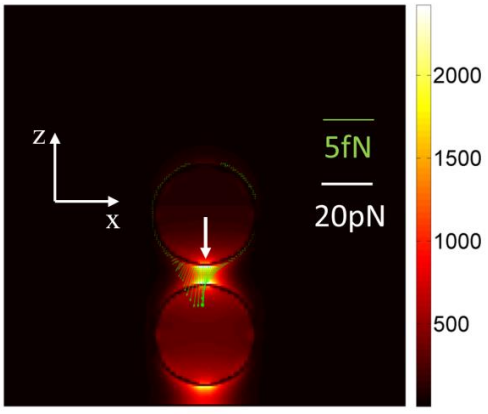

Fig. 5.7 The force analysis for the top particle of the vertical dimer. The indicators are same as in Fig. 5.4. The incident light wavelength is 633 nm. F_x=-4.1405 pN, F_z=-16.382 pN

In this subsection, the forces of the top particle and bottom particle of the dimer were calculated. These can examine the optical confinement of the dimer. The trapping of the bottom particle is stable and it will not be affected by the top particle. The forces were also calculated in another wavelength, which shows similar results. Therefore, the trapping not only occurs in a special condition.

5.3.2 Trapping stability of the bottom particle

Trapping potential is important for a stable trapping of a particle. Trapping potential can be calculated by the following formula [165],

$$U(r_0) = \int_{\infty}^{r_0} \mathbf{F}(r) \cdot d\mathbf{r} \tag{5.19}$$

It means the trapping potential can be obtained if we get the force distribution in the radial direction. Generally, in order to overcome the motion from the thermal effects, more than 10 k_BT trapping potential depth is need for stable trapping [166], where k_B is the Boltzmann constant and T is the temperature.

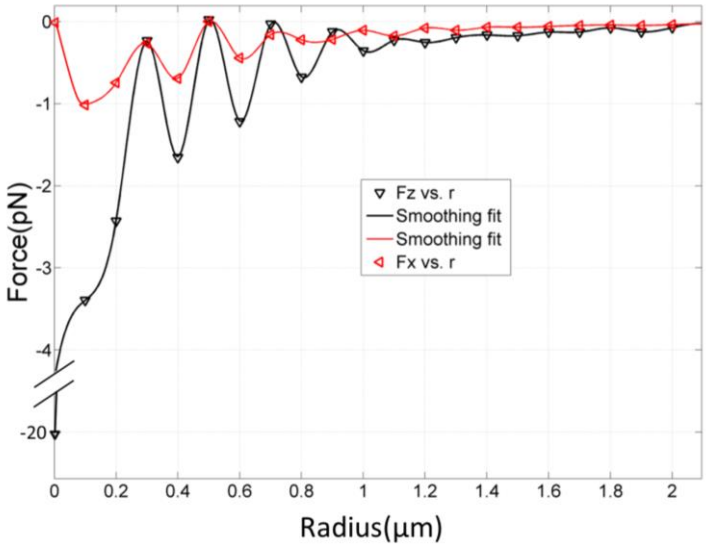

Fig. 5.8 The x- and z- direction total force distribution at the radial direction for single particle above the Ag film, the bottom particle is studied. The parameters are same to Fig. 5.4. Radius is the particle offset length to the SP-VP center. The force was obtained every 100 nm. Both the particle-film and the particle-particle distances are 10 nm. The incident power is 1 W.

According to Eq. (5.19), in order to obtain the trapping potential, the total forces distributions on the radial direction were calculated. As shown in Figs. 5.8 and 5.9, when the particle is away to more than 2 μm, the force becomes small (closed to 0) because of the sharply attenuated the plasmonic field. The x- and z-direction forces in the Fig. 5.9 are both relatively weaken, but the distribution patterns remain unchanged.

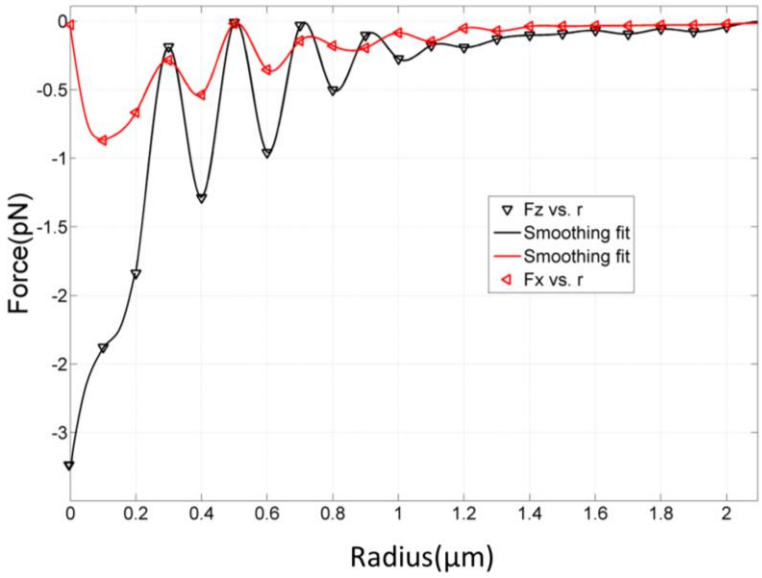

Fig. 5.9 The x- and z- direction total force distribution at the radial direction for vertically-oriented dimer above the Ag film, the bottom particle is studied. The other parameters are same to Fig. 5.8.

Temperature is another factor in this estimation as heating effect is an important issue in the plasmonic tweezers system [105]. However, in the proposed configuration, the beam is out of focus by about 2~3 μm thus the expected temperature change will not be significant. According to the temperature distribution calculations in [127], the temperature increase in the focused plasmonic tweezers system is estimated to be only about 2 Kelvins, as the gold metal film has a high thermal conductivity to dissipate the localized heating. Note that the silver metal film used here has relatively higher thermal conductivity than gold [167]. Therefore we take the temperature as 300 Kelvins in the estimation.

A conservative estimation was made for the trapping potential at the integral below 2 μm rather than infinity. The calculation results of trapping potentials without/with top particle are shown in Fig. 5.10. In the case of Fig. 5.8, the largest trapping potential is 111 k_B/W at the center, which means that about 90 mw incident power can maintain a table trap. In the case of Fig. 5.9, the trapping potential well also exists at the center, which is 92.3 k_B/W. It means that more than 108.3 mw power can maintain a stable trapping of a bottom particle. That is evidence that out proposed system can work well.

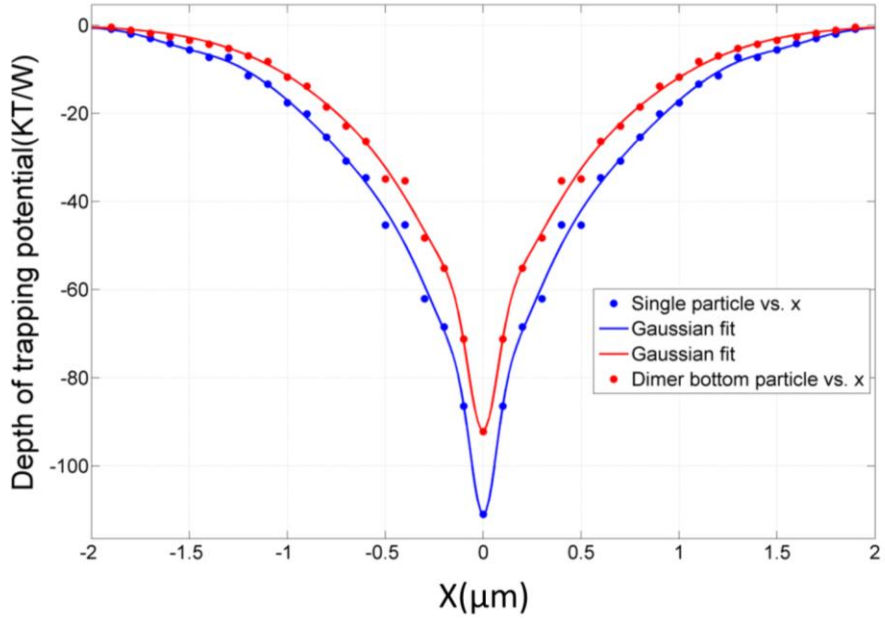

Fig. 5.10 The calculated trapping potential well along x direction for single particle (blue curve) and the bottom particle of the dimer (red curve).

In order to study the trapping stability, the trapping potential was calculated according to the force distribution in z direction, as shown in Fig. 5.11. The height is the distance between the particle bottom and the metal surface. The trapping potential value at the center is 115 k_B/W. It is bigger than the radical direction trapping potential. Thus, the calculated minimum power can maintain the trapping in three directions.

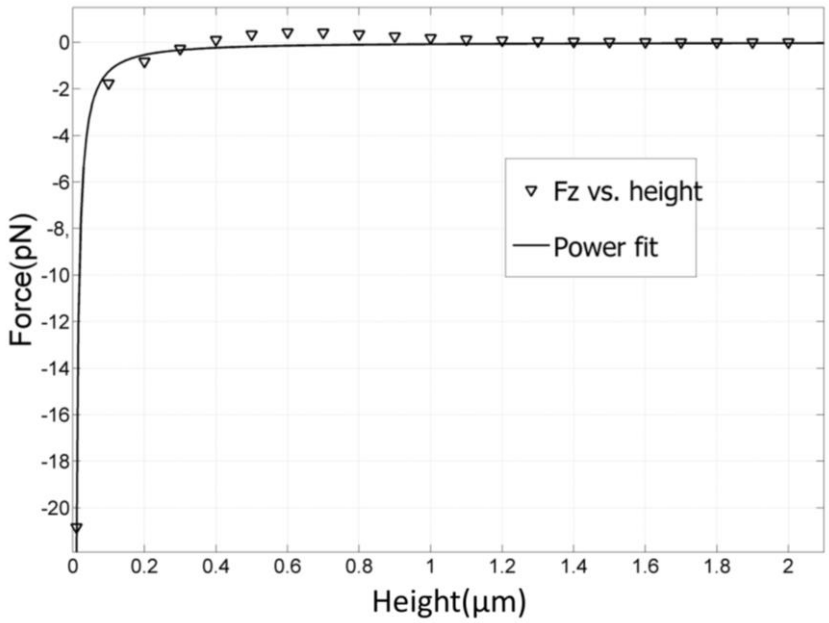

Fig. 5.11 The z- direction force distribution of the single particle at the center and off the Ag film with different height.

As we can see from each trapping potential well shown in the Fig. 5.10, there is no obvious local minima trapping well or barrier except the center, so center is the only possible trapping position for particle. But the position of an optically trapped particle may be not fixed. Depending on the exact trap morphology and depth, the particle could be confined over a rather large region of space. According to the equipartition theorem the thermal kinetic energy of a particle can be related to the optical potential energy of a trap with stiffness k [106]:

$$\frac{1}{2}KT = \frac{1}{2}k\left\langle x^2 \right\rangle \tag{5.19}$$

where $\left\langle x^2 \right\rangle$ is the variance of the displacement from the equilibrium position. Assuming that the stiffness of the 50 nm gold nanoparticle is 5.82 pN/nm/W [166], the square displacement $\left\langle x^2 \right\rangle$ at 300 Kelvins can be estimated to be about 0.71×10^{-18} m^2, corresponding to a displacement of 0.8 nm, which is acceptable in the field enhancement. From the optical potential well we can make more rigorous

estimation, the probability function for the displacement of a trapped particle can be deduced [168, 169]:

$$p(x) \propto \exp\left(\frac{-U(x)}{KT}\right) = \exp\left(\frac{-kx^2}{2KT}\right) \tag{5.20}$$

The displacement x can be regarded as the position where the probability p(x) decrease to 1/e of the value p(0), which corresponds 0.43 k_B trapping potential difference. Assuming the center has trapping potential 10 k_B, we can calculate the displacement is about 1.7 nm and 0.08 nm at x- and z- directions, respectively. Thus the impact of displacement on the electric field enhancement is acceptable.

In this subsection, the forces of particle in the plasmonic field were firstly calculated. The force distribution shows the particle has the tendency of moving to the center of the SP-VP. The SP-VP has the capability to attract the particle, and it is not affected by the top particle. Then the temperature of the particles system was evaluated. It showed no obvious temperature increase. Then the trapping potentials in x- and z- directions can be obtained with the force distribution results, and these show great trapping stability, which is important for maintaining strong electric field enhancement.

5.4 SERS application of the vertical dimer

5.4.1 Electric field enhancements

Next, in order to study the SERS application of this vertical dimer system, the electric field enhancement calculation as well as three other structures as comparison have been done, as shown in Fig. 5.12. The colorbar of Fig 5.12 is logarithmic scale in base 10. In single molecule SERS, the Raman enhancement

factor is around 10^{12}, which suggests the electrical enhancement factor would have to be 10^3 according to Eq. (2.29) [149].

Fig. 5.12(a) shows the plasmonic field excited by the RPB. Without particle, the electric field enhancement factor is about 60 times. Comparing to traditional excitation method without SPPs, we have already obtained at least one order of magnitude for the electrical enhancement.

When a single particle is placed 10 nm above the Ag film [Fig. 5.12(b)], the electric field enhancement is over 2×10^3. The RPB excited plasmonic field is almost longitudinal component that has the same orientation as the vertical dimer.

When a vertical dimer is placed 10 nm above the Ag film [Fig. 5.12(c)], a much larger enhancement of over 2×10^3 is observed at the dimer gap. It is interesting to see that the enhancement at the dimer gap is larger than that at the particle-film gap at the same gap size. Note that the electric field enhancement of the proposed vertical dimer is relatively smaller than that of a single trapped particle. This is expected because the total available energy has to be shared between particle-film gap and the particle-particle gap for the dimer configuration. Both the vertical dimer and the trapped particle configurations lead to large enhancement that is sufficient for highly sensitive Raman applications such as single molecule detection. However, for the simple trapped particle configuration, the sample has to be attached/close to the metal surface. The proposed vertical dimer configuration is a further extension of single trapped particle system with added flexibility.

Fig. 5.12(d) shows a horizontally-oriented dimer with particle size and same gap distance above the Ag film exited by the same plasmonic field, but the enhancement is relatively lower , which is below 700 times. The hot spots locate at the bottom of the particles, because the incident field (SP-VP) for this dimer is

mainly longitudinal field. This indicates the vertically-dimer has better adaptability for electric field enhancement in some specific condition.

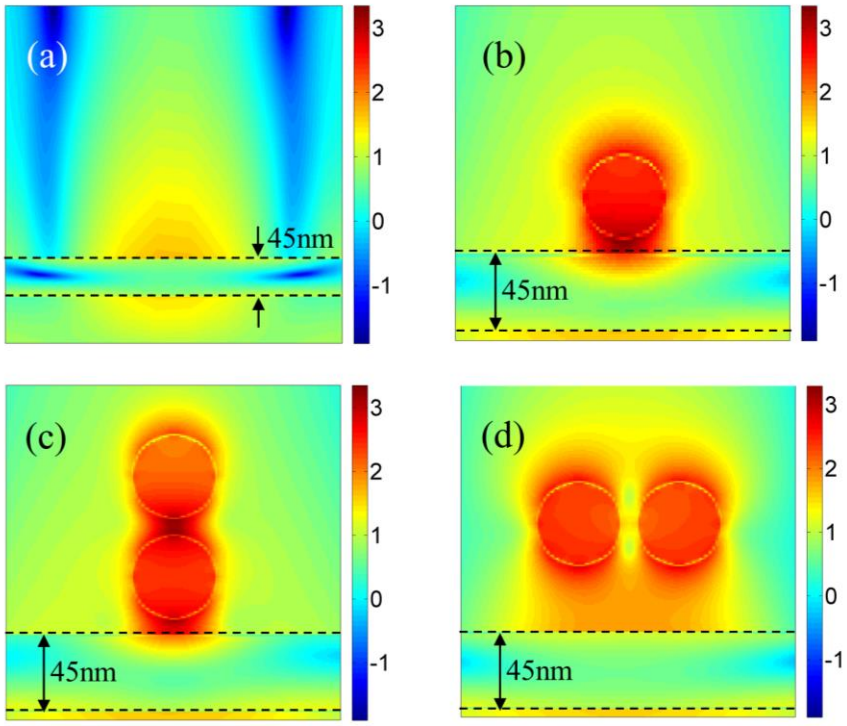

Fig. 5.12 The calculated electric field enhancement in x-z plane, when: (a) no gold particles, (b) a vertical dimer placed on the Ag film and $d_{pf} = d_{pp} = 10$ nm, (c) a horizontal dimer placed on the Ag film, the gap distance is same to 10 nm and the height of the gap center is same to (b), which is 65 nm from the surface.

We are also interested in the situation of $d_{pf} \neq d_{pp}$. In Fig. 5.13(a), the dimer gap distance is shorter than the particle-film gap distance. As the LSP-LSP will be relatively stronger than the LSP-SPP coupling and the smaller gap will have more absorption, the electric field intensity in the dimer gap is undoubtedly stronger than the particle-film gap. In Fig. 5.13(b), the will be a competition between the SP coupling effect and smaller gap size effect, the resultant electric field distribution indicates that the gap size effect dominates in this situation.

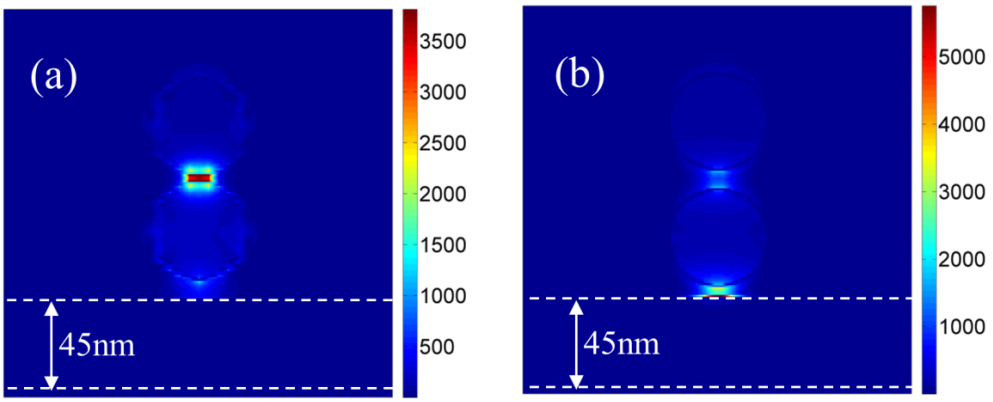

Fig. 5.13 The calculated electric field enhancement of 50 nm metallic particle dimers in x-z plane. (a) $d_{pp}=10$ nm and $d_{pf}=5$ nm. (b) $d_{pp}=5$ nm and $d_{pf}=10$ nm.

5.4.2 Gap distance dependent electric field enhancements

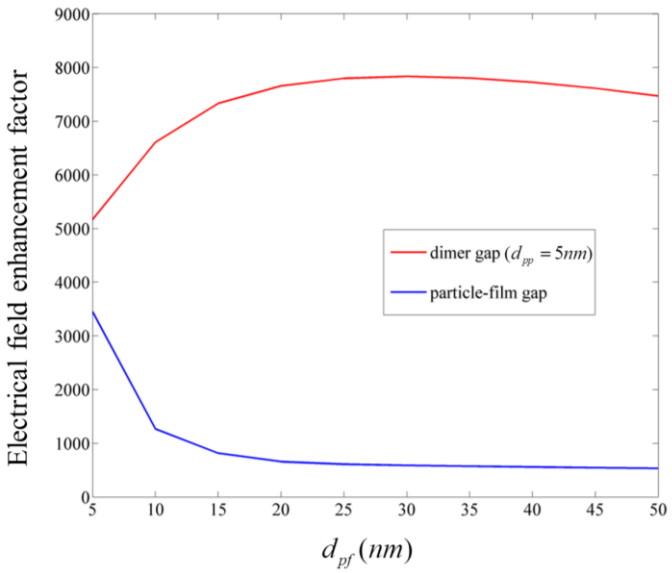

Fig. 5.14 The electric field enhancement when changing d_{pf}. The electric field enhancement factor is obtained at the point next to the particle where will present the highest electric field value.

In order to understand how the electric field enhancement depends on the particle-particle dimer gap distance d_{pp} and the particle-film gap distance d_{pf}, detailed calculations were performed . As shown in Fig. 5.14, when d_{pf} is larger than 20 nm, the dimer gap enhancement becomes stable. Since 50 nm is in near-field within the SPPs penetration depth, it can still excite the hot-spot in the dimer gap.

When d_{pf} is lower than 20 nm, the situation becomes complex. Although the particle-film gap will absorb part of the energy and its enhancement increases, the dimer gap enhancement is still higher than particle-film gap enhancement even when both d_{pp} and d_{pf} approaches 5 nm.

For further understanding of the situation when d_{pf} is below 20 nm, the measurement was made by varying d_{pp} from 1 nm to 20 nm with an interval of 1 nm. Four cases were studied that d_{pf} was chosen to be 5 nm, 10 nm, 15 nm and 20 nm respectively. The results are showed in Fig. 5.15. As expected, the electric field enhancement at the particle-film gap increases with the decrease of the d_{pf}. On the other hand, the electric field enhancement at the particle-film gap increases with d_{pp}. This can be understood that the introducing of the top particle will influence the plasmonic coupling since some of the energy will be shared within the dimer. On the contrary, the average enhancement in the dimer gap decreases with d_{pf}. The enhancement is inversely proportional to d_{pp} when d_{pp} is larger than 5 nm.

However, when it becomes smaller than 5 nm, the results are irregular and become more complex. Nonuniform grid was used after optimizing the calculation time. The grids in bulk area are 4 nm × 4 nm × 2 nm. 2 nm is in z direction as the gaps are vertically-oriented that need to be more precise. The grids in edge area are 1 nm × 1 nm × 1 nm. Although the grid spacing 1 nm is closed to atomic spacing, the simulation results are always converged. The irregular results may be simulation errors come from grid meshing. For one thing, the smallest grid size 1 nm × 1 nm × 1 nm is close to the 5 nm gap studied here. For another, auto-mesh generation was not used, and this kind of manual meshing would bring errors. It should be pointed out that the particle-film gap distance d_{pf} is within the plasmonic field penetration

depth, which is typical around 10 nm. If d_{pp} is adjusted to nanosize such as 5 nm, the enhancement is more than 7×10^3 times, which is enough for the single molecule SERS application.

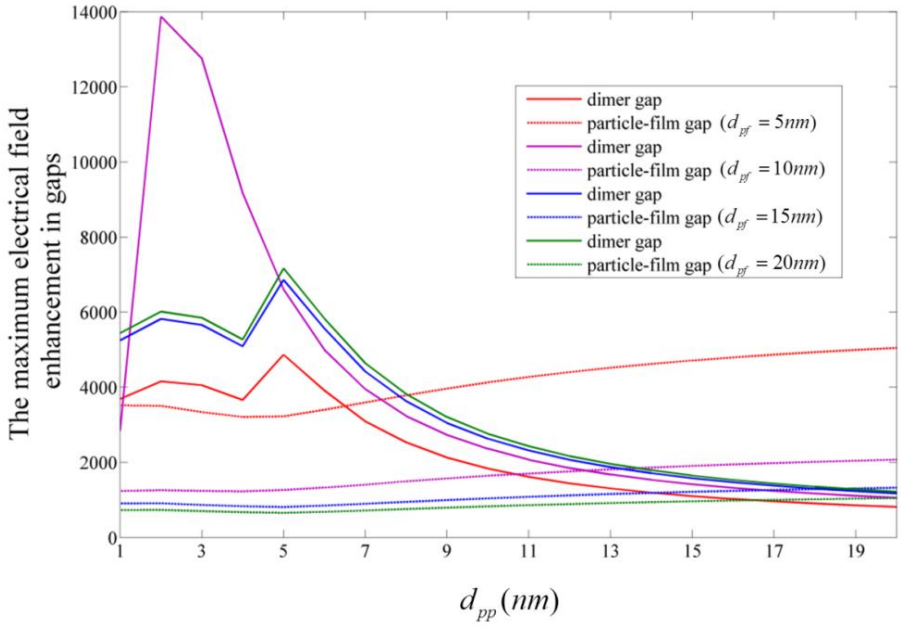

Fig. 5.15 The electric field enhancement when changing d_{pp}. The enhancement factor is obtained at the point next to the particle which will present the highest field value.

In this section, the electric field enhancement of the vertical dimer was evaluated for the SERS application. The plasmon coupling between particle and particle is relatively stronger than that between particle and film. The dimer gap being used for highly sensitive SERS detection no longer requires the sample to be at the surface of the film. The results of gap distance dependent electric field enhancement can provide instructions for practical application.

5.5 Electric field enhancement explanation

5.5.1 Plasmon hybridization of vertical dimers on metal film

In order to understand the underlying mechanism of the observed enhancement, simply physical models were proposed based on the dipole

approximation theory. As shown in Fig. 5.16(a), when the dimer is far away from the film, the dimer has little effect on the plasmonic field, thus it can be regarded as enhanced plasmonic field exciting the dimer. Although there is some decay along the z direction [Fig. 5.12(a)], the enhancement is still relatively high in the dimer gap, indicating that the LSP-LSP coupling of the particle-particle interaction is strong. This mode corresponds to the result in Fig. 5.15 when d_{pf} is more than 20 nm.

Fig. 5.16(b) is the situation of mainly SPP-LSP coupling. The dimer gap distance is large and the bottom particle is close to the film. It can be considered that the two particles are excited by the plasmonic field separately. Because of the absorption and scattering by the bottom particle, the field exerted on the top particle is weak. Thus the enhancement in the particle-film gap is stronger than that in the dimer gap when d_{pp} becomes large. This agrees with the result in Fig. 5.15.

When both the dimer gap and dimer-film gap size become close to the particle size (tens of nanometers), SPP-LSP-LSP coupling appears [Fig. 5.16(c)]. The electric field enhancement within the dimer gap comes from the absorption and scattering of the plasmonic field. The absorption is proportional to dimer effective polarizibility according to Eq. (5.18), whilst the scattering is proportional to the square of the effective polarizability of the bottom particle. The electric field enhancement in the gap between the bottom particle and the film is from the absorption and scattering by the nanoparticle with the addition of the plasmonic field. The effective polarizability of the bottom particle is only part of total dimer effective polarizability, and the original plasmonic field is relatively small compared with these plasmon hybridizations. To sum up, that is reason why the dimer gap enhancement is large in this SPP-LSP-LSP thus the proposed vertical dimer system is of advantageous over a conventional particle-film system.

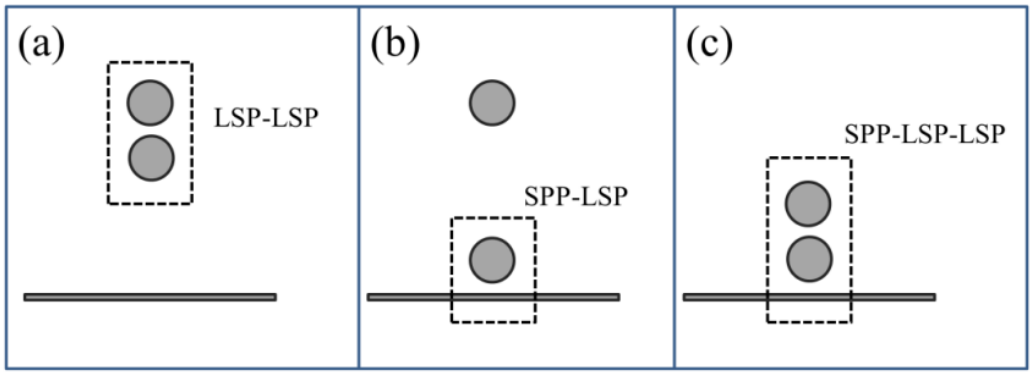

Fig. 5.16 Three plasmon hybridization modes: (a) dimer is far away from the film ($d_{pf} \gg R > d_{pp}$); (b) the dimer gap distance is large and the one sphere is close to the film ($d_{pp} \gg R > d_{pf}$); (c) dimer is close to the film ($d_{pp} \sim d_{pf} < R$).

5.5.2 Electric field line distribution of vertical dimers on a metal film

Single nanoparticle or nanoparticle dimer far away from the Ag film can be analytically analysed with dipole approximation introduced in the theory part, as they can be regarded as single nanosphere or two nanospheres in the uniform electrical excitation field. When these particles are close to the film surface, the SPPs will engage and the plasmonic field varies intensely. Fig 5.17 (a) and (b) show the electric field line distribution for a particle-film system and a particle-particle-film dimer system, respectively, using the SPP-LSP and SPP-LSP-LSP modes. In the diagram each electric field line occupies 2 nm × 2 nm gridding. In Fig. 5.17(a), the sign of the charge at the particle remains similar to a single polarized sphere [Fig. 5.3(a)]. However, since the plasmonic field decays from the surface, the electric field in the gap is stronger than that at the top. As a result, the hot-spot locates at the gap rather than at the top. As shown in Fig. 5.17(b), the electric field lines change their directions and become more concentrated at the particle-particle dimer gap due to the introduction of the new particle at the top. Thus the free

electrons at the bottom of the top particle and the top of the bottom particle will have more intense interaction than that between the bottom particle and film. That is evidence that the localized plasmon hybridization dominates in this SPP-LSP-LSP coupling. We can conclude that the vertically-oriented dimer structure within the particle-particle-film system is an effective and efficient SERS structure.

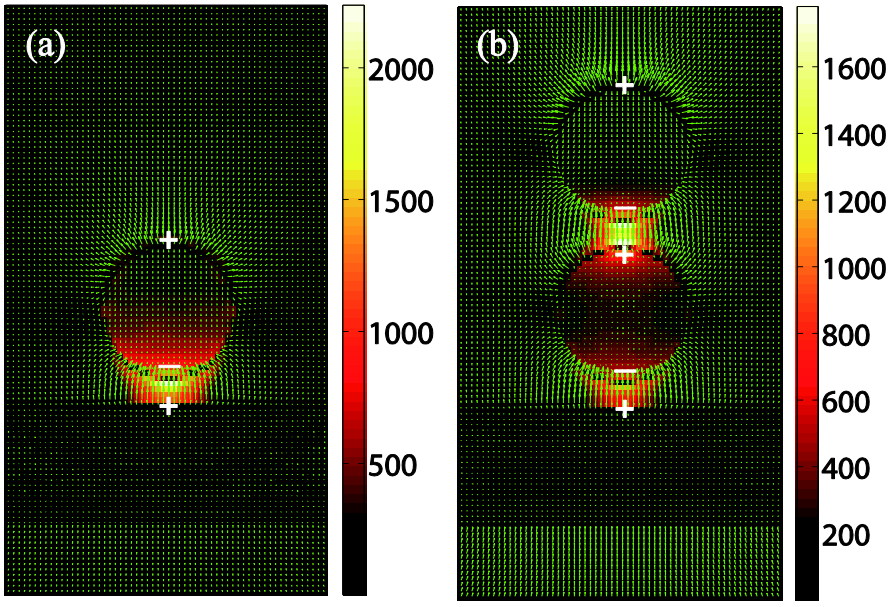

Fig. 5.17 The FDTD simulation for the electric field line distribution of (a) a gold sphere placed above a silver film ($d_{pf} = 10$ nm) and (b) gold nanosphere dimer ($d_{pp} = 10$ nm) placed above a gold film ($d_{pf} = 10$ nm). The background shows the electric field intensity.

The electric field lines distributions corresponding to the cases in the Fig. 5.13 were also calculated. The charge distributions agree well with the electric field distributions. In Fig. 5.18(a), the electric field line distribution becomes more complex, as the strongly enhanced field in the gap will significantly affect the field of the ambient environment, especially the surface of the particles. In Fig. 5.18(b), the electric field line distribution is more normal, as the electric field is mainly confined in the particle-film gap.

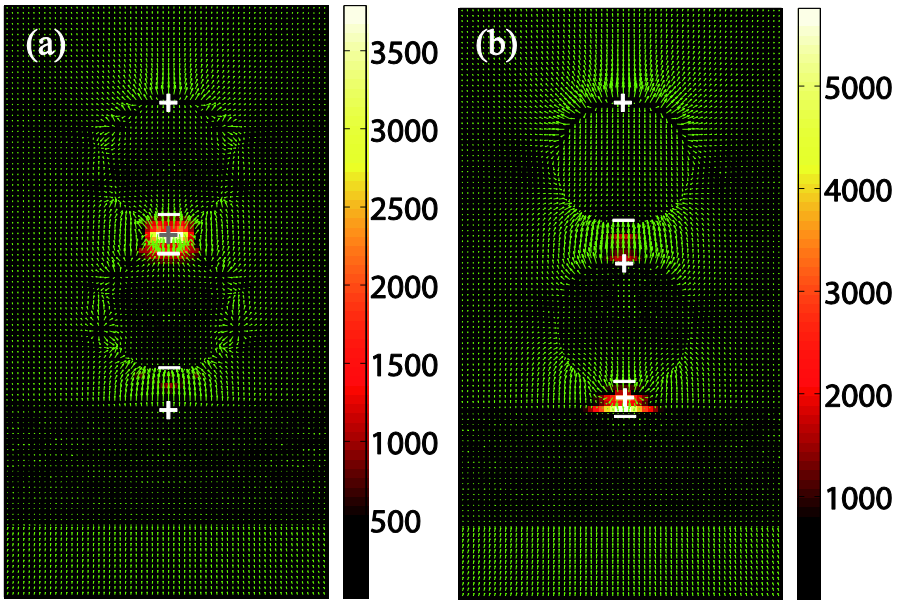

Fig. 5.18 The FDTD simulation for the electric field line distribution of (a) a gold sphere placed above a silver film ($d_{pf} = 5$ nm) and (b) gold nanosphere dimer ($d_{pp} = 10$ nm) placed above a gold film ($d_{pf} = 5$ nm). The background shows the electric field intensity.

5.6 Summary

In conclusion, a vertically-oriented particle-particle dimer structure was presented for the first time, which is suitable for highly sensitive scanning SERS application. It was firstly demonstrated that a 50 nm gold nanoparticle could be trapped by SP-VP. Further force analysis indicated that the top particle will not influence the stable trapping of the bottom particle, which verified that the proposed system is feasible.

Comparing to a horizontally-oriented dimer fabricated with complex technique, the vertically-oriented dimer easily built and it is able to do scanning for Raman imaging. Acting as the excitation field for the dimer, SP-VP is not only dominant in the longitudinal direction but also providing an enhanced field. The vertically-oriented dimer can effectively make use of the dominant longitudinal

component of the SP-VP, thus it can provide much stronger electric field in the gap which is essential for high-sensitivity (single molecule level) SERS applications.

In addition, the dipole approximation theory was used to analyse the simulation results of the gap distance dependent electric field enhancement. It was found that three main plamon coupling mechanisms exist in the vertical-dimer-metal-film system. These coupling mechanisms will pave the way for exploiting SERS imaging application with more complex structure based on the proposed vertically-oriented dimer. Finally, through the electric field line distribution, the charge distribution relating to the Coulomb force was obtained, this reveals how the particles response in the plasmonic field.

Of course, there is some limitation in this work, as fixed wavelength was used to do the calculation, which is not an optimised working wavelength. Different wavelength sources may bring different spectral responses. In particular, the resonance effects of the nanostructures are crucial for both the trapping force and the electric field enhancement. The working wavelength need to be optimised to satisfy both trapping potential and electric field enhancement, so that it can be better utilised in practical applications.

Chapter 6 Trapping and rotating a metallic particle trimer with optical vortex

6.1 Introduction

Invented by Ashkin three decades ago, optical tweezers has been widely used in manipulating objects in the micro world [88]. Rotating objects, as a special form of object manipulation, has been studied intensively because it could have a range of applications such as biological cell orientation [170], photonics devices [171], optical spanner [99, 172, 173] and micro-rotor [174-179].

Generally, torque induced by angular momentum of light can be used to rotate an object, and it has two distinct forms: Spin Angular Momentum (SAM) [180] and Orbital Angular Momentum (OAM) [181]. SAM is associated with circular polarization. Each photon in a circularly polarized light carries a basic unit of SAM $\pm\hbar$. The sign of the SAM depends on whether the light is left or right circularly polarized [182]. OAM is associated with helical wavefront. Beam with helical phase $\varphi = l\phi$ (l is positive or negative topological charge and ϕ is the polar angle) possesses well-defined OAM with $l\hbar$ [181].

SAM rotation has been applied to birefringence materials [183-185], irregular objects [176, 186, 187], turbine type structures [175, 178, 188] and non-uniform coated spheres [179]. However, the torque changes with the orientation of the objects. In addition, the photothermal effect and photodamage are challenges for high absorption objects and biological samples [189]. OAM provides an alternative method for optical rotation of particles without special requirement of the shape and/or material composition of particles.

Optical vortex is a typical beam that possesses OAM [172, 190]. Compared with laser beam being focused directly to the particle, optical vortex with doughnut-shaped intensity distribution leads to less instant heating and photodamage because of its relatively large illumination area [189]. Therefore, optical vortex is an attractive candidate for trapping and rotating particles.

Trapping and rotation of metallic particles with optical vortex have indeed attracted much attention. Zhao *et al* demonstrated the rotation of three individual metallic particles by using strongly focused circularly polarized Laguerre-Gaussian beam [100]. K. Dholakia's group reported the trapping and rotation of two individual nanoparticles in the dark core of optical vortex [101, 191]. The rotation of single metallic particle on a metal-thin-film with plasmonic vortex has been previously demonstrated [147].

However, in all previous studies the rotation of metallic particles is not steady in terms of rotation path and speed. In addition, the trapped metallic particles in the experiments of all previous studies were individual particles rather than an integrated system, which is highly desirable for practical applications such as micro-rotor. Furthermore, as for theoretical analysis, previous work only studied the force of dielectric particle in optical vortex and there is no detailed quantitative analysis of the force of metallic particle in optical vortex.

In this chapter, the first stable trapping and steady rotation of a metallic particle trimer with optical vortex was experimentally demonstrated [35]. 3D electric field distribution of a focused radially polarized optical vortex beam has been derived and calculated, by using angular spectrum representation and Richards-Wolf vectorial diffraction theory [143, 144]. Through morphological analysis, It was found that the metallic particles are confined within the maximum intensity ring of

the focused field. Moreover, in order to investigate the mechanism of the interaction between metallic particle and optical vortex, FDTD simulation and MST method were used for quantitative force analysis.

6.2 Experimental trapping and rotating mesoscopic particles

Fig. 6.1 shows the schematic diagram of experimental setup. After passing through a half-waveplate and a quarter-waveplate, the 1064 nm Nd:YAG laser beam was converted to a circularly polarized beam. The spiral phase plate was used to give a helical wavefront to the beam. In a full cycle, the spiral phase plate with topological charge of 1 can introduce $0 \sim 2\pi$ phase change to the beam with its continuously increasing step thickness. The step thickness is typical in the order of the laser wavelength. The obtained circularly polarized optical vortex was finally focused to the sample on glass slide by using an oil immersion objective with NA=1.49. Particles were suspended in deionized water. The incident laser power is about 100 mW. The sample of particles solution was held in a homemade circular well to minimize the motion of water. The well was fabricated on an electric insulating tape by laser direct writing technique. Note that the use of insulation tape is not essential; any other waterproof material of thickness 100~200 micrometers can be used here. The CCD camera (Point Grey Chameleon CMLN-13S2M) was used to record the movement of the particles, which are illuminated by a white light source. Since the dichroic mirror has a high transmission coefficient but a low reflection coefficient at 1064 nm, most of the reflected 1064 nm beam will not be collected on the CCD camera. Nevertheless a band-stop infrared filter was further used to prevent the remaining 1064 nm stray light from entering into the CCD camera.

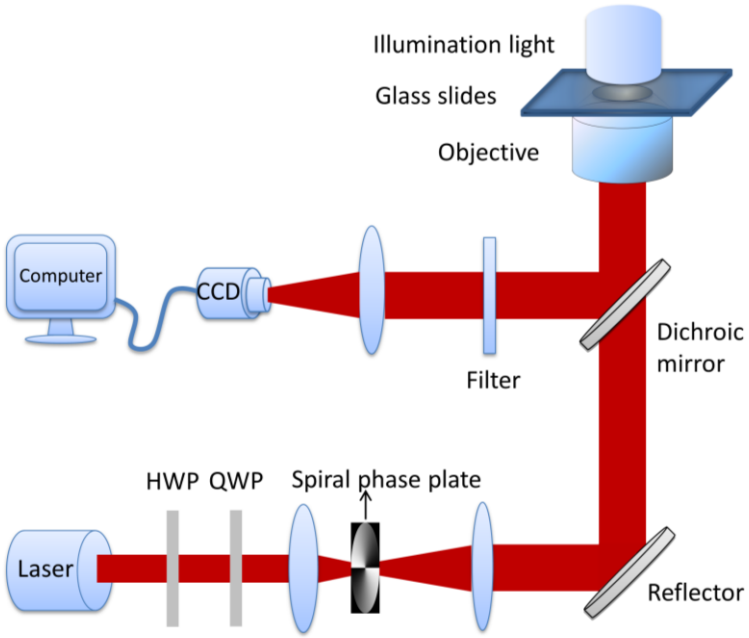

Fig. 6.1 Optical tweezers system with focused circularly polarized optical vortex. The incident wavelength is 1064 nm. The incident laser power is about 100 mW. HWP: half-waveplate. QWP: quarter-waveplate. The topological charge of the spiral phase plate is 1. The NA of the oil immersion objective lens is 1.49. The illumination light represents a white light source.

6.2.1 Trapping and rotating a gold particle trimer

The optical tweezers experiment was performed using 0.8~1.5 μm diameter gold particles (ALFA AESAR). A subset of identical sized particles with diameter around 1 μm was used in experiments. The gold particles will not be trapped automatically by the focused optical vortex because of the repulsion force from the bright ring of the focused optical vortex. Following six steps were used in order to achieve stable trapping of a gold particle trimer. (1) The spiral phase plate in the experimental setup (Fig. 6.1) was removed. The focused optical vortex now became a conventional focused beam. (2) The focused circularly polarized beam was then used to push/move selected gold particles to a desired position. (3) In total three gold particles were moved to the same position and they were placed close to each other by repeating step-2. (4) The laser was then switched off, and the three particles

would not diffuse away in a short time. (5) A motorised stage was used to move the sample plate so that the center position of the three gold particles was at the focus position of the optical beam. (6) Finally, the spiral phase plate was reloaded and the laser beam was re-launched. The three gold particles were automatically pushed together into the center of the focused optical vortex. The gold particle trimer was now trapped stably inside the bright ring of the focused optical vortex where they started rotating.

Note that this experiment has been repeated more than 3 times and stable trapping and rotation of metallic particle trimers can always be reproduced using the five-step experimental procedure. Typical results are shown in Fig. 6.2 where three gold particles with similar size were trapped. It was found that the speed of the rotation could vary because of the variation of the gold particle size (0.8~1.5 μm).

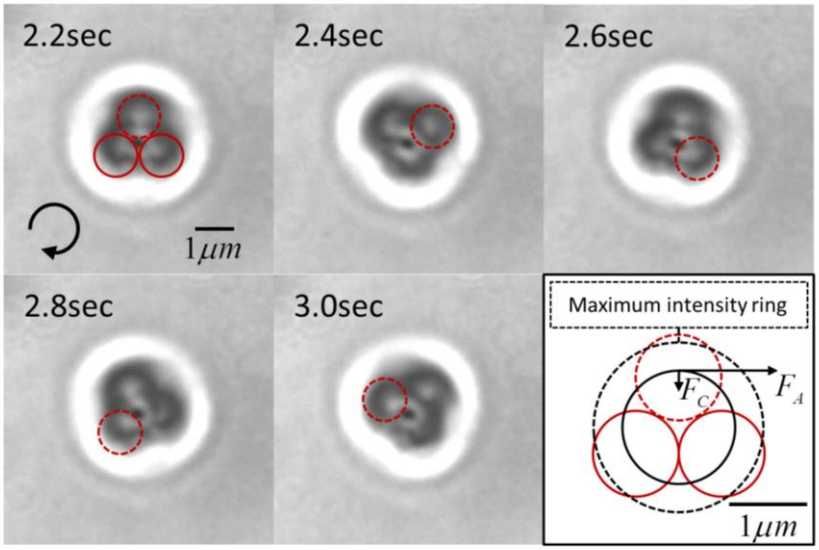

Fig. 6.2 Successive frames of a video recording that show the movement of gold particle trimer in the focused circularly polarized optical vortex. The time interval is 0.2 s. The gold particle in the red dotted circle is to indicate the rotation, which is clockwise. The panel at the bottom right corner shows the force analysis graph. The dotted circle indicates the maximum intensity ring. The solid circle indicates the rotation path of gold particles. F_A and F_c is the angular force and centripetal force of the dotted circle indicating particle, respectively.

The number of the gold particles trapped stably here is three, as the size of gold particle trimer matches the size of the bright ring of the focused optical vortex (with topological charge 1). If the laser is switched off, the trapped and rotated gold particle trimer will not be able to continue rotating. Rather the gold particles will follow a centrifugal motion afterwards, and the gold particle trimer will eventually break apart because the optical force no longer exists. The three gold particles will return to Brownian movements, and they will diffuse away.

Gold particles rotate approximately 21 cycles in 20 seconds (Fig. 6.2), so their angular velocity is $21\times 2\,\pi/20\,\mathrm{s}\approx 6.6\,\mathrm{rad/s}$. Since the trimer particles are touching each other and the diameter of each particle is around 1.15 μm, their radius of rotation is $1.15/\sqrt{3}\,\mu\mathrm{m}\approx 0.664\,\mu\mathrm{m}$. The volume of the gold particle is 7.96×10^{-19} m^3 and the mass of each particle is 1.54×10^{-14} kg, assuming that the mass density of gold is 19320 $\mathrm{kg/m}^3$. According to Newton's second law of motion ($F_c = mr\omega^2$), we can calculate the centripetal force F_c of gold particles to be 4.45×10^{-19} N. The angular force F_A of gold particles experienced in this experiment approximately equals to the hydrodynamic drag force, which is influenced by both the interaction between particles and the wall effect [192].

Here a simplified model was used where the trimer was treated as three isolated particles thus only the effect of wall (e.g. glass slide substrate) on a rotating particle was considered to estimate the hydrodynamic drag force. Under these assumptions, we can get the following equation according to Stokes's law with the Faxen correction to fifth order [193],

$$F = \mu_{drag} v = 6\pi\eta R v\left\{[1-\frac{9}{16}\frac{R}{h}+\frac{1}{8}(\frac{R}{h})^3-\frac{45}{256}(\frac{R}{h})^4-\frac{1}{16}(\frac{R}{h})^5]^{-1}\right\} \qquad (6.1)$$

where μ_{drag} is the drag coefficient, v is the linear velocity and R is the particle radius. The viscous coefficient η in water is about 8.9×10^{-4} Pa·s at $25\,^{o}C$. h is the distance between the center of trapped particle and the glass slide. Therefore, the angular force F_A of gold particles can be calculated as about 4.37×10^{-14} N, assuming $h=10\,\mu$m, as the geometric focal plane is located at about 10 μm distance from the glass-water interface. It should be pointed out that a complex model considering both particle-particle and particle-wall interactions is necessary in order to precisely calculate the hydrodynamic drag force related to the rotation of the particle trimer.

In addition, the torque of a rotating particle can be calculated using the following equation in the paraxial limit [181, 194],

$$\mu_{drag} vr = \tau = \frac{\alpha p}{\omega}(l+\sigma_z) \tag{6.2}$$

where r is the rotation radius, τ is the torque of a rotating particle, α is the absorption coefficient, p is the incident laser power, ω is the frequency of the light, l is the topological charge, $\sigma_z = \mp 1$ for right- or left- handed circularly polarized light and $\sigma_z = 0$ for linearly polarized light. The rotation speed v of the metallic particle trimer is proportional to the incident power, thus the rotation speed of the metallic particle trimer can be controlled by adjusting the laser power.

Note that the topological charge of the spiral phase plate used here is 1. Higher topological charge could also be used but this would lead to a larger rotation radius, as shown in Eq. (6.2). Higher topological charge would thus be more suitable for trapping and rotating larger size metallic particles.

6.2.2 Trapping and rotating a silica particle tetramer

The optical trapping and rotation of 1 μm silica particles were also investigated using the same experimental system. In contrast to gold particles, silica particles can be automatically trapped to the bright ring of the focused optical vortex when the particle is close to the ring. By moving the motorised stage, up to four silica particles can be trapped near the bright ring of the focused optical vortex, forming a silica particle tetramer that starts rotating spontaneously. The number of the silica particles trapped here is four since the size of silica particle tetramer matches the size of the ring of the focused optical vortex (with topological charge 1). Following this experimental procedure, this experiment has been repeated more than 3 times. Similar experimental result as those shown in Fig. 6.3 could consistently be reproduced.

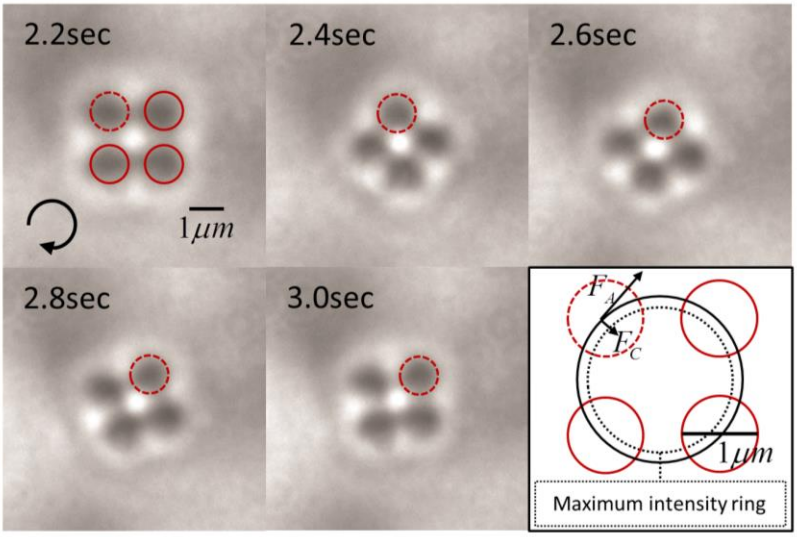

Fig. 6.3 Successive frames of a video recording that show the movement of a silica particle tetramer in the focused circularly polarized optical vortex. The time interval is 0.2 s. One of the silica particles is dotted to indicate the rotation, which is clockwise. The panel at the bottom right corner shows the force analysis graph. Note that the particles in this sketch may not be equally spaced. The dotted circle indicates maximum intensity ring. The solid circle indicates the rotation path of silica particles. F_A and F_c is the angular force and centripetal force of the dotted circle indicated particle, respectively.

Silica particles rotate at a much slower pace of approximately 4 cycles in 15 s (Fig. 6.3), corresponding to an angular velocity of $4\times 2\pi/15\,\mathrm{s}\approx 1.68\,\mathrm{rad/s}$. The radius of rotation is about 1 μm, which is larger than the rotation radius of 0.667 μm for a gold trimer. Given that the density of silica particle is $2650\,\mathrm{kg/m^3}$, the centripetal force and angular force of silica particle can be calculated to be about 3.89×10^{-21} N and 1.02×10^{-14} N, respectively.

The centripetal force of a dielectric particle is mainly due to the varying gradient of the intensity of a focused optical vortex in the radial direction. The gradient force of a dielectric particle can be expressed in terms of its polarizability α and the gradient of the electric field intensity as

$$F_{grad} = -(1/2)n\alpha\nabla E^2 \tag{6.3}$$

where *n* is the refractive index of water where the particle is suspended [88]. As shown in the bottom-right panel of Fig. 6.3, the centers of the silica particles are slightly outside the maximum intensity ring, indicating that the direction of the gradient force is towards the center, thus providing the centripetal force for the rotation.

The rotation status relies on the forces exerted on the particles. The angular force is 1.02×10^{-14} N and 4.37×10^{-14} N for the silica particle and the gold particle, respectively. Because of the smaller angular force, the silica particle tetramer rotates at a slower speed than the metallic trimer. This agrees with the experimental observations. The centripetal force is 3.89×10^{-21} N and 4.45×10^{-19} N for the silica particle and gold particles, respectively. For silica particles, the thermal motion will slightly change the particle position related to the bright ring in radical direction. This will cause changes to the gradient force on the silica particles, leading to a fluctuating centripetal force.

Furthermore, as the gradient force is associated with the field intensity distribution, the bright ring of the focused beam may not be uniform and this will cause change of the gradient force, leading to additional fluctuation of the centripetal force. Therefore, the rotation of silica particles is not steady because of the change of the centripetal force. In contrast, the gold particles are more strongly trapped because of the much larger angular force and centripetal force. In addition, all three gold particle are trapped inside the bright ring of the focused optical vortex, the rotation will thus not be affected by the non-uniform field distribution of the bright ring, making the rotation of metallic particles trimer steadier. Therefore, the rotation of the metallic particle trimer is not only faster but also steadier than that of the dielectric particles.

In addition, the rotation speed of the gold particle trimer can be controlled by the incident light power (Eq. 6.2). Therefore the metallic particle trimer rotation system is a better candidate for micro-rotor application.

6.3 Circularly polarized optical vortex

6.3.1 Calculation method for the focused optical vortex field

Having obtained the experimental parameters in the metallic particles rotation, here we will perform theoretical estimation of the particle position/trajectory. Following the theory established by Richards and Wolf [144], the angular spectrum representation of the focal field in the spherical coordinates can be expressed as follows [143]:

$$\mathbf{E}(\rho,\varphi,z)=\frac{ikfe^{-ikf}}{2\pi}\int_0^{\theta_{\max}}\int_0^{2\pi}\mathbf{E}_\infty(\theta,\phi)e^{ikz\cos\theta}e^{ik\rho\sin\theta\cos(\phi-\varphi)}\sin\theta d\phi d\theta \qquad (6.4)$$

where ρ is the distance from the excitation point, φ is the angle with respect to the polarization direction, z is the distance to the focal plane, f is the radius of Gaussian reference sphere for the incident beam, k is the propagating wave vector.

A circularly polarized vortex beam is a circularly polarized beam with a spiral phase wavefront. In a Cartesian coordinates system, a left-hand circular (LHC) polarized beam with a planar wavefront can be expressed as

$$\mathbf{E}_{LHC} = (\mathbf{n}_x + i\mathbf{n}_y)/\sqrt{2} \tag{6.5}$$

Assume the transmission coefficients for s- and p- polarizations are both 1. If the incident beam is in x polarization (i.e. $\mathbf{E}_{inc} = E_{inc}\mathbf{n}_x$),

$$\begin{aligned}\mathbf{E}_\infty(\theta,\phi) &= E_{inc}(\theta,\phi)[\cos\phi\mathbf{n}_\theta - \sin\phi\mathbf{n}_\phi]\sqrt{n_1/n_2}(\cos\theta)^{1/2} \\ &= E_{inc}(\theta,\phi)\frac{1}{2}\begin{bmatrix}(1+\cos\theta)-(1-\cos\theta)\cos 2\phi \\ -(1-\cos\theta)\sin 2\phi \\ -2\cos\phi\sin\theta\end{bmatrix}\sqrt{n_1/n_2}(\cos\theta)^{1/2}\end{aligned} \tag{6.6}$$

where n_1 and n_2 are respectively the refractive indices of matching oil and water.

For y polarization (i.e. $\mathbf{E}_{inc} = E_{inc}\mathbf{n}_y$), is the incident electric field

$$\begin{aligned}\mathbf{E}_\infty(\theta,\phi) &= E_{inc}(\theta,\phi)[\cos\phi\mathbf{n}_\phi + \sin\phi\mathbf{n}_\theta]\sqrt{n_1/n_2}(\cos\theta)^{1/2} \\ &= E_{inc}(\theta,\phi)\begin{bmatrix}\sin\phi\cos\phi(\cos\theta-1) \\ \cos^2\phi+\sin^2\phi\cos\theta \\ -\sin\phi\sin\theta\end{bmatrix}\sqrt{n_1/n_2}(\cos\theta)^{1/2}\end{aligned} \tag{6.7}$$

For a left-hand circularly polarized beam

$$\mathbf{E}_\infty(\theta,\phi) = \frac{1}{\sqrt{2}}E_{inc}(\theta,\phi)\begin{bmatrix}\frac{1}{2}[(1+\cos\theta)-(1-\cos\theta)\cos 2\phi]+i\frac{1}{2}\sin 2\phi(\cos\theta-1) \\ \frac{1}{2}\sin 2\phi(\cos\theta-1)+i[\cos\theta+\frac{1}{2}(1+\cos 2\phi)(1-\cos\theta)] \\ -\sin\theta e^{i\phi}\end{bmatrix}\sqrt{n_1/n_2}(\cos\theta)^{1/2} \tag{6.8}$$

Considering the spiral phase factor $\exp(il\phi)$, where l is the topological charge of the optical vortex.

$$\mathbf{E}(\rho,\varphi,z)=\begin{bmatrix}E_x\\E_y\\E_z\end{bmatrix}=\frac{ikfe^{-ikf}}{2\pi}\int_0^{\theta_{\max}}\int_0^{2\pi}E_0\exp(-\frac{f^2\sin^2\theta}{w^2})\exp(il\phi)\sqrt{\frac{n_1}{n_2}}\sqrt{\cos\theta}e^{ikz\cos\theta}e^{ik\rho\sin\theta\cos(\phi-\varphi)}\sin\theta$$
$$\times\frac{1}{\sqrt{2}}\begin{bmatrix}\frac{1}{2}[(1+\cos\theta)-(1-\cos\theta)\cos2\phi]+i\frac{1}{2}\sin2\phi(\cos\theta-1)\\\frac{1}{2}\sin2\phi(\cos\theta-1)+i[\cos\theta+\frac{1}{2}(1+\cos2\phi)(1-\cos\theta)]\\-\sin\theta e^{i\phi}\end{bmatrix}d\phi d\theta \tag{6.9}$$

where subscripts *x*, *y* and *z* represent the components in the Cartesian coordinates, E_0 is the incident electric field, $\exp(-\frac{f^2\sin^2\theta}{w^2})$ is the apodization function, where w represents the beam waist for the Gaussian beam and $f\sin\theta$ is the aperture radius of the reference lens.

Using the mathematical identity $\int_0^{2\pi}e^{in\phi}e^{ix\cos(\phi-\varphi)}=2\pi(i^n)J_n(x)e^{in\varphi}$, where $J_n(x)$ is the n^{th} order Bessel function of the first kind.

$$E_x(\rho,\varphi,z)=-\frac{1}{2\sqrt{2}}ikfe^{-ikf}\int_0^{\theta_{\max}}E_0\exp(-\frac{f^2\sin^2\theta}{w^2})\sqrt{\frac{n_1}{n_2}}\sin\theta\sqrt{\cos\theta}e^{ikz\cos\theta}i^l$$
$$\times[(1+\cos\theta)e^{il\varphi}J_l(k\rho\sin\theta)+(1-\cos\theta)e^{i(l+2)\varphi}J_{(l+2)}(k\rho\sin\theta)]d\theta \tag{6.10}$$

$$E_y(\rho,\varphi,z)=-\frac{1}{2\sqrt{2}}ikfe^{-ikf}\int_0^{\theta_{\max}}E_0\exp(-\frac{f^2\sin^2\theta}{w^2})\sqrt{\frac{n_1}{n_2}}\sin\theta\sqrt{\cos\theta}e^{ikz\cos\theta}i^{l+1}$$
$$\times[(1+\cos\theta)e^{il\varphi}J_l(k\rho\sin\theta)+(1-\cos\theta)e^{i(l+2)\varphi}J_{(l+2)}(k\rho\sin\theta)]d\theta \tag{6.11}$$

$$E_z(\rho,\varphi,z) = -\frac{1}{\sqrt{2}} ikfe^{-ikf} e^{i(l+1)\varphi} \int_0^{\theta_{\max}} \int_0^{2\pi} E_0 \exp(-\frac{f^2 \sin^2\theta}{w^2}) \sqrt{\frac{n_1}{n_2}} \sin^2\theta \sqrt{\cos\theta} e^{ikz\cos\theta} i^{l+1} J_{l+1}(k\rho\sin\theta) d\phi d\theta \tag{6.12}$$

6.3.2 Focused circularly polarized optical vortices with different topological charges

Using the equations above, we can calculate the field distributions of the focal plane. In the calculations, n_1 and n_2 were assumed to be 1.515 and 1.33, respectively. Other parameters are same as experiment in Fig. 6.1. Figs. 6.4-6 show the electric field and intensity of tightly focused left-hand circularly polarized optical vortex with topological charges $l = 0, 1, 2$ respectively. In these figures, (a)(b)(c) represent the *x*-, *y*- and *z*- polarized components of electric field in the focal plane, respectively. (d) represents the total intensity distribution.

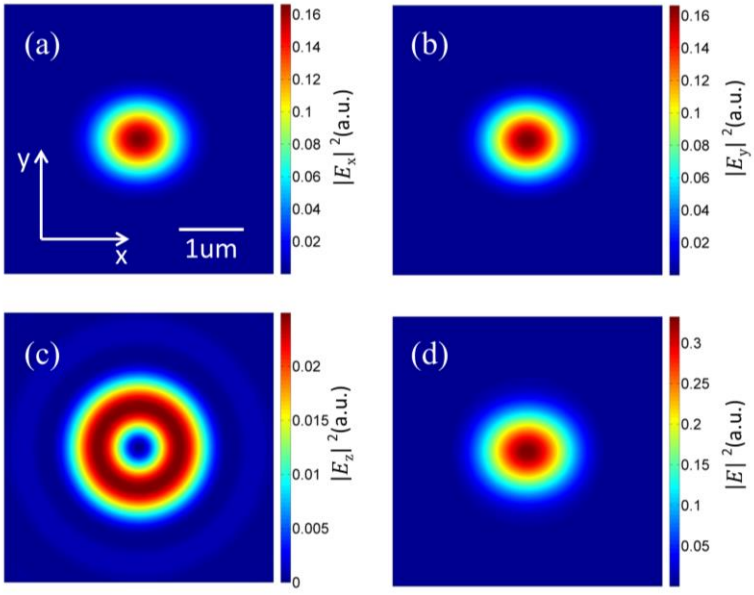

Fig. 6.4 Electric field and intensity of tightly focused left-hand circularly polarized optical vortex (topological charge $l = 0$) in the focal plane. (a) x direction component $|E_x|^2$. (b) y direction component $|E_y|^2$. (c) Longitudinal component $|E_z|^2$. (d) Total intensity $|E|^2$.

The circularly polarized optical vortex with topological charge 0 can be regarded as circularly polarized beam. As shown in Fig. 6.4, the focus center of the total electric intensity is bright, whilst that of the optical vortex with non-zero topological charge is dark.

The optical vortex with topological charge 1 was used in the experiments. As shown in Fig. 6.5, the radius of the maximum intensity ring (r_{ring}) is calculated to be about 0.76 μm, which is larger than the rotation radius of gold particles of 0.664 μm. Thus the gold particle trimer is confined within the maximum intensity ring, which is consistent with the experimental observation.

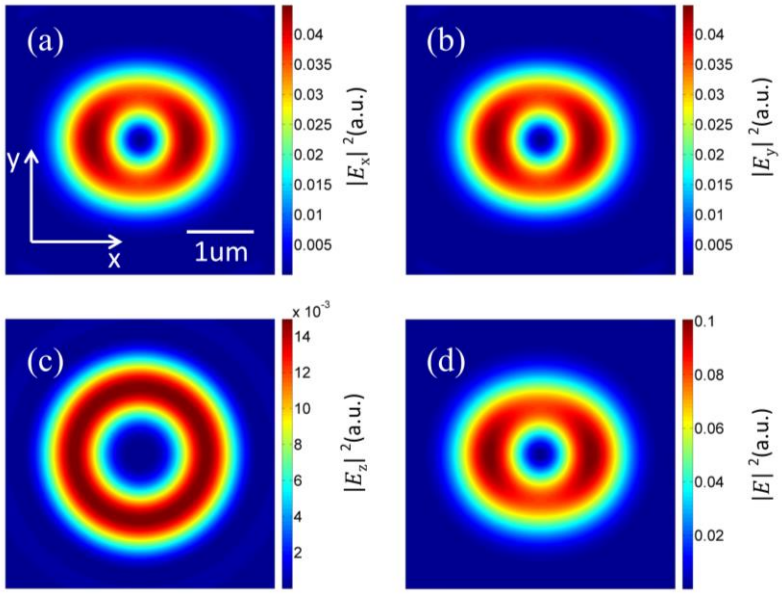

Fig. 6.5 Electric field and intensity of tightly focused left-hand circularly polarized optical vortex (topological charge $l=1$) in the focal plane. (a) x direction component $|E_x|^2$. (b) y direction component $|E_y|^2$. (c) Longitudinal component $|E_z|^2$. (d) Total intensity $|E|^2$.

As shown in Fig. 6.6, the optical vortex with topological charge 2 has larger dark core than that with topological charge 1, so the dark core of its focused field is also larger. It proves once again that the higher topological charge optical vortex is suitable for larger size metallic particle trapping.

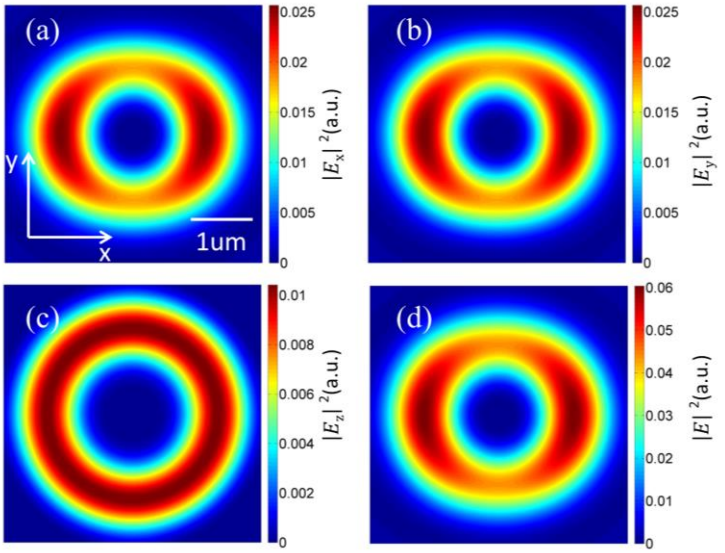

Fig. 6.6 Electric field and intensity of tightly focused left-hand circularly polarized optical vortex (topological charge $l=2$) in the focal plane. (a) x direction component $|E_x|^2$. (b) y direction component $|E_y|^2$. (c) Longitudinal component $|E_z|^2$. (d) Total intensity $|E|^2$.

6.4 Trapping and rotation mechanisms of gold particles in focused optical vortex

6.4.1 Force analysis of a gold particle in the focused optical vortex

Fig. 6.7 shows the force distributions of a gold particle at different radii in three directions, which were calculated using Eq. (3.19). The *x* direction force (F_x) represents the radial force. When the radius is less than 2.2 μm, the force is pulling the particles to the center because of the radiation pressure from the bright ring of the focused optical vortex. For the same reason, when the radius is between 2.2 μm and 4 μm, F_x is pushing the particles away from the center, as shown in Fig. 6.7(b). The y direction force (F_y) represents the angular force. The negative F_y provides the angular torque of the particle in the clockwise rotation. The *z* direction force (F_z) is always negative and it can balance the gravity, buoyancy and the force of the thermal conversion (usually from bottom to top). At the position of the rotation radius, the

radial force F_x is calculated to be 5.4×10^{-14} N, which is larger than 4.45×10^{-19} N thus the radial force can provide sufficient centripetal force for the rotation. The angular force is calculated to be about 4.3×10^{-14} N which is in the same order of magnitude to the estimated experimental angular force of 4.37×10^{-14} N.

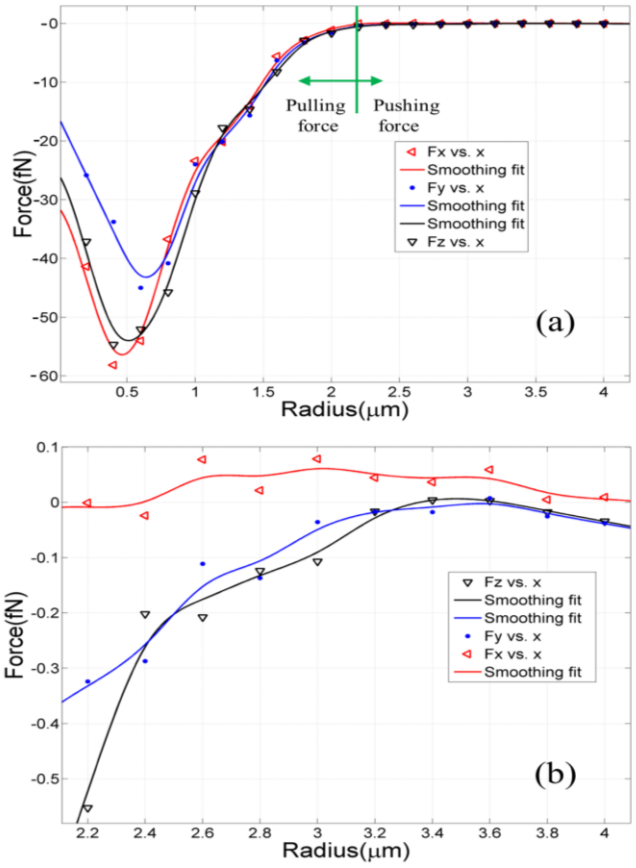

Fig. 6.7 The force distributions in *x*-, *y*- and *z*- directions of a 1 μm diameter gold particle in the focused optical vortex field. x represents the distance between particle and the focus center, which is 0~4 μm in (a) and 2.2~4 μm in (b).

6.4.2 Stability of the trapping for a gold particle in the focused optical vortex

In order to study the stability of the trapping, the trapping potential of a gold particle in the optical vortex was further calculated. Trapping potential can be calculated by the following formula [195]:

$$U(r_0) = \int_{\infty}^{r_0} \mathbf{F}(r) \cdot d\mathbf{r} \tag{6.13}$$

where $U(r_0)$ is the required energy to move the particle from the trap to infinity. Generally, in order to obtain a stable trapping, more than 10 k_BT trapping potential depth is needed to overcome the disturbance from the thermal effect [88], where k_B is the Boltzmann constant and T is the temperature. The trapping potential depth distribution was calculated as shown in Fig. 6.8. At a radius of around 1.2 μm, the trapping potential barrier is sufficient for the confinement of gold particles because the trapping potential at this position is larger than 10 k_BT. Since the largest depth of trapping potential is located at the center, the gold particles have the tendency to move towards the center. Thus all three particles were pushed towards the center of the optical vortex and form a stable gold particle trimer.

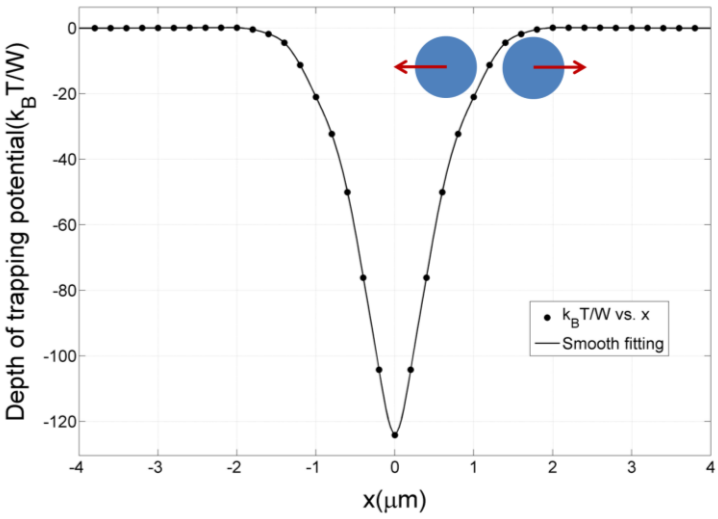

Fig. 6.8 The calculated trapping potential distribution for the gold particle along *x* direction. The blue circles indicate gold particles and the red arrows indicate the potential movement directions.

6.5 Discussion

With the analysis above, it is clear that the metallic particles and dielectric particles are trapped inside and just outside the maximum intensity ring of the optical vortex respectively. Now we can review this from another prospective, as shown in Fig. 6.9.

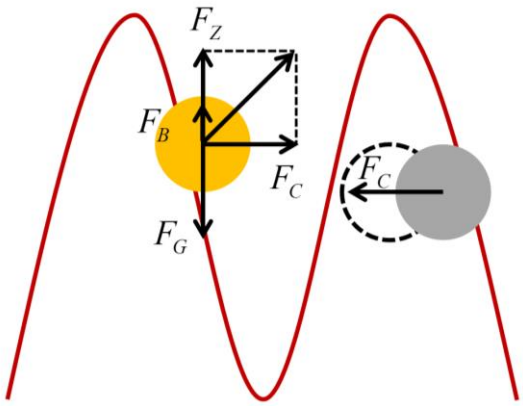

Fig. 6.9 The forces of particles on the section in x-z plane. Red curve represents the profile of the field distribution of the focused optical vortex Yellow sphere indicates the metallic particle and grey sphere indicates the dielectric particle.

The total force on the metallic particle is mainly scattering force, which is inwards. This force can be divided to F_z and F_x. F_x is responsible for the centripetal force (F_c) and F_z is responsible for balance of the particle in z direction. Because there is little refraction in the metallic particle, the metallic particle experiences a very small gradient force. The force the dielectric particle experiences in optical field is mainly gradient force, which is inwards. The lateral trapping force of the dielectric particle is responsible for its centripetal force. Because the scattering cross section of dielectric particle is much smaller than that of metallic particle, the metallic particle experiences a very small scattering force.

Metallic particles are suitable to be applied to micro-machine due to their strong stiffness. When a metallic particle trimer rotates steadily, it will lead a fluid vortex. If two metallic particle trimers rotate in clockwise and anticlockwise directions respectively, as shown in Fig 6.10, the flow of the liquid at the micro-fluidic channel is then from left to right. Therefore, the particles/samples can be transported through this micro-rotor system.

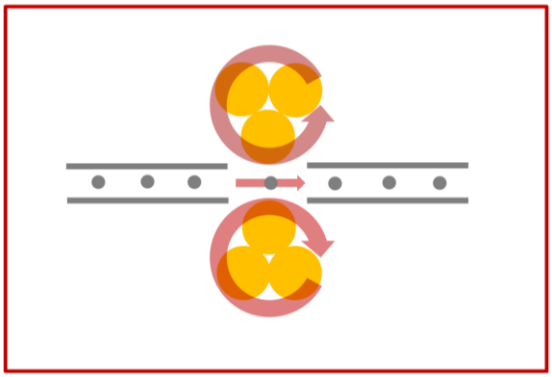

Fig. 6.10 The concept graph for the use of rotating metallic particle trimers in micro-machine.

6.6 Summary

In conclusion, the stable trapping and the steady rotation of a gold particle trimer in the tightly focused circularly polarized optical vortex was observed. The gold particles are found to be confined inside the maximum intensity ring of the focused field. The rotation of the gold particle trimer is steady at a speed of 6.6 rad/s , which can be adjusted according to the incident laser power. Different from individual metallic particles being manipulated with optical vortex reported in previous studies, a gold particle trimer reported here is trapped and rotated as an integrated system.

In addition, the experimental observation of the stable trapping and steady rotation of the gold particle trimer can be explained by quantitative theoretical modelling using vector diffraction theory and MST method. The theoretical results agree with the experimental results. It is believed that the trapping and rotation of a metallic particle trimer with optical vortex provides an alternative method for micro-rotor, which may find potential applications in micro-fluidics devices. The obtained metallic particle trimer may also be useful in SERS, where the trimer gap can be used as a hot spot for electric field enhancement.

Chapter 7 Conclusion and future work

7.1 Conclusion

In this thesis, a systematic research was performed on the optical manipulation of metallic particles. The work reported in this thesis covers the following four aspects.

1. Focused plasmonic trapping of single metallic particle

The focused plasmonic trapping of metallic particle was theoretically investigated. A SP-VP was generated on a metal film through the excitation with focused radially polarized beam. 3D FDTD simulations were performed to obtain the electric field distribution around the metallic particle in the field of the SP-VP. MST method was applied to calculate the gradient and scattering forces exerted on the metallic particle based on the simulation results.

It was found in simulation that the metallic particle can be trapped by the SP-VP. The total force of the metallic particle is the result not of a strong gradient force dominating a weak scattering force in the opposite direction, but instead of a dominant gradient force assisted by a scattering force in the same direction.

The dominant gradient force originates with the coupling between a greatly enhanced plasmonic field and LSP field of the metallic particle, whereas the unusual scattering force is due to pushes exerted through the propagation of focused SPPs.

The proposed focused plasmonic tweezers solves the problem that metallic particle is hard to trap by optical tweezers. This point has been verified by the comparison made between focused plamsonic tweezers and optical tweezers in simulation. Moreover, compared with other plasmonic tweezers based on metal microdiscs or bowtie structures, the proposed setup benefits from the excitation of

SPPs using structured light, thereby reduces the need to fabricate complex nano-sized structures. In addition, this work gives rise to SERS with the following two advantages. (1) Since a metallic particle could act as a 'sensor' for intracellular SERS detection, the trapped metallic particle above the metal film can be controlled to move inside a biological cell thus providing a scan mechanism to image the inner structure of the biological cell. (2) A particle-film gap is formed with a metallic particle being trapped above a metal film. The strong electric field enhancement in the gap is beneficial for the sensitivity of SERS detection.

2. Focused plasmonic trapping of a horizontally-oriented metallic particle dimer

The trapping and tuning of horizontally-oriented metallic particle dimers were theoretically investigated using focused plasmonic tweezers. A SP-VP pair was generated through the excitation with focused linearly-polarized beam. 3D FDTD simulations were performed to analyse the field of the SP-VP pair interacting with the gold nanoparticles. MST method was used to calculate the forces of the particles based on the simulation results. It was found in simulation that two free-standing nanoparticles, such as nanospheres or nanorods, can be trapped simultaneously by the SP-VP pair.

Also, the field of the SP-VP pair was calculated with Richards-Wolf vectorial diffraction theory and angular spectrum representation. A relation between the virtual probes spacing and the excitation wavelength was obtained. It was found that the spacing between the nanoparticles of the dimer can be tuned by changing the excitation wavelength.

This theoretical work is the first time to study the trapping and tuning of a metallic particle dimer. The gap distance of the horizontal dimer is tunable, and this

may find applications in plasmonic sensing. Besides, the dimer can have higher electric field enhancement than that of individual metallic particles, thus it is more useful for sensitive SERS detection, particularly inside biological cells.

3. Focused plasmonic trapping of a vertically-oriented dimer

A vertically-oriented dimer structure was predicted using focused plasmonic tweezers. Force distributions together with trapping potentials of the dimer particles were calculated. These theoretical results have been shown to prove the feasibility and stability of the dimer structure. The stability of the structure is sufficient to maintain strong electric field enhancement. Meanwhile, the employed SP-VP provides further electric field enhancement in the vertical dimer gap, because the vertical dimer can effectively make use of the longitudinal component in the incident field.

The coupling mechanisms for the electric field enhancement have been explained with simply physical model (particle-particle-film system) based on simplified dipole approximation. These mechanisms have been confirmed with the charge distributions in the particle-particle-film systems.

This work mainly contributes to the SERS application with the following two advantages. (1) Compared to horizontally-oriented dimer structures such as nanorods antenna and bow-tie nanostructures, the vertically-oriented dimer has the capability of scanning. (2) Compared to the particle-film system, the vertical dimer system can make the SERS measurement of the sample without the need for a metal surface.

4. Optical trapping and rotation of a metallic particle trimer

The trapping and rotation of a gold particle trimer and a silica particle tetramer in a focused circularly polarized optical vortex were experimentally observed. It was found in experiment that the rotation of the metallic particle trimer

is not only steadier but also faster as compared with the rotation of dielectric particles tetramer.

The experimental observation of the stable trapping and steady rotation of the metallic particle trimer can be well explained by quantitative force analysis. It was found that a large proportion of the radial scattering force pushes the metallic particles together, whilst the remaining portion provides the centripetal force necessary for the rotation.

Different from individual metallic particles being manipulated with optical vortex reported in previous studies, multiple particles are trapped and rotated as an integrated system in this work. The trapping and rotation of a metallic particle trimer in optical vortex provides an alternative method for micro-rotor. In addition, the combination of manipulation of a metallic particle trimer and SERS with the trimer gap may evolve new exciting detection/measurement technology.

7.2 Future work

It is believed that there are several avenues for future research based on the work in this thesis. There is much more further work that can be done to further optimise the results, as well as levitate the use of the proposed schemes to greater heights. The following are some specific challenges to be addressed and improvements that could be undertaken in order to further the work in this thesis:

- **Experiments for focused plasmonic trapping of metallic particle dimers**

  The work on focused plasmonic trapping of horizontally- and vertically- oriented metallic particle dimer lack experimental verifications. If there is opportunity, the experiments can be fulfilled based on the theoretical work in Chapter 4 and Chapter 5.

- **Dynamic manipulation of SPPs with structured light and metal structures**

  It is mentioned that RPB and linearly polarized beam were used to generate SP-VP and SP-VP pair, respectively. These two beams are only few of many options in this area. Structured light can be used to dynamically manipulate SPPs. Also, metal structures can also be used to manipulate SPPs. The combination of using structured light and metal structure will give rise to more options for the manipulation of SPPs.

- **Biosensing by the structures of metallic particles trapped on metal film**

  Single wavelength was only considered in focused plasmonic tweezers system. Actually, the SERS structures should have spectrum responses with different wavelengths. Different sizes of metallic particles and gap distance can lead to different surface plasmon resonances. The spectrum response could also be sensitive to refractive index change of the ambient environment. Therefore, the SERS structures can be used for biosensing.

- **Trapped metallic particles for highly sensitive Raman detection**

  Both the gap between the trapped single metallic nanoparticle and metal film and the gaps between the trapped horizontally- and vertically- oriented dimer can be regarded as hot-spots for highly sensitive Raman detection. These structures can also be used for intracellular detection, as shown in Fig. 7.1. The proposed system is based on surface plasmon coupled emission (SPCE) detection. When the Raman signal couples back through the gold film, the Raman signal can be collected at the back focal plane of the objective. Since the movement of gold particle can be controlled, a scanning of gold particle inside the cell can be performed. Therefore, full cell Raman detection can be achieved.

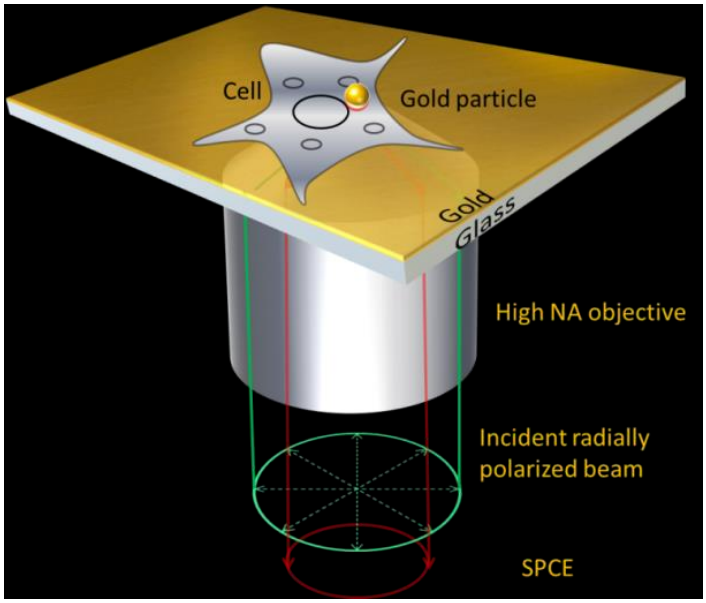

Fig. 7.1 The trapped gold particle for cell detection.

- **Photonics devices constructing by focused plasmonic tweezers**

  Focused plasmonic tweezers technique has been proven to have the capability to trap metallic nanowire [140] or semiconductor nanowire [196]. Thus it can be used for constructing photonics devices by moving the nanowires, and then the functions of these photonics devices can be further exploited.

References

1. M. C. Daniel, and D. Astruc, "Gold nanoparticles: assembly, supramolecular chemistry, quantum-size-related properties, and applications toward biology, catalysis, and nanotechnology," Chem Rev **104**, 293-346 (2004).
2. S. Eustis, and M. A. El-Sayed, "Why gold nanoparticles are more precious than pretty gold: Noble metal surface plasmon resonance and its enhancement of the radiative and nonradiative properties of nanocrystals of different shapes," Chem Soc Rev **35**, 209-217 (2006).
3. X. H. Huang, P. K. Jain, I. H. El-Sayed, and M. A. El-Sayed, "Gold nanoparticles: interesting optical properties and recent applications in cancer diagnostic and therapy," Nanomedicine **2**, 681-693 (2007).
4. R. A. Sperling, P. Rivera Gil, F. Zhang, M. Zanella, and W. J. Parak, "Biological applications of gold nanoparticles," Chem Soc Rev **37**, 1896-1908 (2008).
5. E. Boisselier, and D. Astruc, "Gold nanoparticles in nanomedicine: preparations, imaging, diagnostics, therapies and toxicity," Chem Soc Rev **38**, 1759-1782 (2009).
6. D. A. Giljohann, D. S. Seferos, W. L. Daniel, M. D. Massich, P. C. Patel, and C. A. Mirkin, "Gold nanoparticles for biology and medicine," Angewandte Chemie **49**, 3280-3294 (2010).
7. L. Dykman, and N. Khlebtsov, "Gold nanoparticles in biomedical applications: recent advances and perspectives," Chem Soc Rev **41**, 2256-2282 (2012).
8. K. Saha, S. S. Agasti, C. Kim, X. N. Li, and V. M. Rotello, "Gold Nanoparticles in Chemical and Biological Sensing," Chem Rev **112**, 2739-2779 (2012).
9. J. F. Hainfeld, D. N. Slatkin, and H. M. Smilowitz, "The use of gold nanoparticles to enhance radiotherapy in mice," Phys Med Biol **49**, N309-N315 (2004).

10. O. C. Farokhzad, J. J. Cheng, B. A. Teply, I. Sherifi, S. Jon, P. W. Kantoff, J. P. Richie, and R. Langer, "Targeted nanoparticle-aptamer bioconjugates for cancer chemotherapy in vivo," P Natl Acad Sci USA **103**, 6315-6320 (2006).

11. X. H. Huang, I. H. El-Sayed, W. Qian, and M. A. El-Sayed, "Cancer cell imaging and photothermal therapy in the near-infrared region by using gold nanorods," J Am Chem Soc **128**, 2115-2120 (2006).

12. D. Peer, J. M. Karp, S. Hong, O. C. FaroKHzad, R. Margalit, and R. Langer, "Nanocarriers as an emerging platform for cancer therapy," Nat Nanotechnol **2**, 751-760 (2007).

13. X. H. Huang, P. K. Jain, I. H. El-Sayed, and M. A. El-Sayed, "Plasmonic photothermal therapy (PPTT) using gold nanoparticles," Laser Med Sci **23**, 217-228 (2008).

14. M. Wang, and M. Thanou, "Targeting nanoparticles to cancer," Pharmacol Res **62**, 90-99 (2010).

15. G. F. Paciotti, L. Myer, D. Weinreich, D. Goia, N. Pavel, R. E. McLaughlin, and L. Tamarkin, "Colloidal gold: A novel nanoparticle vector for tumor directed drug delivery," Drug Deliv **11**, 169-183 (2004).

16. W. H. De Jong, and P. J. Borm, "Drug delivery and nanoparticles:applications and hazards," Int J Nanomedicine **3**, 133-149 (2008).

17. Y. Malam, M. Loizidou, and A. M. Seifalian, "Liposomes and nanoparticles: nanosized vehicles for drug delivery in cancer," Trends Pharmacol Sci **30**, 592-599 (2009).

18. Y. W. C. Cao, R. C. Jin, and C. A. Mirkin, "Nanoparticles with Raman spectroscopic fingerprints for DNA and RNA detection," Science **297**, 1536-1540 (2002).

19. K. Kneipp, A. S. Haka, H. Kneipp, K. Badizadegan, N. Yoshizawa, C. Boone, K. E. Shafer-Peltier, J. T. Motz, R. R. Dasari, and M. S. Feld, "Surface-enhanced Raman Spectroscopy in single living cells using gold nanoparticles," Appl Spectrosc **56**, 150-154 (2002).

20. J. Ando, K. Fujita, N. I. Smith, and S. Kawata, "Dynamic SERS imaging of cellular transport pathways with endocytosed gold nanoparticles," Nano Lett **11**, 5344-5348 (2011).

21. M. Righini, G. Volpe, C. Girard, D. Petrov, and R. Quidant, "Surface plasmon optical tweezers: tunable optical manipulation in the femtonewton range," Phys Rev Lett **100**, 186804 (2008).

22. W. Zhang, L. Huang, C. Santschi, and O. J. Martin, "Trapping and sensing 10 nm metal nanoparticles using plasmonic dipole antennas," Nano Lett **10**, 1006-1011 (2010).

23. K. Wang, E. Schonbrun, P. Steinvurzel, and K. B. Crozier, "Trapping and rotating nanoparticles using a plasmonic nano-tweezer with an integrated heat sink," Nat Commun **2**, 469 (2011).

24. C. J. Min, Z. Shen, J. F. Shen, Y. Q. Zhang, H. Fang, G. H. Yuan, L. P. Du, S. W. Zhu, T. Lei, and X. C. Yuan, "Focused plasmonic trapping of metallic particles," Nat Commun **4**, 2891 (2013).

25. E. Hao, and G. C. Schatz, "Electromagnetic fields around silver nanoparticles and dimers," J Chem Phys **120**, 357-366 (2004).

26. C. Oubre, and P. Nordlander, "Finite-difference time-domain studies of the optical properties of nanoshell dimers," J Phys Chem B **109**, 10042-10051 (2005).

27. A. Polemi, and K. L. Shuford, "Distance dependent quenching effect in nanoparticle dimers," J Chem Phys **136**, 184703 (2012).

28. J. Mertens, A. L. Eiden, D. O. Sigle, F. M. Huang, A. Lombardo, Z. P. Sun, R. S. Sundaram, A. Colli, C. Tserkezis, J. Aizpurua, S. Milana, A. C. Ferrari, and J. J. Baumberg, "Controlling Subnanometer Gaps in Plasmonic Dimers Using Graphene," Nano Lett **13**, 5033-5038 (2013).

29. P. Kuhler, E. M. Roller, R. Schreiber, T. Liedl, T. Lohmuller, and J. Feldmann, "Plasmonic DNA-Origami Nanoantennas for Surface-Enhanced Raman Spectroscopy," Nano Lett **14**, 2914-2919 (2014).

30. M. Fruhnert, F. Kretschmer, R. Geiss, I. Perevyazko, D. Cialla-May, M. Steinert, N. Janunts, D. Sivun, S. Hoeppener, M. D. Hager, T. Pertsch, U. S. Schubert, and C. Rockstuhl, "Synthesis, Separation, and Hypermethod Characterization of Gold Nanoparticle Dimers Connected by a Rigid Rod Linker," J Phys Chem C **119**, 17809-17817 (2015).

31. R. W. Taylor, T. C. Lee, O. A. Scherman, R. Esteban, J. Aizpurua, F. M. Huang, J. J. Baumberg, and S. Mahajan, "Precise Subnanometer Plasmonic Junctions for SERS within Gold Nanoparticle Assemblies Using Cucurbit[n]uril "Glue"," ACS Nano **5**, 3878-3887 (2011).

32. V. V. Thacker, L. O. Herrmann, D. O. Sigle, T. Zhang, T. Liedl, J. J. Baumberg, and U. F. Keyser, "DNA origami based assembly of gold nanoparticle dimers for surface-enhanced Raman scattering," Nat Commun **5**, 3448 (2014).

33. Z. Shen, and L. Su, "Plasmonic trapping and tuning of a gold nanoparticle dimer," Opt Express **24**, 4801-4811 (2016).

34. Z. Shen, L. Su, and Y. C. Shen, "Vertically-oriented nanoparticle dimer based on focused plasmonic trapping," Opt Express **24**, 16052-16065 (2016).

35. Z. Shen, L. Su, X. C. Yuan, and Y. C. Shen, "Trapping and rotating of a metallic particle trimer with optical vortex," Appl Phys Lett **109**, 241901 (2016).

36. G. Ruthemann, "*ELEKTRONENBREMSUNG AN RONTGENNIVEAUS," Ann. Phys.-Berlin **2**, 135-146 (1948).

37. G. Ruthemann, "*Diskrete Energieverluste Mittelschneller Elektronen Beim Durchgang Durch Dunne Folien," Ann Phys **2**, 113-134 (1948).

38. W. Lang, "*Geschwindigkeitsverluste Mittelschneller Elektronen Beim Durchgang Durch Dunne Metallfolien," Optik **3**, 233-246 (1948).

39. R. H. Ritchie, "Plasma Losses by Fast Electrons in Thin Films," Phys Rev **106**, 874-881 (1957).

40. C. J. Powell, and J. B. Swan, "Origin of the Characteristic Electron Energy Losses in Aluminum," Phys Rev **115**, 869-875 (1959).

41. C. J. Powell, and J. B. Swan, "Origin of the Characteristic Electron Energy Losses in Magnesium," Phys Rev **116**, 81-83 (1959).

42. D. Bohm, and D. Pines, "A Collective Description of Electron Interactions .3. Coulomb Interactions in a Degenerate Electron Gas," Phys Rev **92**, 609-625 (1953).

43. E. A. Stern, and R. A. Ferrell, "Surface Plasma Oscillations of a Degenerate Electron Gas," Phys Rev **120**, 130-136 (1960).

44. A. Otto, "Excitation of Nonradiative Surface Plasma Waves in Silver by Method of Frustrated Total Reflection," Z Phys **216**, 398-410 (1968).

45. Kretschm.E, and H. Raether, "Radiative Decay of Non Radiative Surface Plasmons Excited by Light," Z Naturforsch Pt A **A 23**, 2135-2136 (1968).

46. H. Raether, *Surface plasmons on smooth and rough surfaces and on gratings* (Springer, 1988).

47. W. Knoll, "Interfaces and thin films as seen by bound electromagnetic waves," Annu Rev Phys Chem **49**, 569-638 (1998).

48. A. V. Zayats, I. I. Smolyaninov, and A. A. Maradudin, "Nano-optics of surface plasmon polaritons," Phys Rep **408**, 131-314 (2005).

49. K. A. Willets, and R. P. Van Duyne, "Localized surface plasmon resonance spectroscopy and sensing," Annu Rev Phys Chem **58**, 267-297 (2007).

50. K. L. Kelly, E. Coronado, L. L. Zhao, and G. C. Schatz, "The optical properties of metal nanoparticles: The influence of size, shape, and dielectric environment," J Phys Chem B **107**, 668-677 (2003).

51. P. Coullet, L. Gil, and F. Rocca, "Optical Vortices," Opt Commun **73**, 403-408 (1989).

52. J. F. Nye, and M. V. Berry, "Dislocations in Wave Trains," P Roy Soc Lond a Mat **336**, 165-190 (1974).

53. L. W. Deng, H. H. He, Z. K. Feng, J. J. Jiang, X. C. Zhang, and W. H. Xiong, "Microwave electromagnetic characteristics of CoFeZrRE magnetic films," Rare Metal Mat Eng **35**, 986-989 (2006).

54. M. W. Beijersbergen, R. P. C. Coerwinkel, M. Kristensen, and J. P. Woerdman, "Helical-Wave-Front Laser-Beams Produced with a Spiral Phaseplate," Opt Commun **112**, 321-327 (1994).

55. B. R. Brown, and A. W. Lohmann, "Computer-Generated Binary Holograms," Ibm J Res Dev **13**, 160-168 (1969).

56. A. W. Lohmann, and D. P. Paris, "Binary Fraunhofer Holograms Generated by Computer," Appl Opt **6**, 1739-1748 (1967).

57. N. R. Heckenberg, R. Mcduff, C. P. Smith, H. Rubinszteindunlop, and M. J. Wegener, "Laser-Beams with Phase Singularities," Opt Quant Electron **24**, S951-S962 (1992).

58. N. R. Heckenberg, R. Mcduff, C. P. Smith, and A. G. White, "Generation of Optical-Phase Singularities by Computer-Generated Holograms," Opt Lett **17**, 221-223 (1992).

59. P. S. Tan, X. C. Yuan, J. Lin, Q. Wang, T. Mei, R. E. Burge, and G. G. Mu, "Surface plasmon polaritons generated by optical vortex beams," Appl Phys Lett **92**, 111108 (2008).

60. H. He, M. E. J. Friese, N. R. Heckenberg, and H. Rubinszteindunlop, "Direct Observation of Transfer of Angular-Momentum to Absorptive Particles from a Laser-Beam with a Phase Singularity," Phys Rev Lett **75**, 826-829 (1995).

61. H. Rubinsztein-Dunlop, T. A. Nieminen, M. E. J. Friese, and N. R. Heckenberg, "Optical trapping of absorbing particles," Adv Quantum Chem **30**, 469-492 (1998).

62. K. T. Gahagan, and G. A. Swartzlander, "Trapping of low-index microparticles in an optical vortex," Journal of the Optical Society of America B-Optical Physics **15**, 524-534 (1998).

63. D. G. Grier, "A revolution in optical manipulation," Nature **424**, 810-816 (2003).

64. H. He, N. R. Heckenberg, and H. Rubinszteindunlop, "Optical-Particle Trapping with Higher-Order Doughnut Beams Produced Using High-Efficiency Computer-Generated Holograms," J. Mod. Opt. **42**, 217-223 (1995).

65. K. Okamoto, *Fundamentals of optical waveguides* (Elsevier, 2006).

66. S. Ramachandran, P. Kristensen, and M. F. Yan, "Generation and propagation of radially polarized beams in optical fibers," Opt Lett **34**, 2525-2527 (2009).

67. V. G. Niziev, and A. V. Nesterov, "Influence of beam polarization on laser cutting efficiency," J Phys D Appl Phys **32**, 1455-1461 (1999).

68. S. Quabis, R. Dorn, M. Eberler, O. Glockl, and G. Leuchs, "Focusing light to a tighter spot," Opt Commun **179**, 1-7 (2000).

69. R. Dorn, S. Quabis, and G. Leuchs, "Sharper focus for a radially polarized light beam," Phys Rev Lett **91**, 233901 (2003).

70. J. K. Moh, "Radially polarized beams for surface plasmon microscopy," Thesis, Nanyang Technological University, 2009.

71. R. C. Jones, "A new calculus for the treatment of optical systems I. Description and discussion of the calculus," J Opt Soc Am **31**, 488-493 (1941).

72. S. A. Maier, *Plasmonics: Fundamentals and Applications* (Springer, 2007).

73. H. Y. Lin, C. H. Huang, C. H. Chang, Y. C. Lan, and H. C. Chui, "Direct near-field optical imaging of plasmonic resonances in metal nanoparticle pairs," Opt Express **18**, 165-172 (2010).

74. W. Li, P. H. Camargo, X. Lu, and Y. Xia, "Dimers of silver nanospheres: facile synthesis and their use as hot spots for surface-enhanced Raman scattering," Nano Lett **9**, 485-490 (2009).

75. J. H. Lee, J. M. Nam, K. S. Jeon, D. K. Lim, H. Kim, S. Kwon, H. Lee, and Y. D. Suh, "Tuning and Maximizing the Single-Molecule Surface-Enhanced Raman Scattering from DNA-Tethered Nanodumbbells," ACS Nano **6**, 9574-9584 (2012).

76. M. Lankers, J. Popp, E. Urlaub, H. Stahl, G. Rossling, and W. Kiefer, "Investigations of Multiple Component Systems by Means of Optical Trapping and Raman-Spectroscopy," J Mol Struct **348**, 265-268 (1995).

77. K. Ajito, and K. Torimitsu, "Laser trapping and Raman spectroscopy of single cellular organelles in the nanometer range," Lab Chip **2**, 11-14 (2002).

78. M. Gu, J. B. Haumonte, Y. Micheau, J. W. M. Chon, and X. S. Gan, "Laser trapping and manipulation under focused evanescent wave illumination," Appl Phys Lett **84**, 4236-4238 (2004).

79. C. M. Creely, G. Volpe, G. P. Singh, M. Soler, and D. V. Petrov, "Raman imaging of floating cells," Opt Express **13**, 6105-6110 (2005).

80. W. Tang, R. J. Newton, C. A. Xie, Y. Q. Li, and N. Whitley, "Non-destructive analysis of the nuclei of transgenic living cells using laser tweezers and near-infrared raman spectroscopic technique," Genomics Proteomics Bioinformatics **3**, 169-178 (2005).

81. P. R. T. Jess, V. Garces-Chavez, D. Smith, M. Mazilu, L. Paterson, A. Riches, C. S. Herrington, W. Sibbett, and K. Dholakia, "Dual beam fibre trap for Raman microspectroscopy of single cells," Opt Express **14**, 5779-5791 (2006).

82. S. Ahlawat, N. Kumar, R. Dasgupta, R. S. Verma, A. Uppal, and P. K. Gupta, "Raman spectroscopic investigations on optical trap induced deoxygenation of red blood cells," Appl Phys Lett **103**, 183704 (2013).

83. J. Kepler, *De cometis libelli tres* (Typis Andreµ Apergeri, sumptibus Sebastiani Mylii, 1619).

84. J. C. Maxwell, *A treatise on electricity and magnetism* (Clarendon Press, 1881).

85. P. Lebedev, "Experimental examination of light pressure," Nuovo Cimento **15**, 195 (1883).

86. E. F. Nichols, and G. F. Hull, "A preliminary communication on the pressure of heat and light radiation," Phys Rev **13**, 307-320 (1901).

87. A. Ashkin, "Acceleration and Trapping of Particles by Radiation Pressure," Phys Rev Lett **24**, 156 (1970).

88. A. Ashkin, J. M. Dziedzic, J. E. Bjorkholm, and S. Chu, "Observation of a Single-Beam Gradient Force Optical Trap for Dielectric Particles," Opt Lett **11**, 288-290 (1986).

89. K. F. Ren, G. Grehan, and G. Gouesbet, "Prediction of reverse radiation pressure by generalized Lorenz-Mie theory," Appl Opt **35**, 2702-2710 (1996).

90. P. C. Chaumet, and M. Nieto-Vesperinas, "Time-averaged total force on a dipolar sphere in an electromagnetic field," Opt Lett **25**, 1065-1067 (2000).

91. K. Svoboda, and S. M. Block, "Optical Trapping of Metallic Rayleigh Particles," Opt Lett **19**, 930-932 (1994).

92. P. M. Hansen, V. K. Bhatia, N. Harrit, and L. Oddershede, "Expanding the optical trapping range of gold nanoparticles," Nano Lett **5**, 1937-1942 (2005).

93. L. Bosanac, T. Aabo, P. M. Bendix, and L. B. Oddershede, "Efficient optical trapping and visualization of silver nanoparticles," Nano Lett **8**, 1486-1491 (2008).

94. Q. W. Zhan, "Trapping metallic Rayleigh particles with radial polarization," Opt Express **12**, 3377-3382 (2004).

95. K. Sasaki, M. Koshioka, H. Misawa, N. Kitamura, and H. Masuhara, "Optical Trapping of a Metal-Particle and a Water Droplet by a Scanning Laser-Beam," Appl Phys Lett **60**, 807-809 (1992).

96. S. Sato, Y. Harada, and Y. Waseda, "Optical Trapping of Microscopic Metal Particles," Opt Lett **19**, 1807-1809 (1994).

97. H. Furukawa, and I. Yamaguchi, "Optical trapping of metallic particles by a fixed Gaussian beam," Opt Lett **23**, 216-218 (1998).

98. M. Gu, D. Morrish, and P. C. Ke, "Enhancement of transverse trapping efficiency for a metallic particle using an obstructed laser beam," Appl Phys Lett **77**, 34-36 (2000).

99. A. T. O'Neil, and M. J. Padgett, "Three-dimensional optical confinement of micron-sized metal particles and the decoupling of the spin and orbital angular momentum within an optical spanner," Opt Commun **185**, 139-143 (2000).

100. Y. Q. Zhao, J. S. Edgar, G. D. M. Jeffries, D. McGloin, and D. T. Chiu, "Spin-to-orbital angular momentum conversion in a strongly focused optical beam," Phys Rev Lett **99**, 073901 (2007).

101. M. Dienerowitz, M. Mazilu, P. J. Reece, T. F. Krauss, and K. Dholakia, "Optical vortex trap for resonant confinement of metal nanoparticles," Opt Express **16**, 4991-4999 (2008).

102. Y. Q. Zhang, W. Shi, Z. Shen, Z. S. Man, C. J. Min, J. F. Shen, S. W. Zhu, H. P. Urbach, and X. C. Yuan, "A Plasmonic Spanner for Metal Particle Manipulation," Sci Rep **5**, 15446 (2015).

103. Y. G. Song, B. M. Han, and S. Chang, "Force of surface plasmon-coupled evanescent fields on Mie particles," Opt Commun **198**, 7-19 (2001).

104. G. Volpe, R. Quidant, G. Badenes, and D. Petrov, "Surface plasmon radiation forces," Phys Rev Lett **96**, 238101 (2006).

105. K. Wang, E. Schonbrun, and K. B. Crozier, "Propulsion of gold nanoparticles with surface plasmon polaritons: evidence of enhanced optical force from near-field coupling between gold particle and gold film," Nano Lett **9**, 2623-2629 (2009).

106. K. C. Neuman, and S. M. Block, "Optical trapping," Rev Sci Instrum **75**, 2787-2809 (2004).

107. M. Righini, A. S. Zelenina, C. Girard, and R. Quidant, "Parallel and selective trapping in a patterned plasmonic landscape," Nat Phys **3**, 477-480 (2007).

108. R. Quidant, and C. Girard, "Surface-plasmon-based optical manipulation," Laser Photonics Rev **2**, 47-57 (2008).

109. M. L. Juan, M. Righini, and R. Quidant, "Plasmon nano-optical tweezers," Nat Photonics **5**, 349-356 (2011).

110. B. J. Roxworthy, K. D. Ko, A. Kumar, K. H. Fung, E. K. C. Chow, G. L. Liu, N. X. Fang, and K. C. Toussaint, "Application of Plasmonic Bowtie Nanoantenna Arrays for Optical Trapping, Stacking, and Sorting," Nano Lett **12**, 796-801 (2012).

111. K. J. Moh, X. C. Yuan, J. Bu, S. W. Zhu, and B. Z. Gao, "Surface plasmon resonance imaging of cell-substrate contacts with radially polarized beams," Opt Express **16**, 20734-20741 (2008).

112. K. J. Moh, X. C. Yuan, J. Bu, S. W. Zhu, and B. Z. Gao, "Radial polarization induced surface plasmon virtual probe for two-photon fluorescence microscopy," Opt Lett **34**, 971-973 (2009).

113. Q. W. Zhan, "Evanescent Bessel beam generation via surface plasmon resonance excitation by a radially polarized beam," Opt Lett **31**, 1726-1728 (2006).

114. A. Farhang, N. Bigler, and O. J. F. Martin, "Coupling of multiple LSP and SPP resonances: interactions between an elongated nanoparticle and a thin metallic film," Opt Lett **38**, 4758-4761 (2013).

115. G. Leveque, and O. J. F. Martin, "Optical interactions in a plasmonic particle coupled to a metallic film," Opt Express **14**, 9971-9981 (2006).

116. F. Le, N. Z. Lwin, N. J. Halas, and P. Nordlander, "Plasmonic interactions between a metallic nanoshell and a thin metallic film," Phys Rev B **76**, 165410 (2007).

117. P. Nordlander, and E. Prodan, "Plasmon Hybridization in Nanoparticles near Metallic Surfaces," Nano Lett **4**, 2209-2213 (2004).

118. N. Papanikolaou, "Optical properties of metallic nanoparticle arrays on a thin metallic film," Phys Rev B **75**, 235426 (2007).

119. Y. P. Wu, and P. Nordlander, "Finite-Difference Time-Domain Modeling of the Optical Properties of Nanoparticles near Dielectric Substrates," J Phys Chem C **114**, 7302-7307 (2010).

120. H. Wang, T. Liu, Y. Z. Huang, Y. R. Fang, R. C. Liu, S. X. Wang, W. J. Wen, and M. T. Sun, "Plasmon-driven surface catalysis in hybridized plasmonic gap modes," Sci Rep **4**, 07087 (2014).

121. D. J. Griffiths, *Introduction to electrodynamics* (Prentice Hall, 1999).

122. P. M. Bendix, S. Nader, S. Reihani, and L. B. Oddershede, "Direct Measurements of Heating by Electromagnetically Trapped Gold Nanoparticles on Supported Lipid Bilayers," ACS Nano **4**, 2256-2262 (2010).

123. S. Duhr, and D. Braun, "Why molecules move along a temperature gradient," P Natl Acad Sci USA **103**, 19678-19682 (2006).

124. V. Garces-Chavez, R. Quidant, P. J. Reece, G. Badenes, L. Torner, and K. Dholakia, "Extended organization of colloidal microparticles by surface plasmon polariton excitation," Phys Rev B **73**, 085417 (2006).

125. M. Ploschner, M. Mazilu, T. F. Krauss, and K. Dholakia, "Optical forces near a nanoantenna," J Nanophotonics **4**, 041570 (2010).

126. Y. Seol, A. E. Carpenter, and T. T. Perkins, "Gold nanoparticles: enhanced optical trapping and sensitivity coupled with significant heating," Opt Lett **31**, 2429-2431 (2006).

127. W. B. Chen, and Q. W. Zhan, "Realization of an evanescent Bessel beam via surface plasmon interference excited by a radially polarized beam," Opt Lett **34**, 722-724 (2009).

128. T. Atay, J. H. Song, and A. V. Nurmikko, "Strongly interacting plasmon nanoparticle pairs: From dipole-dipole interaction to conductively coupled regime," Nano Lett **4**, 1627-1631 (2004).

129. J. I. Chen, Y. Chen, and D. S. Ginger, "Plasmonic nanoparticle dimers for optical sensing of DNA in complex media," J Am Chem Soc **132**, 9600-9601 (2010).
130. P. Nordlander, C. Oubre, E. Prodan, K. Li, and M. I. Stockman, "Plasmon Hybridization in Nanoparticle Dimers," Nano Lett **4**, 899-903 (2004).
131. I. Romero, J. Aizpurua, G. W. Bryant, and F. J. G. de Abajo, "Plasmons in nearly touching metallic nanoparticles: singular response in the limit of touching dimers," Opt Express **14**, 9988-9999 (2006).
132. C. E. Talley, J. B. Jackson, C. Oubre, N. K. Grady, C. W. Hollars, S. M. Lane, T. R. Huser, P. Nordlander, and N. J. Halas, "Surface-enhanced Raman scattering from individual Au nanoparticles and nanoparticle dimer substrates," Nano Lett **5**, 1569-1574 (2005).
133. A. Kinkhabwala, Z. F. Yu, S. H. Fan, Y. Avlasevich, K. Mullen, and W. E. Moerner, "Large single-molecule fluorescence enhancements produced by a bowtie nanoantenna," Nat Photonics **3**, 654-657 (2009).
134. B. Pettinger, B. Ren, G. Picardi, R. Schuster, and G. Ertl, "Nanoscale probing of adsorbed species by tip-enhanced Raman spectroscopy," Phys Rev Lett **92**, 096101 (2004).
135. D. C. Marinica, A. K. Kazansky, P. Nordlander, J. Aizpurua, and A. G. Borisov, "Quantum Plasmonics: Nonlinear Effects in the Field Enhancement of a Plasmonic Nanoparticle Dimer," Nano Lett **12**, 1333-1339 (2012).
136. J. M. McMahon, A. I. Henry, K. L. Wustholz, M. J. Natan, R. G. Freeman, R. P. Van Duyne, and G. C. Schatz, "Gold nanoparticle dimer plasmonics: finite element method calculations of the electromagnetic enhancement to surface-enhanced Raman spectroscopy," Anal Bioanal Chem **394**, 1819-1825 (2009).
137. L. Huang, H. L. Guo, J. F. Li, L. Ling, B. H. Feng, and Z. Y. Li, "Optical trapping of gold nanoparticles by cylindrical vector beam," Opt Lett **37**, 1694-1696 (2012).
138. P. T. Lin, H. Y. Chu, T. W. Lu, and P. T. Lee, "Trapping particles using waveguide-coupled gold bowtie plasmonic tweezers," Lab Chip **14**, 4647-4652 (2014).
139. S. A. Maier, M. L. Brongersma, P. G. Kik, S. Meltzer, A. A. G. Requicha, and H. A. Atwater, "Plasmonics - A route to nanoscale optical devices," Adv Mater **13**, 1501-1505 (2001).

140. Y. Q. Zhang, J. Wang, J. F. Shen, Z. S. Man, W. Shi, C. J. Min, G. H. Yuan, S. W. Zhu, H. P. Urbach, and X. C. Yuan, "Plasmonic Hybridization Induced Trapping and Manipulation of a Single Au Nanowire on a Metallic Surface," Nano Lett **14**, 6430-6436 (2014).

141. A. Bouhelier, F. Ignatovich, A. Bruyant, C. Huang, G. C. D. Francs, J. C. Weeber, A. Dereux, G. P. Wiederrecht, and L. Novotny, "Surface plasmon interference excited by tightly focused laser beams," Opt Lett **32**, 2535-2537 (2007).

142. F. D. Stefani, K. Vasilev, N. Bocchio, N. Stoyanova, and M. Kreiter, "Surface-plasmon-mediated single-molecule fluorescence through a thin metallic film," Phys Rev Lett **94**, 023005 (2005).

143. L. Novotny, and B. Hecht, *Principles of nano-optics* (Cambridge University Press, 2012).

144. B. Richards, and E. Wolf, "Electromagnetic Diffraction in Optical Systems .2. Structure of the Image Field in an Aplanatic System," Proc R Soc Lon Ser-A **253**, 358-379 (1959).

145. P. B. Johnson, and R. W. Christy, "Optical Constants of Noble Metals," Phys Rev B **6**, 4370-4379 (1972).

146. E. Wolf, "Electromagnetic Diffraction in Optical Systems .1. An Integral Representation of the Image Field," Proc R Soc Lon Ser-A **253**, 349-357 (1959).

147. Z. Shen, Z. J. Hu, G. H. Yuan, C. J. Min, H. Fang, and X. C. Yuan, "Visualizing orbital angular momentum of plasmonic vortices," Opt Lett **37**, 4627-4629 (2012).

148. A. D. Rakic, A. B. Djurisic, J. M. Elazar, and M. L. Majewski, "Optical properties of metallic films for vertical-cavity optoelectronic devices," Appl Opt **37**, 5271-5283 (1998).

149. E. C. Le Ru, and P. G. Etchegoin, "Rigorous justification of the [E](4) enhancement factor in Surface Enhanced Raman Spectroscopy," Chem Phys Lett **423**, 63-66 (2006).

150. K. D. Alexander, K. Skinner, S. P. Zhang, H. Wei, and R. Lopez, "Tunable SERS in Gold Nanorod Dimers through Strain Control on an Elastomeric Substrate," Nano Lett **10**, 4488-4493 (2010).

151. J. Q. Jiao, X. Wang, F. Wackenhut, A. Horneber, L. P. Chen, A. V. Failla, A. J. Meixner, and D. Zhang, "Polarization-Dependent SERS at Differently Oriented Single Gold Nanorods," Chemphyschem **13**, 952-958 (2012).

152. N. A. Hatab, C. H. Hsueh, A. L. Gaddis, S. T. Retterer, J. H. Li, G. Eres, Z. Zhang, and B. Gu, "Free-standing optical gold bowtie nanoantenna with variable gap size for enhanced Raman spectroscopy," Nano Lett **10**, 4952-4955 (2010).

153. K. Fujita, S. Ishitobi, K. Hamada, N. I. Smith, A. Taguchi, Y. Inouye, and S. Kawata, "Time-resolved observation of surface-enhanced Raman scattering from gold nanoparticles during transport through a living cell," J Biomed Opt **14**, 024038 (2009).

154. E. Bailo, and V. Deckert, "Tip-enhanced Raman spectroscopy of single RNA strands: towards a novel direct-sequencing method," Angewandte Chemie **47**, 1658-1661 (2008).

155. L. P. Du, D. Y. Tang, G. H. Yuan, S. B. Wei, and X. C. Yuan, "Emission pattern of surface-enhanced Raman scattering from single nanoparticle-film junction," Appl Phys Lett **102**, 081117 (2013).

156. J. F. Shen, J. Wang, C. J. Zhang, C. J. Min, H. Fang, L. P. Du, S. W. Zhu, and X. C. Yuan, "Dynamic plasmonic tweezers enabled single-particle-film-system gap-mode Surface-enhanced Raman scattering," Appl Phys Lett **103**, 191119 (2013).

157. E. G. Bortchagovsky, S. Klein, and U. C. Fischer, "Surface plasmon mediated tip enhanced Raman scattering," Appl Phys Lett **94**, 063118 (2009).

158. K. Uetsuki, P. Verma, P. Nordlander, and S. Kawata, "Tunable plasmon resonances in a metallic nanotip-film system," Nanoscale **4**, 5931-5935 (2012).

159. K. Kneipp, Y. Wang, H. Kneipp, L. T. Perelman, I. Itzkan, R. Dasari, and M. S. Feld, "Single molecule detection using surface-enhanced Raman scattering (SERS)," Phys Rev Lett **78**, 1667-1670 (1997).

160. Z. D. Schultz, J. M. Marr, and H. Wang, "Tip enhanced Raman scattering: plasmonic enhancements for nanoscale chemical analysis," Nanophotonics **3**, 91-104 (2014).

161. S. Albaladejo, R. Gómez-Medina, L. S. Froufe-Pérez, H. Marinchio, R. Carminati, J. F. Torrado, G. Armelles, A. García-Martín, and J. J. Sáenz, "Radiative corrections to the polarizability tensor of an electrically small anisotropic dielectric particle," Opt Express **18**, 3556-3567 (2010).

162. C. F. Bohren, and D. R. Huffman, *Absorption and scattering of light by small particles* (Wiley, 1983).

163. V. V. Gozhenko, L. G. Grechko, and K. W. Whites, "Electrodynamics of spatial clusters of spheres: Substrate effects," Phys Rev B **68**, 125422 (2003).

164. A. Pinchuk, and G. Schatz, "Anisotropic polarizability tensor of a dimer of nanospheres in the vicinity of a plane substrate," Nanotechnology **16**, 2209-2217 (2005).

165. A. A. E. Saleh, and J. A. Dionne, "Toward Efficient Optical Trapping of Sub-10-nm Particles with Coaxial Plasmonic Apertures," Nano Lett **12**, 5581-5586 (2012).

166. A. H. J. Yang, T. Lerdsuchatawanich, and D. Erickson, "Forces and Transport Velocities for a Particle in a Slot Waveguide," Nano Lett **9**, 1182-1188 (2009).

167. Y. S. Touloukian, *Thermal conductivity: metallic elements and alloys* (IFI/Plenum, 1970).

168. E. L. Florin, A. Pralle, E. H. K. Stelzer, and J. K. H. Horber, "Photonic force microscope calibration by thermal noise analysis," Appl Phys a-Mater **66**, S75-S78 (1998).

169. L. I. McCann, M. Dykman, and B. Golding, "Thermally activated transitions in a bistable three-dimensional optical trap," Nature **402**, 785-787 (1999).

170. R. Dasgupta, S. Ahlawat, R. S. Verma, and P. K. Gupta, "Optical orientation and rotation of trapped red blood cells with Laguerre-Gaussian mode," Opt Express **19**, 7680-7688 (2011).

171. O. M. Marago, P. H. Jones, P. G. Gucciardi, G. Volpe, and A. C. Ferrari, "Optical trapping and manipulation of nanostructures," Nat Nanotechnol **8**, 807-819 (2013).

172. N. B. Simpson, L. Allen, and M. J. Padgett, "Optical tweezers and optical spanners with Laguerre-Gaussian modes," J Mod Optic **43**, 2485-2491 (1996).

173. N. B. Simpson, K. Dholakia, L. Allen, and M. J. Padgett, "Mechanical equivalence of spin and orbital angular momentum of light: An optical spanner," Opt Lett **22**, 52-54 (1997).

174. M. Liu, T. Zentgraf, Y. M. Liu, G. Bartal, and X. Zhang, "Light-driven nanoscale plasmonic motors," Nat Nanotechnol **5**, 570-573 (2010).

175. T. Asavei, V. L. Y. Loke, M. Barbieri, T. A. Nieminen, N. R. Heckenberg, and H. Rubinsztein-Dunlop, "Optical angular momentum transfer to microrotors fabricated by two-photon photopolymerization," New J Phys **11**, 093021 (2009).

176. H. Ukita, and H. Kawashima, "Optical rotor capable of controlling clockwise and counterclockwise rotation in optical tweezers by displacing the trapping position," Appl Opt **49**, 1991-1996 (2010).
177. S. Maruo, A. Takaura, and Y. Saito, "Optically driven micropump with a twin spiral microrotor," Opt Express **17**, 18525-18532 (2009).
178. X. F. Lin, G. Q. Hu, Q. D. Chen, L. G. Niu, Q. S. Li, A. Ostendorf, and H. B. Sun, "A light-driven turbine-like micro-rotor and study on its light-to-mechanical power conversion efficiency," Appl Phys Lett **101**, 113901 (2012).
179. Y. W. Zong, J. Liu, R. Liu, H. L. Guo, M. C. Yang, Z. Y. Li, and K. Chen, "An Optically Driven Bistable Janus Rotor with Patterned Metal Coatings," ACS Nano **9**, 10844-10851 (2015).
180. R. A. Beth, "Mechanical detection and measurement of the angular momentum of light," Phys Rev **50**, 115-125 (1936).
181. L. Allen, M. W. Beijersbergen, R. J. C. Spreeuw, and J. P. Woerdman, "Orbital Angular-Momentum of Light and the Transformation of Laguerre-Gaussian Laser Modes," Phys Rev A **45**, 8185-8189 (1992).
182. A. T. O'Neil, I. MacVicar, L. Allen, and M. J. Padgett, "Intrinsic and extrinsic nature of the orbital angular momentum of a light beam," Phys Rev Lett **88**, 053601 (2002).
183. M. C. Zhong, J. H. Zhou, Y. X. Ren, Y. M. Li, and Z. Q. Wang, "Rotation of birefringent particles in optical tweezers with spherical aberration," Appl Opt **48**, 4397-4402 (2009).
184. F. W. Sheu, T. K. Lan, Y. C. Lin, S. U. Chen, and C. Ay, "Stable trapping and manually controlled rotation of an asymmetric or birefringent microparticle using dual-mode split-beam optical tweezers," Opt Express **18**, 14724-14729 (2010).
185. K. D. Wulff, D. G. Cole, and R. L. Clark, "Controlled rotation of birefringent particles in an optical trap," Appl Opt **47**, 6428-6433 (2008).
186. J. L. Zhang, T. G. Kim, S. C. Jeoung, F. F. Yao, H. Lee, and X. D. Sun, "Controlled trapping and rotation of carbon nanotube bundle with optical tweezers," Opt Commun **267**, 260-263 (2006).
187. C. I. Ha, H. S. Wi, and H. K. Pak, "Rotation of irregularly shaped liposome using optical tweezers," J Korean Phys Soc **48**, S222-S225 (2006).

188. E. Higurashi, O. Ohguchi, T. Tamamura, H. Ukita, and R. Sawada, "Optically induced rotation of dissymmetrically shaped fluorinated polyimide micro-objects in optical traps," J Appl Phys **82**, 2773-2779 (1997).

189. G. D. M. Jeffries, J. S. Edgar, Y. Q. Zhao, J. P. Shelby, C. Fong, and D. T. Chiu, "Using polarization-shaped optical vortex traps for single-cell nanosurgery," Nano Lett **7**, 415-420 (2007).

190. M. J. Padgett, and L. Allen, "The Poynting Vector in Laguerre-Gaussian Laser Modes," Opt Commun **121**, 36-40 (1995).

191. M. Dienerowitz, M. Mazilu, P. J. Reece, T. F. Krauss, and K. Dholakia, "Optical vortex trap for resonant confinement of metal nanoparticles," Optics express **16**, 4991-4999 (2008).

192. J. Happel, and H. Brenner, *Low Reynolds number hydrodynamics : with special applications to particulate media* (Noordhoff International Publishing, 1973).

193. K. Svoboda, and S. M. Block, "Biological Applications of Optical Forces," Annu Rev Bioph Biom **23**, 247-285 (1994).

194. M. E. J. Friese, J. Enger, H. RubinszteinDunlop, and N. R. Heckenberg, "Optical angular-momentum transfer to trapped absorbing particles," Phys Rev A **54**, 1593-1596 (1996).

195. L. Novotny, R. X. Bian, and X. S. Xie, "Theory of nanometric optical tweezers," Phys Rev Lett **79**, 645-648 (1997).

196. L. C. Zhang, X. J. Dou, C. J. Min, Y. Q. Zhang, L. P. Du, Z. W. Xie, J. F. Shen, Y. J. Zeng, and X. C. Yuan, "In-plane trapping and manipulation of ZnO nanowires by a hybrid plasmonic field," Nanoscale **8**, 9756-9763 (2016).